The solar internetwork

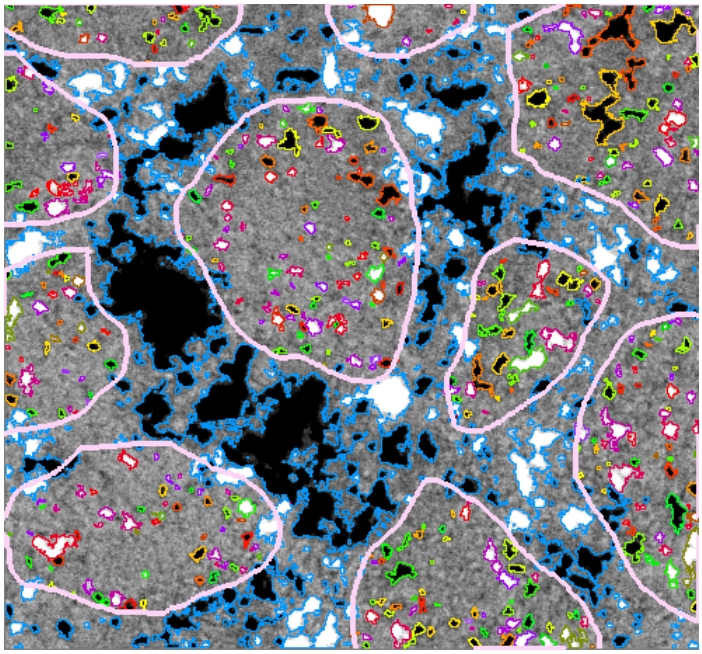

Milan Gošić

INSTITUTO de ASTROFÍSICA de ANDALUCÍA

Consejo Superior de Investigaciones Científicas

Editor: Universidad de Granada. Tesis Doctorales
Autor: Milan Gosic
ISBN: 978-84-9125-406-5
URI: http://hdl.handle.net/10481/41677

FÍSICA Y CIENCIAS DEL ESPACIO

Universidad de Granada

The solar internetwork

Memoria que presenta
D. Milan Gošić
para optar al grado de
Doctor en Astrofísica.

Dr. D. Luis Ramón Bellot Rubio

INSTITUTO de ASTROFÍSICA de ANDALUCÍA

Consejo Superior de Investigaciones Científicas

Director de la tesis: Dr. D. Luis Ramón Bellot Rubio

Declaración

El doctorando **Milan Gošić** y el director de la tesis **Dr. Luis Ramón Bellot Rubio**, garantizamos, al firmar esta tesis doctoral, que el trabajo ha sido realizado por el doctorando bajo la dirección de los directores de la tesis y hasta donde nuestro conocimiento alcanza, en la realización del trabajo, se han respetado los derechos de otros autores a ser citados, cuando se han utilizado sus resultados o publicaciones.

Gošić Milan

Milan Gošić
El doctorando

Dr. Luis Ramón Bellot Rubio
El director

Granada, 2 de noviembre de 2015

Resumen

En esta tesis se estudia la evolución del campo magnético de la intrared en las escalas pequeñas y su contribución al magnetismo del Sol en calma.

Los elementos de la intrered son estructuras magnéticas muy dinámicas, de cortas vidas que pueblan el interior de las celdas supergranulares. Debido a su abundancia, se cree que estos campos pequeños son ingredientes esenciales para el magnetismo solar. Sin embargo, estos elementos son débiles y producen minúsculos señales de polarización, que es la razón por la cual sus propiedades son bastante desconocidas. Además de esto, los campos magnéticos de intrared están acopladas con la dinámica de las celdas supergranulares. Por lo tanto, para entender cómo evolucionan, es necesario seguirlos continuamente durante muchas horas. Hasta la época de Hinode, era imposible obtener observaciones que cumplen todos los requisitos para estudiar la evolución de los campos de la intrared.

Utilizado el Hinode Narrowband Filter Imager (NFI) nosotros obtuvimos observaciones de larga duración, con la resolución espacial y temporal sin precedentes y con la sensibilidad más alta jamás alcanzada. Estas observaciones por la primera vez nos permiten examinar la evolución de los parches individuales del flujo magnético en el Sol en calma en escalas temporales desde minutos hasta días.

Para estudiar elementos magnétos de la intrared en el Sol en calma utilizamos observaciones obtenidas con el Hinode/NFI en el marco de "Hinode Operation Plan 151". Las medidas se tomarón en la línea de resonancia Na I D1 en 589.6 nm. Nuestras secuencias de los magnetogramas tienen una alta sensibilidad de 4 Mx cm^{-2}, una resolución espacial de 0.16 segundos de arco por un pixel y una cadencia de $\sim$60 segundos.

Para seguir los parches individuales de flujo desde que nacen hasta

que mueren y analizar las interacciones entre ellos, hemos desarrollado un nuevo código para resolver algunos de los problemas de códigos automáticos de seguimiento que provocan interacciones mal identificadas y/o etiquetados incorrectos de los elementos magnéticos. Utilizando este código podemos determinar la historia de los parches individuales de una manera fiable. Estas correcciones nos permiten evaluar de una manera directa la importancia de la intrared para mantenimiento del flujo magnético del Sol en calma.

Nosotros clasificamos los parches de flujo detectados como parches de la intrared o red y analizamos cómo evolucionan con el tiempo y contribuyen al flujo del Sol. Nosotros encontramos que el flujo de la intrared aporta unos 15% del flujo absoluto total del Sol en calma. El resto es proporcionado por el NE. Las variaciones pequeñas temporales del flujo de la intrared y la red muestran que en escalas grandes están en un estado estable, pero también muestran que el flujo magnético dentro de las celdas superganulares puede aumentar casí un orden de magnitud cuando elementos magnéticos aparezcan en grupos por la superficie del Sol.

También analizamos por la primera vez cómo interaccionan los elementos de la intrared con los elementos de la red y contribuyen el flujo a ellos. Gracias a este estudio concluimos que las regiones de la intrared son fuentes del flujo más importantes de la red. En otras palabras, los parches de la intrared son capaces de mantener el flujo de la red. Sus contribuciones son mucho más grandes que de las zonas efímeras.

Nosotros describimos por la primera vez de una manera consistente cómo los supergranulos individuales ganan y pierden flujo magnético. Analizamos las fuentes y sumideros de flujo de la intrared y calculamos las tasas de aparición y desaparición del flujo total. Demostramos cómo estas tasas cambian con el tiempo y distancia desde los centros de las celdas. También discutimos las consecuencias de estos resultados para mecanismos responsables de la formación de elementos magnéticos de la intrared.

Summary

In this thesis we study the evolution of small-scale internetwork fields and their contribution to the quiet Sun magnetism.

Internernetwork elements are highly dynamic, short-lived magnetic structures that populate the interior of supergranular cells. Because of their abundance it is believed that these small-scale fields are essential ingredients of the solar magnetism. However, they are weak and produce tiny polarization signals, which is the reason why their properties are poorly known. In addition to this, internetwork fields are coupled to the dynamics of supergranular cells. Therefore, to understand their evolution it is necessary to follow them continuously for many hours. Until the Hinode era, it was impossible to obtain observations that fulfill all the requirements to study the evolution of internetwork fields.

Using the Hinode Narrowband Filter Imager (NFI) we obtained long duration observations at unprecedented spatial and temporal resolution with the highest sensitivity ever achieved. For the first time these observations allow us to examine the evolution of individual flux patches in the quiet Sun on temporal scales from minutes to days.

To study quiet Sun internetwork magnetic elements we used observations obtained with the Hinode/NFI in the framework of the Hinode Operation Plan 151. The measurements were carried out in the Na I D1 resonance line at 589.6 nm. Our magnetogram sequences have a high sensitivity of 4 Mx cm^{-2}, a spatial resolution of 0.16 arcsec/pixel and a cadence of $\sim$60 s.

To follow individual flux patches from birth to death and analyze the interactions between them, we developed a new code to solve some of the problems of automatic tracking codes that lead to misidentifications

and/or incorrect labeling of the magnetic elements. By use of this code we can determine the history of flux patches in a reliable manner. These corrections permit us to evaluate in a direct way the importance of the internetwork for the maintenance of the quiet Sun magnetic flux.

We classified the detected flux features as internetwork or network patches and analyzed how they evolve with time and contribute to the quiet Sun flux budget. We found that the internetwork flux accounts for about 15% of the total unsigned quiet Sun flux. The rest is provided by the network. The small temporal variations of the internetwork and network fluxes reveal their steady-state nature on large scales, but they also show that the flux inside of individual supergranular cells may increase by almost an order of magnitude when clusters of magnetic elements appear on the solar surface.

We analyzed for the first time how internetwork features interact with network elements and contribute their flux to the network. From this study we concluded that internetwork regions are the main source of flux for the network. In other words, internetwork flux features are capable of maintaining the network. Their contribution is much larger than that of ephemeral regions.

We describe in a consistent way for the first time how individual supergranular cells gain and lose magnetic flux. We analyze the sources and sinks of internetwork flux and calculate the total flux appearance and disappearance rates. We demonstrate that these rates change with time and distance from the cell centers. The results are discussed in terms of the mechanisms responsible for the formation of internetwork magnetic elements.

Contents

1

Introduction

The Sun as a star was perceived for a long time to be magnetic only in regions occupied by sunspots, traditionally known as *active* regions. Everywhere else, the solar surface seemed to be devoid of magnetic activity, and therefore was properly named the *quiet Sun* (QS). Such impression about solar magnetism remained intact until 1970s, when the magnetic fields were detected for the first time inside of the quiet areas. Since then, we have been observing small and weak, highly transient magnetic fields all over the solar disk. Thanks to development of observational technologies, the quiet Sun magnetic fields received a lot of attention in recent years and has been studied throughly. However, their origin, properties, and evolution are still fairly unknown. To understand the dynamical nature of the quiet Sun it is essential not only to grasp the observational phenomena but also to estimate their relative importance. With this thesis we are are giving our contribution to understanding of the QS magnetism.

We start this chapter briefly summarizing the main characteristics of the Sun as a star (Section 1.1). Then we describe the distinctive convective and magnetic field signatures visible on the solar surface. This includes description of granular motions (Section 1.2) and the solar magnetic fields, focusing on the QS (Section 1.3). Naturally, special attention is paid to progress made with the quiet Sun internetwork fields (Section 1.4). In Section 1.5 we list the open questions in the field of the QS magnetism. Finally, we summarize the aims of this thesis (Section 1.6) and give the outline in Section 1.7.

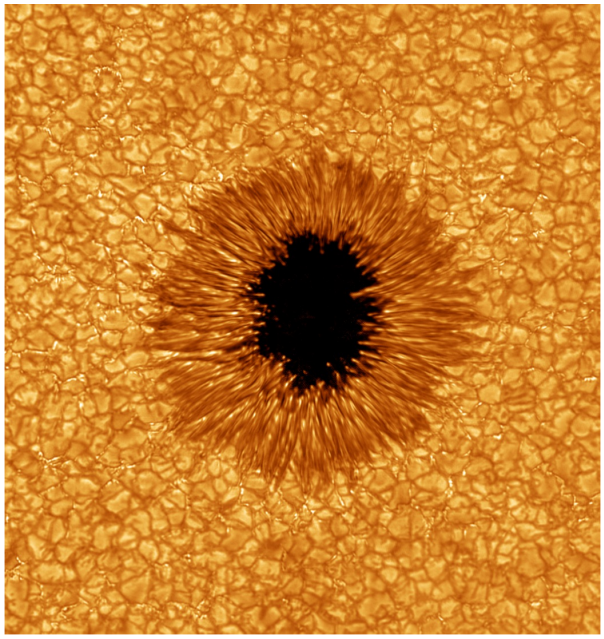

FIGURE 1.1:— Granulation around a sunspot in the photosphere. Granulation exhibit a typical boiling pattern. Sunspots consist of a dark area called *umbra*, and a less dark *penumbra* where convection is inhibited. The image of active region NOAA 1084 was taken with the New Solar Telescope at Big Bear Solar Observatory on July 2, 2010.

1.1 Characteristics of the Sun

The Sun is the closest star to Earth. It is composed of hydrogen (73%) and helium (25%), and has a mass of $M_\odot = (1.9889 \pm 0.0003) \times 10^{30}$ kg. The maximum of its energy radiates in the yellow-green part of the spectrum. The radius of the visible disk is $R_\odot = (6.960 \pm 0.001) \times 10^8$ m and the luminosity is $L_\odot = (3.844 \pm 0.010) \times 10^{26}$ W, which gives an effective temperature $T_{eff} = 5778 \pm 3$ K. Due to the Earth's elliptical orbit, the distance between the Earth and the Sun varies during the year around a mean value of 1.496×10^{11} m.

Thanks to its proximity, in terms of astronomical distances, the Sun is the only star whose surface can be sufficiently well resolved. This gives us the opportunity to study its atmosphere in detail. Geometrically, the atmosphere is defined as the interface region between star's interior and interstellar space.

The *photosphere* is the deepest and the densest layer of the solar atmo-

sphere. Almost all visible light originates from there, forming the majority part of the spectrum - continuum and absorption lines. The thickness of the Sun's photosphere is just a few hundreds of kilometers and its effective temperature is around 5800 K. The density is approximately 2×10^{-4} kg m^{-3}.

The most distinct structures of the photosphere are granulation and sunspots as shown in Figure 1.1. The image was recorded by the New Solar Telescope at Big Bear Solar Observatory on July 2, 2010 with an angular resolution of 0.1 arcsec[1]. The sunspot is visible as a dark area called *umbra*, enclosed by less darker *penumbra*. It is caused by intense magnetic fields, which inhibits convection, forming areas of reduced surface temperature. Away from the sunspot, we can see the QS where a granular pattern can easily be recognized, revealing bubbles of hot gas going up and colder gas going down. The granulation and magnetic phenomena on the solar surface are described below in Sections 1.2 and 1.3, respectively.

1.2 Solar convection

One of the mechanisms of heat transport is convection. Convection takes place when heated gas moves from hot regions to colder regions, taking the heat with it. This mechanism plays an important role in energy transport of stars with low effective temperature. As the effective temperature of the star decreases, the thickness of the convective zone increases, occupying larger and larger volumes of the star. In the Sun, this region is located under the photosphere and has a thickness of 30% of the solar radius (Berthomieu et al. 1980).

Because of the temperature difference between higher and lower layers of the convective zone, which is permeated by the gravitational field, the fluid is forced to move. Hot parcels rise up toward the solar surface and cold parcels sink down toward the bottom of convective zone.

A more detailed account of convection will be presented in the following two subsections.

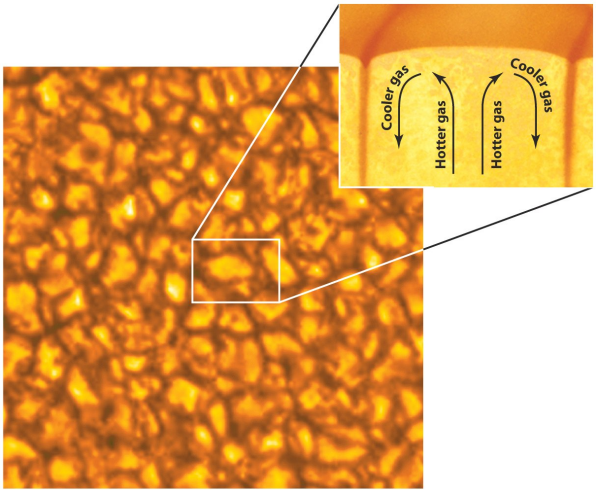

FIGURE 1.2:— Solar granulation as seen through a telescope and artist's impression of convective motions. The gas rises up toward the surface in the center of the granules, and expands horizontally. Cool gas sinks around the edges forming intergranular lanes. Image courtesy Pat Hall.

1.2.1 Granulation

To explain the granular motions in more detail, we will start with a fluid parcel inside of convective zone. We will assume that in a layer with a given temperature, there is no energy exchange between fluid element and surrounding environment. If for some reason the temperature of a gas parcel is increased, it will expand in order to maintain pressure equilibrium with its surroundings. Due to the ensuing decrease of gas density inside of the parcel, it rises up driven by buoyancy. When the gas densities inside and outside of the displaced element are equal again, the buoyancy force disappears and the parcel stops to rise.

When a fluid parcel reaches the upper layers, it expands rapidly due to the exponential decrease of the density with height in the atmosphere. In addition, while at the surface, the fluid radiates photons that carry away some fraction of thermal energy from the gas and as a result it cools down. Due to the lower temperature, hydrogen ions capture electrons and become neutral atoms. During this process, atoms radiate again and gas cools down even more. While cooling by radiation and expanding horizon-

[1] An arcsecond corresponds to 710−735 km at the center of the Sun's disk at perihelion and aphelion, respectively.

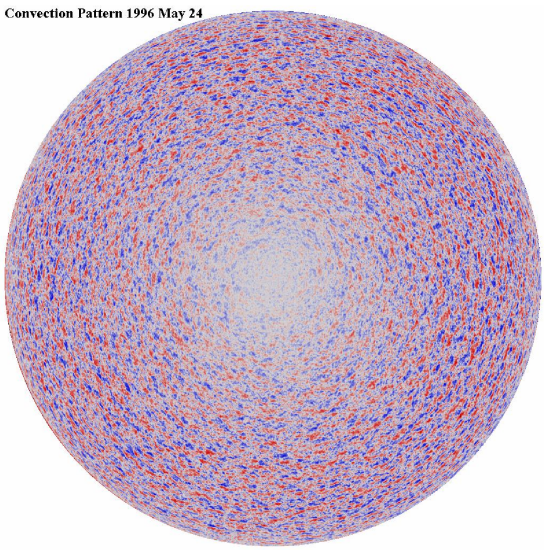

FIGURE 1.3:— Supergranular cells visible on Dopplergram image of solar disk. Blue color shows the upflow plasma, and red color is accompanied with plasma going down. Image is taken with MDI on board SOHO on May 24, 1996.

tally, the parcel encounters other similar expanding flows, and together they form dark and cold, intergranular lanes (Figure 1.2). From here the fluid moves downward.

Deeper in the convective zone, downflowing plasma located in intergranular lanes mix with upflowing diverging plasma. Because of interactions between downflows and upflows, only a small fraction of upflow plasma reaches the surface and cools down by radiation. A Significant portion of it turns over and cools down by mixing with downdraft plasma. The lowest layers of the convection zone heat the parcels that reach the bottom. The typical lifetime of granular cells is about a few minutes, with characteristic sizes in the range of 200-4000 km (Nordlund et al. 2009).

1.2.2 Supergranular cells

From granular scales, convective flow patterns crosses mesogranular scales (November et al. 1981; Roudier et al. 1999; Rieutord et al. 2000; Matloch et al. 2009; Yelles Chaouche et al. 2011) and reach supergranular ones (Rieutord & Rincon 2010).

Supergranules was first detected by Hart (1956), and later named by

Leighton et al. (1962). Their properties has been studied by many scientists since then. The characteristic size of supergranular cells is of the order of 12-50 Mm, with lifetimes of 20-50 h (DeRosa & Toomre 2004). Individual supergranules have flow speeds of about 0.5 km s^{-1} (Simon & Leighton 1964; Zwaan 1978; Rimmele & Schröter 1989; Shine et al. 2000). They can be seen in white light images or in line-of-sight Dopplergrams, magnetograms and images of chromospheric emissions, although they do not enclose completely supergranular cells. In Figure 1.3 a Dopplergram image of the solar disk on May 24, 1996 recorded by MDI on board the Solar and Heliospheric Observatory is shown. The image clearly demonstrates the cellular flows at large spatial scales. Gas moving upward is presented with blue color and descending flows with red color.

There are two physical models proposed to explain large scale convection (see review Rieutord & Rincon 2010). The first one is related to buoyancy forces as the main driver of the supergranulation. The second one implies that supergranulation emerges as a result of nonlinear interactions of granular motions at smaller scales (Rieutord et al. 2000). Still, understanding of convective motions at large scales is incomplete.

1.3 Quiet Sun magnetism

The solar magnetic field is organized on a wide range of spatial and temporal scales. At large scales, it is generated in the solar interior through global dynamo action (Parker 1955; Steenbeck & Krause 1969). The resulting magnetic field rises and reaches the atmosphere. The most conspicuous features visible on the solar surface are active regions, characterized by strong kilogauss magnetic fields (see Schrijver & Zwaan 2000). They are large magnetic structures with lifetimes spanning from several weeks to months. The properties of active regions are changing on the time scales of 11 years during which emergence rate of these structures change by a factor 8 (Hagenaar et al. 2003). At the maximum of the solar cycle, 6×10^{21} Mx day^{-1} emerge inside of active regions (Schrijver & Harvey 1994), usually appearing in pairs of opposite polarity structures orientated in the East-West direction.

Outside of active regions we observe the quiet Sun. In recent years it turned out that the QS is not quiet at all and represents a highly dynamical environment in which small magnetic features are continuously appearing on the surface. Thanks to their abundance it seems now that the

QS may have essential contribution to the solar magnetism. This idea is supported by observations of the coronal heating detected over the QS (see reviews by De Wijn et al. 2009; Sánchez Almeida & Martínez González 2011; Martínez Pillet 2013; Bellot Rubio & Orozco Suárez 2015).

The QS is formed by strong kilogauss fields located at the border of supergranular cells, called network (NE), and weak internetwork fields (IN) occupying the interiors of supergranules. In the following sections we will present in details their characteristics.

1.3.1 Network fields

NE fields are the most apparent magnetic features in the QS. Thanks to this, they have been examined thoroughly over the years and their properties are well known.

The distribution of NE fields coincides with the dominant large-scale convective motions − supergranulation (Leighton et al. 1962; Simon & Leighton 1964; Del Moro et al. 2007). They are usually created when the flux is dragged by horizontal flows from the inner parts of supergranular cells toward the edges (Orozco Suárez et al. 2012b; Giannattasio et al. 2013). Here, magnetic flux accumulates and creates NE elements. They adopt the form of concentrated, more or less discrete patches of magnetic flux. Since they are confined to the supergranular flows, they are very persistent and live a few hours before they are dispersed due to convective motions and interactions with nearby elements (see e.g., Iida et al. 2012, 2015). In Figure 1.4 (left panel) we show a magnetogram of the quiet Sun photosphere at disk center. A NE region encloses a supergranular cell, roughly marked with red solid line. Yellow arrows point toward some of the NE features.

Network patches have unsigned fluxes of 10^{18} up to a few times 10^{19} Mx (Martin 1988; Wang et al. 1995). They carry a total flux of $10^{23} - 10^{24}$ Mx over the entire solar surface (Simon et al. 2001; Hagenaar et al. 2003, 2008; Zhou et al. 2013), which is comparable to the total flux in active regions ($\sim 8 \times 10^{23}$ Mx at solar maximum; Schrijver & Harvey 1994). However, the presence of NE features is detected in only 10% of the Sun's area (Harvey-Angle 1993).

NE fields are strong, with intrinsic field strength in the kilogauss range and preferential vertical orientation of the field lines (see e.g., Stenflo 1973; Wiehr 1978; Solanki & Stenflo 1984; Stenflo & Harvey 1985; Solanki et al. 1987; Grossmann-Doerth et al. 1996). In higher photospheric layers and in

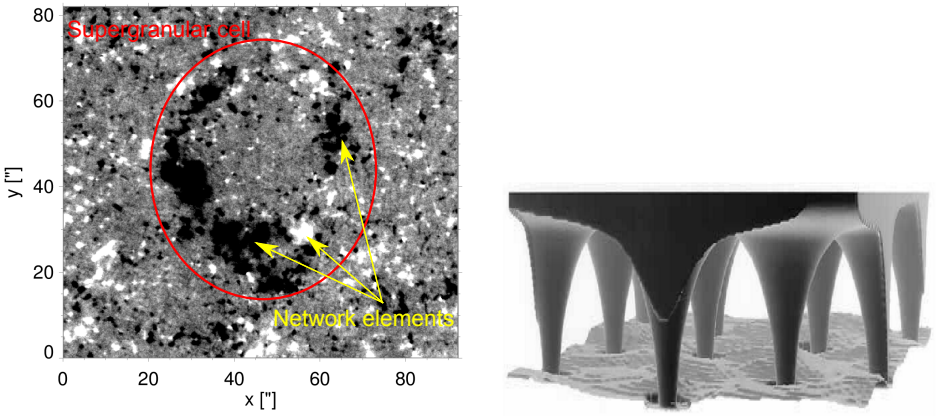

FIGURE 1.4:— *Left panel*: The image shows a longitudinal magnetogram of the solar surface where positive magnetic fields appear in white and negative fields in black. It was recorded on November 2, 2010 with the NFI on board Hinode at the solar disk center. Magnetic NE elements are visible as strong flux concentrations. Some of them are specified by yellow arrows. They are located at supergranular border enclosed with red line. *Right panel*: Magnetic elements with strong fields located at the border of supergranular cells, expand with height and form a magnetic canopy in the chromosphere. Image is taken from Schrijver & Zwaan (2000).

the chromosphere, the gas density and pressure decrease with height. As a consequence NE elements spread out horizontally to maintain pressure balance with the surroundings. Eventually, they merge with same polarity features at some height or create magnetic arches with opposite polarity ones. In this way at chromospheric heights, magnetic fields originating in supergranular lanes create magnetic canopies over supergranular cells. Such a magnetic configuration is presented in Figure 1.4 (right panel) for an unipolar area.

Internal structure of NE elements has been resolved for the first time by Martínez González et al. (2012a) using high resolution observation obtained with Imaging Magnetograph eXperiment (IMaX; Martínez Pillet et al. 2011) on board the SUNRISE balloon-borne solar observatory (Solanki et al. 2010; Barthol et al. 2011; Berkefeld et al. 2011). Apart from confirming the general description of NE structures, they discovered the presence of velocity fields above and below the canopy. Later, Requerey et al. (2014, 2015) provided detailed description of the processes by which QS magnetic features are intensified to kG fields and their subsequent

evolution, also using IMaX data.

Despite a lot of observational studies related to the properties and evolution of NE regions, their origin remains elusive. It is believed that the magnetic flux brought to the surface in active regions plays a minor role in formation of NE patches (Schrijver et al. 1997). Instead, ephemeral regions are considered to be their main source of flux. However, the coupling between NE and other QS magnetic structures, are not well understood. In this thesis, we will address this question.

1.3.2 Ephemeral regions

Besides active regions, the solar magnetic flux also emerges in nonactive or "quiet" areas. Flux rises to the surface on supergranular and mesogranular scales in the form of bipolar features called ephemeral regions (ERs). They are called "ephemeral" because of their short lifetimes of a few hours, typically 2 - 3 (Harvey & Martin 1973; Harvey et al. 1975a; Title 2000; Hagenaar 2001). This is significantly shorter than the lifetime of active regions.

ERs are discovered by Harvey & Martin (1973) who estimated that they have fluxes of about 10^{20} Mx and typical sizes of 30 Mm. A most intriguing result was the capability of ERs to bring to the solar surface as much flux as large active regions. This was the first step in understanding that a significant fraction of the solar magnetic flux is in the form of small-scale magnetic elements outside of active regions. In Figure 1.5 we give example of an ER recorded with the NFI on board Hinode on November 2, 2010. The region is marked with yellow line. During the emergence phase, ER shows its bipolar nature that slowly starts to disperse.

Over the years, ERs were studied using both, ground-based and space-borne observations. As a result, it is found that they preferentially appear at the edges of supergranular cells, but some of them may show up in the interior of the supergranules. Upon appearance on the solar surface, ERs rapidly expand at about 5 km s^{-1}, and slow down to 0.5-1.3 km s^{-1} in later phases of their evolution (Title 2000). With time, they migrate toward the NE and interact with flux patches there (Schrijver et al. 1997). The average unsigned flux of ERs is found to be in the range of 10^{18}-5×10^{19} Mx, following a power-law distribution which smoothly decreases toward larger structures, characteristic for active regions (Harvey & Zwaan 1993; Chae et al. 2001; Hagenaar et al. 2003; Thornton & Parnell 2010). This result, together with indications that ERs do not vary in phase with active

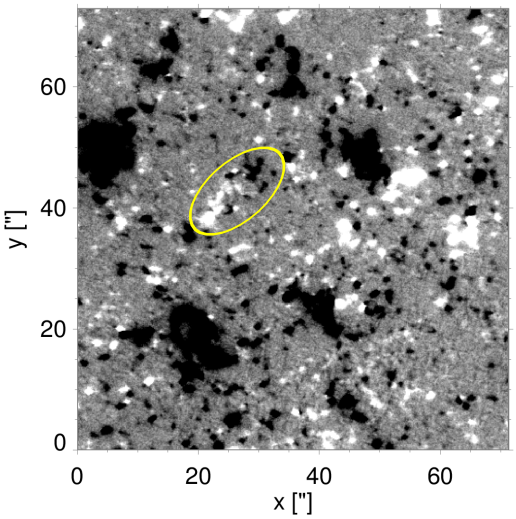

FIGURE 1.5:— Ephemeral region enclosed with yellow line appears inside of a supergranular cell. It emerges as a bipolar region consisting of some strong and many small magnetic patches. The data recorded on November 2, 2010 with Hinode/NFI.

regions, drove Hagenaar et al. (2003) to the conclusion that ERs originate not only from dispersal of active regions but also from some local mechanisms operating on small scales.

The emergence rate of ERs is estimated to be 3×10^{23} Mx day^{-1} (Harvey & Martin 1973; Harvey & Zwaan 1993; Title 2000; Hagenaar 2001; Chae et al. 2001). This is enough to completely replace the magnetic flux stored in NE elements in 1 to 200 hours (Wang 1988b; Martin 1990; Wang et al. 1992; Hagenaar 2001; Chae et al. 2001; Hagenaar et al. 2003, 2008). This is very intriguing result since it implies an enormous appearance rate of ERs. However, the limit of one hour for the flux replacement time has been extrapolated from low cadence observations, and has never been confirmed observationally. In fact, all the previous estimations are derived from observations with modest spatial and temporal resolutions, such as those from the Solar and Heliospheric Observatory (SOHO; Scherrer et al. 1995).

1.4 Internetwork fields

In the previous sections we introduced strong, long-lived magnetic features visible in the "quiet" solar photosphere, namely NE elements and ERs. On the other end of temporal and spatial scales, there are also small and weak magnetic concentrations - internetwork fields. They are distributed all over the solar surface, inside of supergranular cells. The properties of IN fields have been investigated for many years. Our knowledge about their field strengths or inclinations for example, has advanced significantly. However, due to lack of high sensitivity, high resolution observations that monitor IN regions over extended periods of time, their temporal evolution is still unknown. In what follows, we present what we learned about IN until now, and highlight the most important open questions.

1.4.1 Discovery of internetwork elements

Until the 1970's it was believed that the solar surface outside of active regions was a field free, denoted as the *quiet Sun*. During the 1970's solar community made a breakthrough in analyzing small-scale magnetic structures. Livingston & Harvey (1971) were the first authors to report the presence of background field of average strength 2-3 G, using the Kitt Peak magnetograph at spatial resolution of $5''$. They confirmed their result four years later indicating the presence of new component, *the inner network* or *internetwork fields* (Livingston & Harvey 1975; Smithson 1975). This new component was described as mixed polarities features, independent of surrounding NE elements but with a tendency to move toward them. IN elements were small in size and flux, containing only $10^{16} - 10^{17}$ Mx. Through years, their description of IN features turned to be very accurate and is valid even today. However, their lifetimes have been reduced down to approximately 2.1 min (Zhou et al. 2010). In Figure 1.6 we can see small magnetic patches surrounded by yellow circle. These weak patches are located inside of supergranular cells, representing IN fields. Outside of yellow circle, there are strong NE elements. Image is taken with Hinode/NFI at $0''.16$ with detection limit at 4 G.

1.4.2 Magnetic field strength and inclination

Until the Hinode era, IN fields could not be observed with space-borne instruments because of their poor spatial resolution and sensitivity. For

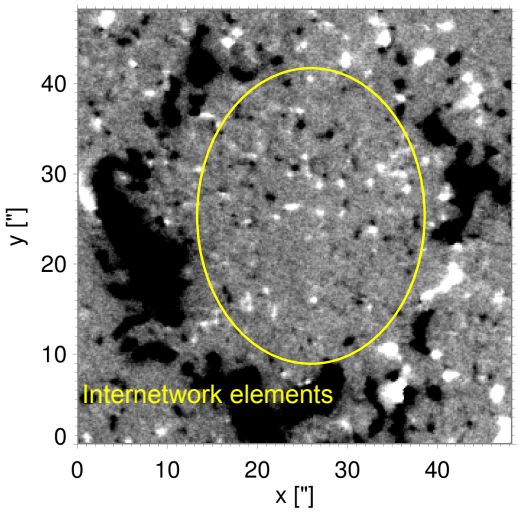

FIGURE 1.6:— Internetwork fields recorded on November 2, 2010 with Hinode/NFI at spatial resolution of 0″.16 and noise level of 6 G. They are located everywhere inside of supergranular cell, inside of area enclosed with yellow solid line.

example, SOHO can see only strong fields such as NE and ERs. The only possibility were ground-based telescopes. Unfortunately, the effects of the Earth's atmosphere and short temporal coverage compromise the measurements and interpretation of the observations. Thus, it was possible to study physical properties of IN fields but not their evolution.

Ground-based measurements make use of both, polarization signals generated by the Zeeman effect and scattering processes via the Hanle effect. The Zeeman effect provides quantitative measurements of the magnetic field vector, but suffers from the fact that polarization signals can be canceled if opposite polarity fields reside in the resolution element (Zirin 1985). Zeeman-based diagnostics made it possible to estimate the typical flux densities and magnetic field strength in the quiet Sun. They have been carried out in two spectral domains, in the Zeeman sensitive Fe I line pairs around 6302 Å and 15648 Å. While observations at 6302 Å suggest the presence of kG fields (Sánchez Almeida & Lites 2000; Domínguez Cerdeña et al. 2003; Socas-Navarro & Lites 2004), at 15648 Å the derived fields have hG strengths (Lin 1995; Lin & Rimmele 1999; Khomenko et al. 2003; Domínguez Cerdeña et al. 2006). The discrepancy between results

could not be reconciled at the time. Some authors suggested that visible and infrared lines sense different magnetic features (Sánchez Almeida & Lites 2000). On the other hand, Bellot Rubio & Collados (2003) argued that visible Fe I lines are more affected by noise than infrared ones. In addition to this, Martínez González et al. (2006) questioned the reliability of the thermodynamic and magnetic properties of IN fields derived from inversions of the Fe I lines. More confusion is brought into discussion with the results from López Ariste et al. (2002, 2006) who again estimated hG fields in internetwork areas, making use of the Zeeman effect in the Mn I 553 nm line. Their result was first confirmed by Asensio Ramos et al. (2007) and questioned later by Sánchez Almeida et al. (2008) who showed that Mn I line is biased to kG fields.

Solution to this debate was obtained when the Spectro-Polarimeter (SP; Lites et al. 2013) on board Hinode's Solar Optical Telescope (Kosugi et al. 2007; Tsuneta et al. 2008b) started to operate. Using Milne-Eddington inversions of the observations in Fe I 6300 Å lines, Orozco Suárez et al. (2007a,b) obtained mainly weak hG fields. This was confirmed by the following studies (Borrero & Kobel 2011a; Jin et al. 2012; Orozco Suárez & Bellot Rubio 2012). Martínez González et al. (2008) drawn the same conclusion from inversions of simultaneous visible and infrared observations.

Observations based on the Hanle effect in the Sr I line at 4607 Å and molecular lines show that IN elements appear to be turbulent magnetic fields in the range of 10 - 60 G (Stenflo 1982; Faurobert-Scholl et al. 1995; Faurobert et al. 2001; Stenflo et al. 1998; Trujillo Bueno et al. 2004; Bommier et al. 2005, 2006; Derouich et al. 2006). This type of diagnostic is not affected by cancellation of opposite polarities. However, a polarimetric accuracy of 10^{-4} is necessary for the detection of the Hanle effect, which requires very long exposure times. As a consequence, the spatial and temporal resolution of Hanle measurements are low.

Evidence of ubiquitous horizontal IN fields in the solar surface was reported for the first time by Lites et al. (1996a). They found horizontal features with lifetimes of few minutes. From the center-to-limb variations of the polarization signal in the quiet Sun, Martínez González et al. (2008) concluded that strong magnetic fields have a tendency to be vertically oriented while weak fields have a wider range of angles. The distribution of field inclinations obtained by Orozco Suárez et al. (2007a,b) clearly displays a peak around 90°, revealing the presence of horizontal fields. At

first, this result was confronted by the statement that most of the horizontal fields are induced by noise and not by real signal (De Wijn et al. 2009; Asensio Ramos 2009; Borrero & Kobel 2011a,b). Nevertheless, using high sensitivity Hinode/SP observations, Orozco Suárez & Bellot Rubio (2012) demonstrated that IN fields are indeed very inclined and on average weak. From statistical studies using Hinode data, it is found that horizontal magnetic elements are visible for not more than 10 minutes, occupying areas smaller than average granules (Ishikawa et al. 2008; Tsuneta et al. 2008a; Ishikawa & Tsuneta 2009b; Jin et al. 2009, see also Ishikawa et al. 2010; Ishikawa & Tsuneta 2009a)

1.4.3 Current knowledge on evolution of internetwork fields

As mentioned before, long duration, high resolution, high sensitivity observations are essential to understand the evolution of individual IN elements and their coupling with the surrounding NE and dynamics of supergranular cells. Obtaining such measurements is a very demanding task and could not achieved without Hinode. Thus, we do not know lot about the evolution of IN fields, but some very important analyses have been done. They gave us insights on appearance modes of IN fields, their possible effects on the higher atmospheric layers, and proper motions.

Emergence of IN fields

Thanks to the development of instrumentation and observing techniques, IN elements have been observed on scales less than 1 Mm. They emerge on the solar surface in the form of bipolar flux concentrations (called magnetic loops) (Harvey et al. 1975a; Zirin 1985; Centeno et al. 2007, see also, Lites et al. 1996a; De Pontieu 2002; Martínez González et al. 2007; Ishikawa et al. 2008; Jin et al. 2009; Guglielmino et al. 2012). Observationally, first appears linear polarization signal showing the top of the loop. It is followed by positive and negative circular polarization features in its proximity, which corresponds to vertical fields (known as footpoins of magnetic loop). After horizontal patch is disappeared, vertical fields are still visible to drift away from each other. Recently, Martínez González et al. (2012a) showed that magnetic loops do not appear uniformly over the solar surface. Similar findings have been reported by Stangalini (2014). According to their results, the loops preferentially appear closer to the edges of supergranular cells. Figure 1.7 shows the temporal evolution of

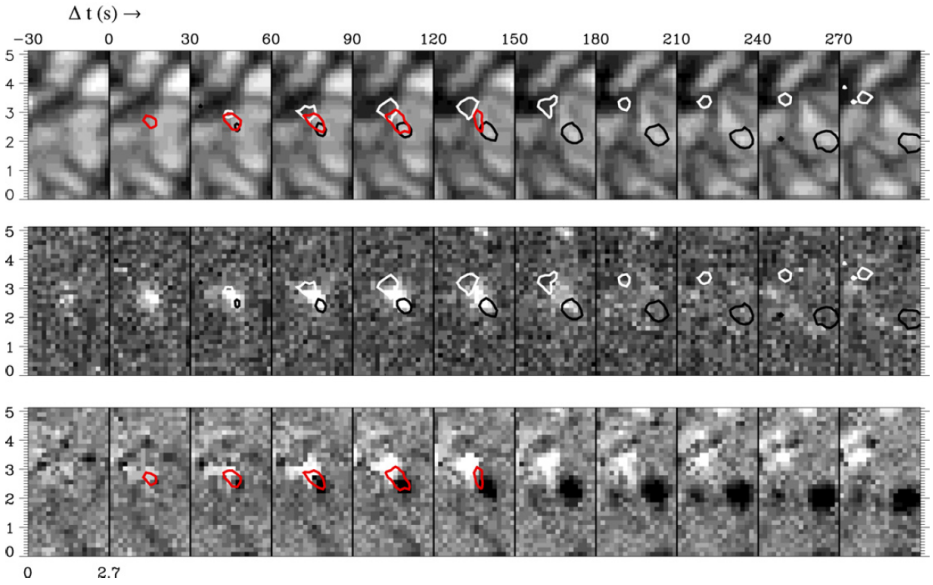

FIGURE 1.7:— Emergence of a small-scale magnetic loop in the IN as seen by the Hinode/SP. *Top panels:* continuum intensity maps. *Middle panels:* the evolution of total linear polarization signal. *Bottom panels:* circular polarization maps. Red contour enclose linear polarization signal (top of the loop), while black and white contours mark circular polarization (footpoins). Coordinates are given in arcsec. From Martínez González & Bellot Rubio (2009).

a typical magnetic loop in the IN (Martínez González & Bellot Rubio 2009). First, a linear polarization patch appears. It is soon followed by two circular polarization patches that separate from each other with time.

IN elements can also emerge as vertical magnetic fields in granules (Orozco Suárez et al. 2008) or they could appear as unipolar fields (Lamb et al. 2008, 2010). Unipolar fields imply that adjacent opposite polarity feature is not detected, which doesn't mean necessarily that it is not present at the surface.

All previously mentioned processes are result of interplay between magnetic fields and convective motions below or at the solar surface. Recently Danilović et al. (2010) and Pietarila et al. (2011) using numerical simulations suggested that photospheric magnetic concentrations can appear as descending magnetic fields dragged down from magnetic canopy.

From the observations that have been available until now, it is concluded that IN fields bring to the surface total unsigned flux of about 10^{15}

- 10^{18} Mx (Livingston & Harvey 1975; Zirin 1985, 1987; Keller et al. 1994; Wang et al. 1995). Up till now, there were only few attempts to determine their emergence rate. The values quoted in the literature range from 10^{24} Mx day^{-1} (Zirin 1987) to 4×10^{26} Mx day^{-1} (Thornton & Parnell 2010; Zhou et al. 2013). However, the published rates vary by more than 2 orders of magnitude, indicating that they are not well determined yet.

Disappearance of IN elements

Magnetic flux can disappear from the photosphere by fading or through cancellation. Fading has been reported to be the dominant process of the flux disappearance, accounting for 83% of the total flux removed from the quiet Sun (Lamb et al. 2013). These authors determined the flux disappearance rate of $2 - 4 \times 10^{24}$ Mx day^{-1} over the entire solar surface.

Cancellation of flux occurs when two opposite-polarity features come into close proximity leading to either flux removal by submergence below the photosphere or through lifting of a closed magnetic loop into the corona (Martin et al. 1985; Livi et al. 1985; Wang 1988b; Martin 1990, see also, Zwaan 1987). In both cases the observational signatures in magnetograms are the same: two opposite polarity patches approach each other, decreasing in size and strength, and eventually disappear below the detection limit.

Motions

At the photospheric level, internetwork elements are subject to granular buffeting. From the inner parts of supergranular cells they are dragged by net velocity toward network region. Tracking of magnetic elements revealed that velocities of IN elements have two components, one random, due to local buffeting and another radial toward the supergranular downdraft (Figure 1.8). Mean radial velocities have been reported by Zhang et al. (1998) to be around 0.4 km s^{-1} without variations with respect to distance from the center of supergranular cell. Using Hinode data de Wijn et al. (2008) reported net velocities of 0.2 km s^{-1}. Orozco Suárez et al. (2012a) studied for the first time the evolution of IN patches on supergranular time scale using Hinode observations. They obtained average value of 0.15 km s^{-1} with clear peak around 8″ away from the cell center.

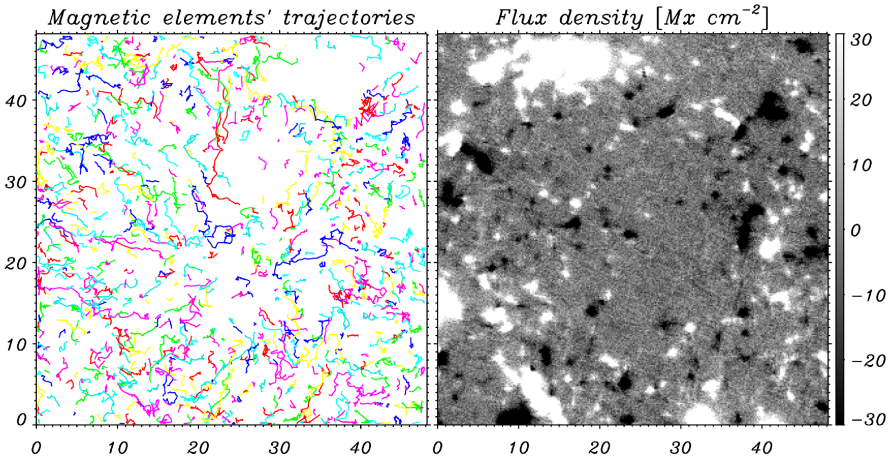

FIGURE 1.8:— Trajectories of few thousand magnetic elements tracked automatically for 13 hours (left panel). Two velocity components are distinguishable, random and radial toward supergranular border. Right: magnetogram calculated using data obtained with the Hinode/NFI. Network and internetwork fields are visible. The image is saturated at ± 30 G. From Orozco Suárez et al. (2012a).

Origin of internetwork fields

Regardless of the efforts made by the solar community, it is still unclear how IN elements are generated. Three mechanisms for creating internetwork magnetic fields have been proposed. According to Ploner et al. (2001) and De Wijn et al. (2005), small-scale magnetic fields in the QS may be debris from the decay of the large magnetic structures i.e., active and ERs. Some fraction of the magnetic flux could be dragged down by convective motions and appear again at some other place. The problem with this scenario is that the time scales of quiet and active magnetic fields are completely different. The characteristic replenishment time of IN magnetic flux is of order of few hours while active regions vary on scales of 11 years. In addition to this, the QS fields do not follow the same orientation as active regions (Hale's polarity law). Hagenaar et al. (2003), Parnell et al. (2009), and Thornton & Parnell (2010) indicate that the rate of flux emergence is independent of the solar cycle, hence a relation to active regions seems unlikely.

The second mechanism implies that magnetic fields are produced in deep layers by large-scale convective motions. In this way, IN magnetic fields would be generated in the same way as ERs (Harvey & Martin 1973;

Harvey et al. 1975b; Hagenaar 2001).

Another proposed solution is that IN fields are the result of a truly local, turbulent dynamo that operates at or just below the solar surface (Cattaneo 1999; Cattaneo & Hughes 2001; Vögler & Schüssler 2007). This local dynamo has been investigated with MHD simulations and it is found that does not depend on the global dynamo responsible for the creation of active regions. Models of turbulent dynamo are able to produce mixed polarity fields on scales smaller than are observed. The shortcoming of MHD simulations is that magnetic flux is clearly located in intergranular lanes while observations show that magnetic fields can appear at granular edges and above granules. At the surface, IN fields interact with pre-existing fields, which alters the magnetic properties of IN fields. Because of this, Stein et al. (2008) and Nordlund (2008) suggested that the turbulent dynamo does not operate at the surface but throughout the entire convection zone.

1.5 Internetwork fields: open questions

Despite a huge progress made in solar physics in recent years, the number of questions are still opened. In this section we will list those that are most important.

- *How and where magnetic elements appear in the solar atmosphere?* - We have seen that internetwork fields can appear as magnetic loops, above the granules, as unipolar fields or as horizontal fields. Nevertheless, due to only few analyses of emergence of internetwork fields we can not rule out the existence of additional forms. Regarding the unipolar fields, it is very intriguing that we have not been able to find the adjacent opposite-polarity patches, although the field lines have to return to the solar surface.
- *How small-scale magnetic fields are generated?* - We still do not know whether these fields appear due to convective motions from below the solar surface, are they the result of flux recycling, or they are generated by surface dynamo action.
- *What is the rate of appearance of magnetic patches?* - The appearance rate of internetwork fields is one of the less known parameters of the solar magnetism. Knowing this parameter we can better understand how the QS flux is maintained on the solar surface. Moreover,

accurate calculation of the appearance rate as a function of time and distance from the center of supergranules may help us understand better mechanisms responsible for formation of IN flux patches.

– *Evolution of IN elements* - Since long duration observations with high resolution and high sensitivity are very difficult to obtain, we do not know how IN elements evolve with time. Very little is known about their appearance phase, but their evolution on scale from minutes to days is even more obscured. Therefore, we do not know how internetwork flux evolve in time and space, does it vary with location within supergranular cells, how flux features interact with each other, etc.

– *Flux budget* - IN fields are very dynamic, short lived structures but very abundant. Thanks to this, they may have an important contribution to the total flux budget of the solar atmosphere and its energy budget. However, it is sill unknown how much flux carry the IN. Previously reported results are very broad and derived from moderate spatial resolution observations with moderate to none temporal coverage. Therefore, they are not reliable.

– *Interactions between IN and NE fields.* - This question has never been addressed before. The reason is the same, the lack of long duration, high resolution observations that are essential to capture the temporal evolution of IN fields on supergranular time scale. If we are able to understand how IN and NE elements interact with each other, we could estimate the IN flux contribution to the NE. This would give us the answer about the origin of NE fields but also shed light on importance of IN features for the QS magnetism.

– *How do magnetic elements disappear?* - The disappearance of magnetic patches from the surface implies the downward or upward retraction of magnetic field lines. Removal of magnetic flux from the surface might play an important role in energy transport to the chromosphere and corona. We already know that magnetic loops can reach chromospheric layers, but their influence on corona is still not clear. The possible mechanism for higher layers heating are cancellation processes but we do not know a lot about them.

1.6 Goals of the thesis

As we mentioned before, our understanding of the QS magnetism is very limited because observations suitable for investigation of weak and small IN features were not available until the Hinode mission. From ground-based observations it was possible to determine some of their properties but due to short temporal coverage of the solar surface, the temporal evolution of IN elements practically remained unknown. With Hinode observations, we finally got the opportunity to explore how the weakest and smallest flux patches in the QS evolve on scales from minutes to days. This is essential in order to understand their maintenance and contribution to the solar magnetism in general.

The main goal of this project is to understand how small-scale magnetic fields evolve with time and contribute to the QS magnetism. To respond to this questions we need high sensitivity, cadence and spatial resolution spectropolarimetric data. To track the evolution of the internetwork fields and the surrounding network region, this study also requires continuous, uninterrupted observations for many hours. Since the signal in the internetwork can be very weak it is necessary to obtain observations with long exposure times. On the other hand, we also need to achieve as high as possible cadence between filtergrams for tracking purpose. Employing the Hinode satellite, we have obtained data sets that are fulfilling all the requirements. In fact, our data sets represent the longest, high resolution observations of internetwork regions ever recorded with filtergrams. What makes our data even more unique is the sensitivity that has never been achieved before, nor later.

With these data sets we have for the first time the opportunity to study the evolution of individual NE and IN magnetic features from their birth to death on scale from minutes to days. Therefore, we can give answers to some of the open questions mentioned before.

- Evolution of IN elements - Making use of an improved automatic tracking, we will study for the first time histories of individual magnetic elements. In this way we can investigate their physical parameters, how they appear, interact and disappear.

- Flux budget - In this thesis we will determined how much flux is present on the solar surface in form of NE and IN flux concentrations and show their fluctuations with time.

– Interactions between IN and NE features - We investigate how IN fields interact with NE patches and change their flux. With this, we give a new insights on the origin of NE fields.

– Appearance and disappearance rates - With this thesis we give first and complete description how individual supergranular cells gain and lose flux. We estimate in a reliable way the rate at which IN flux appears and disappears in order to fully understand how the QS flux is maintained with time.

1.7 Outline of the thesis

We will now briefly outline the content of the thesis. The work is organized in seven chapters. Chapter 2 contains detail description of the data sets used in this thesis and how they are prepared. In Chapter 3 we summarize how automatic tracking codes work. We explain what are their main problems and describe the code we have developed to solve them. We study the flux budget of the QS in Chapter 4 and examine interactions between internetwork and network elements in Chapter 5. In Chapter 6 we investigate how internetwork flux appears and disappears from the solar surface. Chapter 7 summarizes our main results. In more details:

– In chapter 2 we present the Hinode satellite and its scientific instruments. Special attention is given to narrowband filtergraph whose observations are used in this project. In order to investigate the evolution of small-scale internetwork fields, we acquired high sensitivity, high cadence spectropolarimetric data. We describe the data sets in detail and also explain step by step the data reduction and calibration process.

– Chapter 3 firstly introduces the concepts of feature tracking algorithms and their implementation into automatic codes. Since tracking code used in this thesis has shortcomings, as any other automatic tracking code, it is not possible to determine the history of magnetic elements in a reliable way. This is essential for our work and therefore we developed a code that corrects errors made during the tracking process. Our code allow us to follow individual magnetic features from their birth to death, interpret their interactions and study their evolution for the first time.

– In Chapter 4 we analyze flux budget of the QS. To understand the temporal evolution of IN and NE flux and their respective contributions to the QS, we have to consider NE and IN elements separately. To identify them, we developed a method based on dynamical properties of supergranular cells and flux features. After internetwork and network patches are properly classified, we determine their histories employing magnetogram sequences that monitor the QS up to 40 hours. Then we study their physical properties required to calculate the fluxes they contain. These results gave us the opportunity to determine in a consistent way how the two populations contribute to the flux budget of the QS. We also analyze for the first time the flux evolution in individual supergranular cells.

– We study interactions between IN and NE features in Chapter 5. This is the first step in understanding what is the origin of the QS flux and how it is maintained on the solar surface. We track individual IN magnetic elements that reach the NE and identify interactions through which they can change the NE flux. In this way, we determine the total unsigned flux of IN patches deposited to the NE. We discuss about flux contributions from small-scale IN patches and ERs and about differences between these two populations. Our results point out that IN fields should be considered as the main source of flux for the NE and are capable of maintaining the QS flux in general.

– Description of how supergranular cells gain and lose flux is presented in Chapter 6. To understand the flux balance of IN regions we study the temporal evolution of two individual supergranules. We track all flux concentrations inside the cells and determine the modes how they appear and disappear. We then calculate the total IN flux appearance and disappearance rates. These rates are for the first time considered as functions of time and distance from the center of supergranular cells. With this, we explain in a consistent way how the IN flux is maintained on the solar surface.

– Finally, chapter 7 summarizes the work that is done in this project and provides conclusions.

2

Observations

The observations used in this thesis were obtained by the Narrowband Filter Imager (NFI) instrument on board the Japanese Hinode satellite. They show the evolution of magnetic flux patches in the quiet Sun at the disk center. These observations are unique because of their unprecedented spatial and temporal resolution and their very high sensitivity. As long-duration observations, they are ideal to study the highly dynamical quiet Sun magnetic fields on temporal scales from minutes to days. In this chapter we briefly describe the Hinode satellite, its NFI instrument, and give details of the acquired time sequences. We also provide a full description of the data reduction process and show examples of the final products.

2.1 Introduction

The quiet Sun harbors network fields at the borders of the supergranular cells, and internetwork fields in the cell interiors. As opposed to the network, internetwork fields produce small polarization signals, which makes them difficult to detect. Therefore, it is essential to perform high sensitivity measurements with high temporal and spatial resolution. However, to understand the quiet Sun magnetism this must be supported by long temporal coverage. The reason is that quiet Sun magnetic fields are also coupled with the evolution of supergranular cells. This requires continuous monitoring of the same supergranules for many hours.

Fulfilling all the requirements to study the quiet Sun is a very demanding task. In fact, this could not be achieved neither from the Earth nor space prior to the Hinode era. In the case of ground-based telescopes, it is possible to obtain high sensitivity observations but at the cost of temporal coverage and lower spatial resolution due to seeing effects. For instance, the POlarimetric LIttrow Spectrograph (POLIS; Beck et al. 2005) and the Tenerife Infrared Polarimeter II (TIP-II; Collados et al. 2007) achieve measurements with a spatial resolution of $0\farcs5$ and $0\farcs18$, respectively. In addition to this, such observations can last, at best, only five to six hours. This is not sufficient to investigate the spatial and temporal variations of quiet Sun fields.

The other option is to use observations from space-borne instruments. Their main advantage is the capability to provide a long duration sequences with large field of view. With relatively small interruptions, such instruments can observe the Sun for years. Still, it was impossible to study internetwork features before the Hinode mission. The reason is that all space observations had modest spatial resolution and/or polarimetric sensitivity. For example, internetwork features were completely invisible for SOHO, one of the most successful spacecrafts ever launched. With its angular resolution of $1\farcs25$, only network fields and ephemeral regions are accessible to SOHO. In this regard, nothing has changed even when the Helioseismic and Magnetic Imager (HMI; Scherrer et al. 2012)[1] onboard Solar Dynamics Observatory (SDO) started to observe the Sun with spatial resolution of $1''$.

Because all of this, we cannot use the previously obtained observations to achieve the goals posed in this thesis. To do that, we need completely new observations. They are obtained thanks to the Japanese *Hinode* spacecraft. It is capable of providing high sensitivity, high spatial and temporal resolution observations. When pushed to its limits, it is also possible to obtain time sequences with long temporal coverage, i.e., it is possible to study evolution of internetwork fields up to supergranular scales. Using the Hinode observations, in this thesis we describe for the first time how quiet Sun magnetic fields are maintained on the solar surface.

[1] HMI is an instrument onboard SDO dedicated to investigation of the origin of solar activity and understanding of the Sun's interior. It provides Dopplergrams, broadband continuum filtergrams, longitudinal and vector magnetograms.

2.2 General description of the Hinode spacecraft

The *Hinode* satellite (Kosugi et al. 2007), is a solar mission of the Japan Aerospace Exploration Agency's Institute Of Space and Astronautical Science (ISAS/JAXA). ISAS/JAXA was responsible for the design, development and testing. The National Astronomical Observatory of Japan (NAOJ), the National Aeronautics and Space Administration (NASA) and the Particle Physics and Astronomy Research Council (PPARC) were in charge of the scientific instruments and support for spacecraft development. The ground station support is the responsibility of the European Space Agency (ESA) together with JAXA and NASA. *Hinode* was launched on 22 September 2006. Since then, it has been providing seeing-free observations, with high-angular resolution. Such measurements result in larger polarization signals and less noise, compared to ground observations. The smaller influence of noise and the possibility of spatially resolving small magnetic elements makes the Hinode observations exceptionally useful to study the magnetic fields of the quiet Sun.

The scientific goals of the *Hinode* mission are to understand the processes of magnetic field generation, energy transport from the photosphere to the corona, and to determine the mechanisms responsible for eruptive phenomena such as flares and coronal mass ejections. To achieve these goals, the *Hinode* satellite carries three instruments:

- the Extreme ultraviolet Imaging Spectrometer (EIS);
- the X-Ray Telescope (XRT);
- the Solar Optical Telescope (SOT).

These telescopes usually have the same observational target, acting as a single "observatory". This gives the opportunity to observe the processes of interest in different layers of the solar atmosphere and different spectral regions at very high angular resolution. The XRT and EIS instruments are devoted to further our understanding of transient eruptive phenomena, and coupling between photosphere and corona. The emergence and evolution of magnetic structures in the solar photosphere and chromosphere are explored by the SOT.

In the next section we will focus on the SOT and its four instruments. One of them, the Narrowband Filter Imager (NFI), is of particular interest

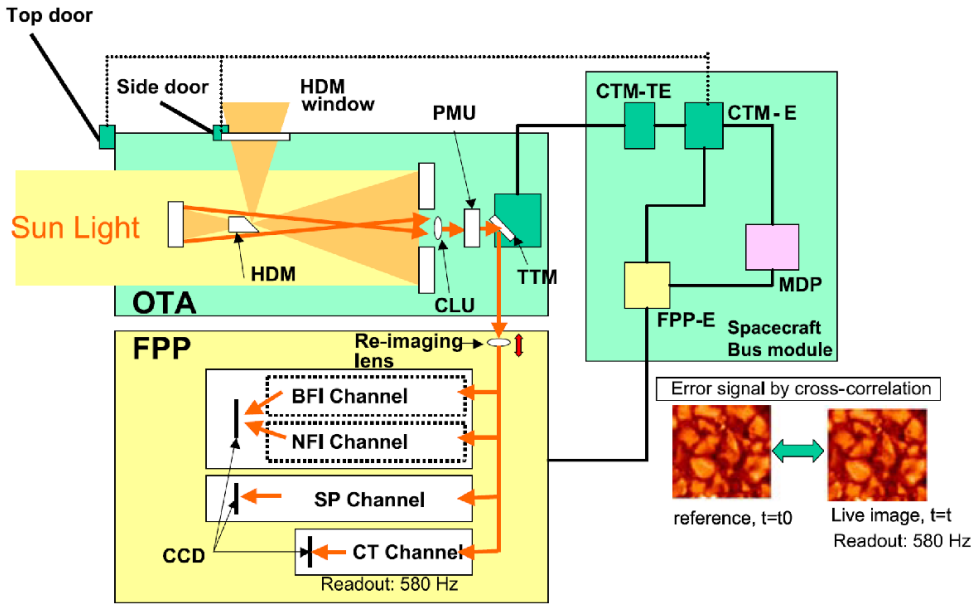

FIGURE 2.1:— The Hinode/SOT entire optical system. Optical Telescope Assembly (OTA), Focal Plane Package (FPP), Heat Dump Mirror (HDM), Collimator Lens Unit (CLU), Polarization Modulation Unit (PMU), Tip-tilt fold Mirror (CTM-TM), Broadband Filter Imager (BFI), Narrowband Filter Imager (NFI), Spectro Polarimeter (SP), Correlation Tracker (CT), Mission Data Processor (MDP), main electronics box for the FPP (FPP-E), main electronics box for the OTA and the CTM-TM (CTM-E), and analog driver for the CTM-TM (CTM-TE). The figure is taken from Tsuneta et al. 2008.

for this thesis and will be presented in (Section 2.3.1). The NFI observations analysed in this work are described in Section 2.4. We describe the complete data reduction process (Section 2.5) and conclude the chapter with a summary (Section 2.6).

2.3 The Solar Optical Telescope (SOT)

The SOT is the largest spaceborne optical telescope dedicated to solar observations. It provides quantitative measurements of the full vector magnetic field on spatial scales of 150-200 km with polarimetric accuracy better than 10^{-3}. The SOT consists of the Optical Telescope Assembly (OTA; Suematsu et al. 2008), and the Focal Plane Package (FPP), as shown in Figure 2.1. The OTA is a diffraction limited (0.″2-0.″3) Gregorian

telescope of 0.5 meter aperture (Tsuneta et al. 2008b). The OTA observes the Sun in the wavelength range from 380 nm to 670 nm. Field stops and heat rejection mirrors are located at the focus of the primary mirror and at the Gregorian focus (secondary focus). The secondary field stop limits the field of view to $361'' \times 197''$. The OTA also holds a collimating lens unit (CLU), a polarization modulator (PMU), and a tip-tilt mirror (CTM-TM) behind the primary mirror. The PMU is a continuously rotating retarder optimized for linear and circular polarization observations. With the CLU and the CTM-TM, the OTA provides a pointing-stabilized parallel beam to the FPP. The FPP has four instruments: the Spectro Polarimeter (SP), the Correlation Tracker (CT), Broadband Filter Imager (BFI), and Narrowband Filter Imager (NFI).

The SP is an off-axis Littrow echelle spectrograph that records dual-beam polarization spectra in the magnetically sensitive Fe I 6302.5 Å and 6301.5 Å lines. It provides observations of all four Stokes parameters - I, Q, U and V. The SP has four operational modes that provides observations at high spatial resolution ($0''.16$ pixels). Achieved polarimetric accuracy depend on working mode and can be as high as 0.1% but with cadence of the order of minutes. Higher cadences are possible but at the cost of lower sensitivity.

In order to avoid polarization crosstalk and reduce the spatial resolution degradation of magnetic field maps, Hinode uses the CT to maintain the stability of the images in the focal plane. It is accomplished using the correlation tracking algorithm applied on intensity maps. Just as the SP, the CT has its own CCD detector.

The BFI shares the same CCD detector with the NFI, and together, they constitute the Filtergraph (FG). The BFI employs interference filters to record diffraction-limited images, over the wavelength range from 3883 Å to 6684 Å. It observes both photospheric and chromospheric layers (blue, green, and red continuum measurements). The BFI provides observations at high spatial resolution ($0''.0541$/pixel) and rapid cadence (less than 10 s) over a $218'' \times 109''$ FOV. The typical exposure time is in the range from 0.03 to 0.8 seconds. With the BFI it is possible to make observations of horizontal motions and temperatures in the photosphere as well as observations in the UV wavelength range which permits mapping of strong magnetic fields.

The NFI is described in more detail in the following subsection.

TABLE 2.1:— The NFI spectral range specifications. For each spectral region we list the main spectral lines with their wavelengths, effective Lande-g factor (g_{eff}) and their purpose. Width of the tunable range is the same in all spectral regions.

Center (nm)	Width (nm)	Lines	g_{eff}	Purpose
517.2	0.6	Mg I b 517.27	1.75	Chromospheric Dopplergrams and magnetograms
525.0	0.6	Fe I 524.71	2.00	Photospheric Dopplergrams
		Fe I 525.02	3.00	
		Fe I 525.06	1.50	
557.6	0.6	Fe 557.61	0.00	Photospheric Dopplergrams
589.6	0.6	Na I D1 589.6	1.33	Photospheric and chromospheric (weak) fields
630.2	0.6	Fe I 630.15	1.67	Photospheric magnetograms
		Fe I 630.25	2.50	
		Fe I 630.38	0.92	Umbral magnetograms
656.3	0.6	H I 656.28		Chromospheric structures

2.3.1 Narrowband Filter Imager (NFI)

The NFI is a tunable birefringent Lyot filter with selectable bandpass used to perform full Stokes polarimetric imaging. From these observations one can derive intensity maps, and longitudinal and transverse magnetograms. The highest spatial resolution provided by NFI is $0''.08$ per pixel in the spectral range 5170-6570 Å. This wavelength range is divided into 6 regions containing 10 lines that cover the photosphere and lower chromosphere. Each spectral region is selected by a wide-band interference filter preceding the Lyot filter. The Lyot filter itself is sufficiently narrow for magnetogram and Dopplergram measurements. However, it can be tuned within ±4 Å around the main spectral lines to measure the nearby continuum or even other spectral lines present within this region. The default spectral line for longitudinal magnetic and Doppler observations is Na I D1 5896 Å. This line provides a higher light level (and its prefilter is not damaged by UV radiation). In Table 2.1 we summarize the characteristics of each spectral region, providing their central wavelengths, the tuning range, the main spectral lines, th effective Landé factors ($g_{\rm eff}$) and possible usage of the lines.

The FOV of the NFI is $264'' \times 164''$, due to vignetting caused by limited size of the optical elements. Typical exposure times are in the range from 0.1 to 1.6 s. The spectral resolution is 60-100 mÅ with a polarization precision of 0.4%. The NFI shares with the BFI a 4096×2048 CCD detector, whose pixels can be summed as 1×1, 2×2 or 4×4. The observations are normally done in one spectral line using only one or a small number of wavelength samples, for extended period of time.

Figure 2.1 shows the light path to the NFI. The light goes from the CLU through the PMU and is reflected on the CTM-TM to the re-imaging lens. Behind it, there is a nonpolarizing beam splitter that divides the light between the SP and the filtergraph. Then the polarizing beam splitter in the filter channel transmits the p-polarized light to the NFI and the s-polarized light to the BFI. At the exit of the NFI, light is collected on the CCD detector.

There are two modes in which NFI can operate in order to obtain Stokes vector images: shuttered and shutterless mode. In the shuttered mode, the mechanical shutter is synchronized with the PMU and controls the exposure of the CCD detector. The exposure time in this mode is fixed at 0.1 s. To acquire a full set of Stokes images, 20 s are necessary.

In shutterless mode, the mechanical shutter is left open and a mask is inserted in the focal plane in order to mask out the outer areas of the CCD. In this way, the FOV is reduced to a narrow vertical strip at the center of the CCD chip. The CCD is continuously read out in synchrony with the PMU, accumulating charge in the central strip, and shifting it under the focal plane mask. Since the left and right halves of the CCD are not read at the same moment, there is a slight time delay between them. After the strip images are received from the CCD, they are added or subtracted in the smart memory buffers of the FPP to create the various Stokes images.

The polarization states are modulated by the PMU in the OTA and analyzed by a polarizer in the NFI. To create the Stokes I and V images, exposures are integrated over a given number of rotation phases of the PMU. Possible exposure times are 0.1, 0.2 or 0.4 s. The full FOV can be observed only when 2×2 or 4×4 summing is employed. At full resolution, the FOV is limited to the central 1K×2K pixels or $82'' \times 164''$. While in shutterless mode, the NFI can achieve very high sensitivity due to a larger duty cycle (exposure time/total cycle time), but at the cost of a reduced FOV. If deemed necessary, the FOV can be increased by reading out and combining different strips on the CCD detector into single images, which on the other side reduces the time cadence. In Table 2.2 we list all possible shutterless modes with their exposure time, pixel size, summation and FOV. The NFI regularly records Stokes I, Q, U and V images or a combination thereof. The Stokes V filtergrams give the location, the polarity, and an estimation of the flux of the magnetic field component along the line of sight (LOS).

TABLE 2.2:— NFI shutterless mode observable Stokes parameters with FOV and CCD characteristics.

Exposure and observables	Pixel size (summing)	CCD read size	FOV
0.1 sec exposure for	$0.08''$ (1×1)	64×2048	$5.2'' \times 164''$
I, Q, U, and V measurements	$0.16''$ (2×2)	160×2048	$12.8'' \times 164''$
	$0.32''$ (4×4)	320×2048	$25.6'' \times 164''$
0.2 sec exposure	$0.08''$ (1×1)	192×2048	$15.4'' \times 164''$
I, U, V or I, Q or I, V	$0.16''$ (2×2)	384×2048	$30.7'' \times 164''$
	$0.32''$ (4×4)	768×2048	$61.4'' \times 164''$
0.4 sec exposure	$0.08''$ (1×1)	400×2048	$32.0'' \times 164''$
I, V	$0.16''$ (2×2)	800×2048	$64.0'' \times 164''$
	$0.32''$ (4×4)	1600×2048	$128.0'' \times 164''$

The NFI data reduction is implemented in the IDL SolarSoft[2] package. However, for our particular data sets, flat field and dark frames are not available. Because of this, and uniqueness of our data, we decided to prepare the data sets following the method described in detail in sections below. This approach also gives us a chance to increase the quality of the final data products.

2.4 Hinode Operation Plan 151

HOP 151 is an observational proposal submitted by Bellot Rubio, Orozco Suárez and Katsukawa under the name *Flux replacement in the photospheric network and internetwork*. Observational proposals and scientific objectives are approved and set during regular planning meetings of the Hinode's operation team. HOP 151 was accepted on December 17, 2009.

The main goal of HOP 151 is to study how the quiet Sun is continuously replenished by new small-scale magnetic flux patches appearing on the solar surface. This requires the satellite to continuously follow the evolution of the same supergranular cell near the disk center, from birth to death without interruptions. If an interruption occurs, the observations must be resumed from the same position to continue the tracking of the same supergranular cells. To have the highest possible signal-to-noise ratio, which is essential for detection of the weakest magnetic elements,

[2]SolarSoft is a set of integrated software libraries, data bases, and system utilities which provide a common programming and data analysis environment for Solar Physics and can be accessed at `http://www.lmsal.com/solarsoft/`

HOP 151 requested the longest possible exposure time for the NFI.

HOP 151 uses only NFI shutterless I and V observations plus Ca II filtergrams recorded every 3 hours for co-alignment. Observations were taken in the Na I D1 resonance line at 5896 Å at 2 wavelengths: ±160 mÅ from the line center. The request to XRT was deep integrations with the cooler filters (thin-Al-mesh or thin-Al-poly) for quiet Sun observations. The FOV had to be larger than $128'' \times 128''$, and the temporal cadence as high as telemetry permitted. Regarding the EIS, long exposure observations in the coolest lines were requested.

Details of the measurements proposed in the framework of HOP 151 are summarized below:

- observations are done in the NFI Na I D1 line at 5896 Å at two wavelengths (± 160 mÅ from the line center);
- the NFI is operated in shutterless mode where only I and V images are recorded, with 0.2 sec exposure time per image;
- to increase the effective exposure time, 8 integration cycles of the PMU are used;
- to observe a FOV of $93'' \times 82''$, three strips on the CCD are read and combined into a single image during the data reduction process;
- the compression level for I images is JPEG Q65 (2.3 bits/pix), while almost no compression (5.1 bits/pix) is used for V images in order to preserve very weak polarization signals;
- The cadence is 1.5 minutes or less for magnetic feature tracking;
- telemetry rate is 12 images every 1.5 minutes (2 Stokes parameters × 2 wavelengths × 3 strips on CCD);
- Ca II H filtergrams are took every 3 hours for image co-alignment between different instruments.

2.4.1 Description of data

In this section we describe all data sets obtained in the framework of HOP 151. This observational proposal has been run five times until now (see Table 2.3). The observed spectral line, Na I D1 589.6 nm is shown in Figure 2.2. In the left panel we show the intensity profile, extracted from the

TABLE 2.3:— HOP 151 runs performed until 2011

	Set #1	Set #2	Set #3	Set #4	Set #5
Date	20 Jan 2010	28 Feb 2010	20 Apr 2010	02 Nov 2010	26 Dec 2010
Starting time	13:56:34	05:20:41	09:43:33	04:02:33	19:00:03
Duration [h]	20	36	41	38.5	37
FOV [pixels]	576 × 768	576 × 512	576 × 512	576 × 512	576 × 512
Cadence [s]	50-70	50-70	80	90	90
Number of gaps	2	7	1	2	1
Duration of gaps	00:06:00	00:53:12	00:16:00	01:01:30	00:31:30
	00:29:11	00:19:00		00:31:31	
		00:21:12			
		00:12:00			
		00:04:00			
		00:23:00			
		00:23:00			
Longest continuous interval [h]	11.2	12.8	29.3	24.9	19.1
Available data	Na I D1 line	Na I D1 line	Na I D1 line	Na I D1 line	Na I D1 line
	EIS*	EIS*	EIS*	EIS*	EIS*
		Ca II H		Ca II H	Ca II H
		Ti-poly	Ti-poly	Ti-poly	Ti-poly
		Al-mesh			Al-mesh

* - Observations in Fe XI, Fe XII, He II, Fe XVI, Mg VI, Fe XIV, Si VII and Fe XV lines.

Fourier Transform Spectrometer Atlas of the QS (Brault & Neckel 1987), and normalized to the local continuum. Red vertical lines correspond to ±160 mÅ. In the case of weak magnetic fields, the Stokes V profile is proportional to the first derivative of the intensity profile (see Unno 1956; Landi Degl'Innocenti & Landi Degl'Innocenti 1973). We calculate the V profile as $\mathrm{d}I/\mathrm{d}\lambda$ and plot the result in the right panel. It can be seen that the observations were taken at two wavelengths that are symmetrically positioned in the line wings with respect to the core, thereby providing approximately the same amount of light during the observations.

To create I and V at each wavelength position, eight pairs of I+V and I-V images were recorded in synchrony with the PMU and summed up. Since individual exposure times are 0.2 s, this gives a total integration time of 6.4 s per line scan (16 images × 2 line wings × 0.2 s/image = 6.4 s). Three contiguous regions were recorded consecutively and processed together to make up the final FOV. The data sequence recorded in January has the largest FOV of 576×512 pixels (92″×123″). The FOV in the other runs is slightly smaller and has the same dimensions of 576×512 pixels (92″×82″).

The shortest data sequence was obtained in the first observational run (20 January 2010) and the longest one in the third (20 April 2010). The

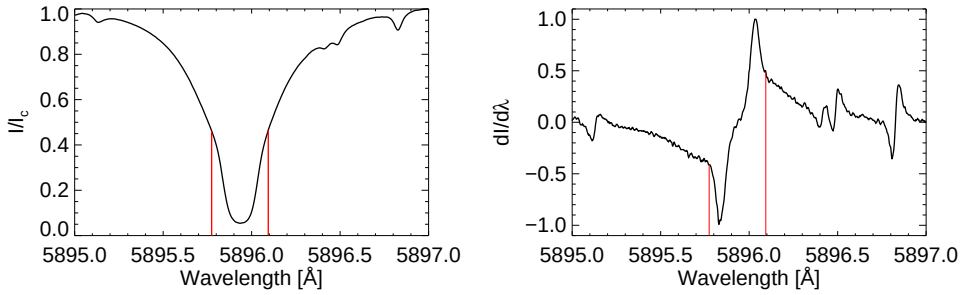

FIGURE 2.2:— Na I D1 line taken from the Kitt Peak FTS-Spectral-Atlas (Brault & Neckel 1987). The Stokes I profile is presented in left panel and its first derivative (proportional to the Stokes V profile) on the right one. Vertical red lines corresponds to ± 160 mÅ from the line center.

data sequences in the first and second runs do not have a constant cadence, varying from 50 to 70 s. In all other cases, the cadence is either 80 or 90 seconds. Unfortunately, there are gaps in each observational sequence that can not be recovered. They were caused by transmission problems and/or data recorder overflows. As can be seen from Table 2.3, these gaps normally last less than 30 min, except for the second and third run that each suffered an interruption of about 1 hour.

Simultaneously with the NFI observations, the BFI provided low chromospheric Ca II H observations in the second, fourth and fifth run. In addition to this, EIS observations are available for all runs and XRT for data sets 2 and 5 (Ti-poly and Al-mesh), and partially for set 3 and 4 (Ti-poly).

2.5 Data reduction

The observations downloaded from the satellite to the ground stations have the status of "raw data". The raw data are stored in the SIRIUS database at ISAS/JAXA in the CCSDS packet format, from which each instrument team makes FITS files. Such FITS files are Hinode Level-0 data, and can be accessed by the community through the Hinode data archives. One of these archives is the "Hinode Science Data Center Europe"[3], maintained by the Institute of Theoretical Astrophysics at the University of Oslo, Norway. The Level-0 data are not calibrated.

[3]This archive is located at following web address: `http://sdc.uio.no/search/API`.

To create magnetogram and Dopplergram time sequences from the raw data, there are several steps that need to be performed:

- Arrangement of the FITS files into single images;
- Recovery of lost telemetry packets;
- Flat-field correction;
- Removal of systematic signal changes due to Hinode orbital variations;
- Image alignment and trimming to the common FOV;
- Filtering 5-min photospheric oscillations;
- Calibration of the magnetograms and Dopplergrams.

In what follows, we describe each of these steps in detail.

2.5.1 Arrangement of the NFI FITS files

Information about the images stored in FITS format can be extracted from the headers. One NFI FITS file contains an I and V image pair at one wavelength. Due to the limited bit depth (from -2^{15} to 2^{15}-1), the intensity images have to be corrected for possible wrap-arounds. Each I and V pair corresponds to a strip or "Region of Interest" (ROI), which can take values 1, 2 or 3. To make a single I or V map for the full FOV, we have to take 3 consecutive FITS files and combine their three ROIs in the proper way. An example is shown in Figure 2.3. From three FITS files we extract the V images. Each V image is divided into two vertical slices of equal size (dashed lines in the upper panel). These slices are then arranged according to their ROI values as indicated with arrows. The same holds for I images. This procedure is repeated for all FITS files. Figure 2.4 shows examples of arranged images at both wavelengths. The panels on the left side are intensity (upper) and circular polarization (bottom) maps at -160 mÅ from the line core. Panels on the right side show intensity and circular polarization maps obtained at +160 mÅ. The intensity maps are normalized to their respective mean values.

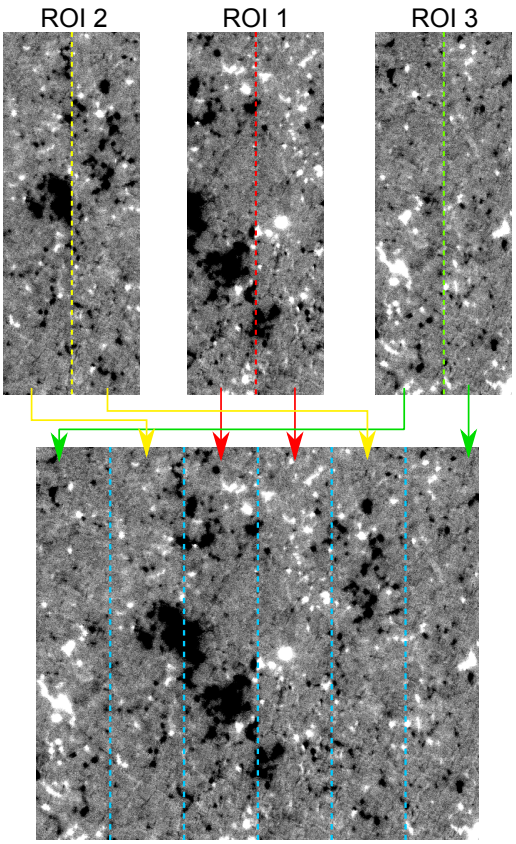

FIGURE 2.3:— From three FITS files, filtergrams are extracted and divided into slices (dashed lines). According to the ROI values of each image, we arrange the slices into a single image (arrows indicate how slices are combined).

2.5.2 Recovery of lost telemetry packets

During the data downlink some telemetry packets can be lost, which produces empty strips in the filtergrams. We recover these strips whenever possible, which is essential for tracking magnetic features. Unfortunately, the recovered areas often have larger noise levels. Since the procedure to recover the missing signal is not the same for I and V maps, we will first describe the case of I maps.

In Figure 2.5 (a), we show an example of a damaged Stokes I map. To recover the missing part, we take the corresponding regions in the two closest I maps of the same wavelength (one before the damaged image and another after it), provided these parts are not effected by telemetry

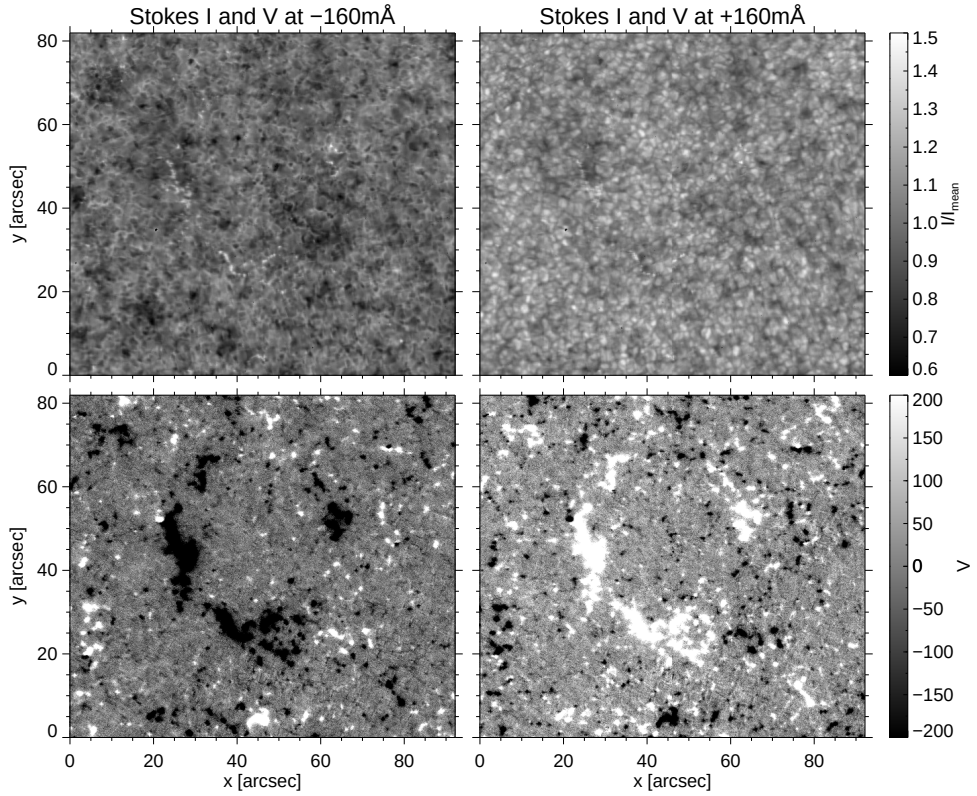

FIGURE 2.4:— Examples of intensity and circular polarization maps after FITS files are properly arranged. The panels on the left side correspond to −160 mÅ from the line core, and the panels on the right side to +160 mÅ. The images are taken from Set 4 on November 2, 2010.

problems. In this particular case, the closest good images are the previous and following ones. Then we calculate the average of the selected areas and replace the missing strip with it. Since the mean intensity of the recovered area can be different from the rest of the image, we scale its intensity so that the mean values are equal across the FOV. The result is presented in panel (b) of Figure 2.5 where the missing strip is enclosed with red box. If the closest image is three or more frames away from the damaged image, we just copy the corresponding area without any additional calculation.

In the case of V maps, the situation is better since we can also use the images taken at the other wavelength. For example, if there is a missing part in one Stokes V image, the first step is to check for the same area in

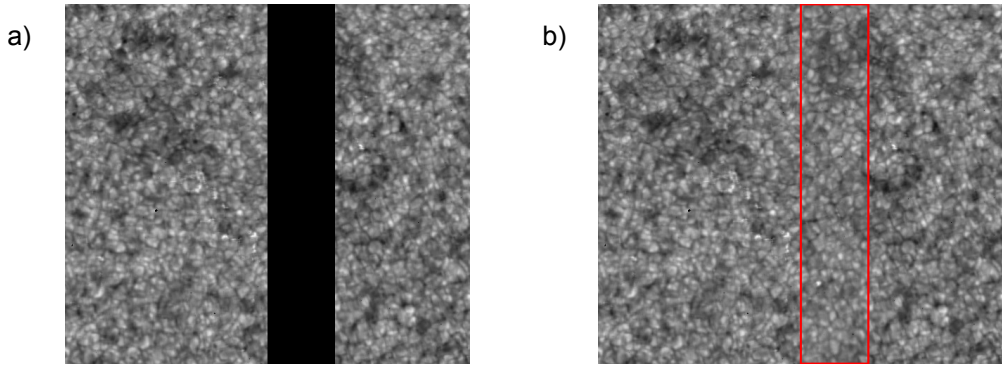

FIGURE 2.5:— Intensity map with missing area (a) and the same map with missing area recovered using the closest intensity maps where corresponding areas are present (b).

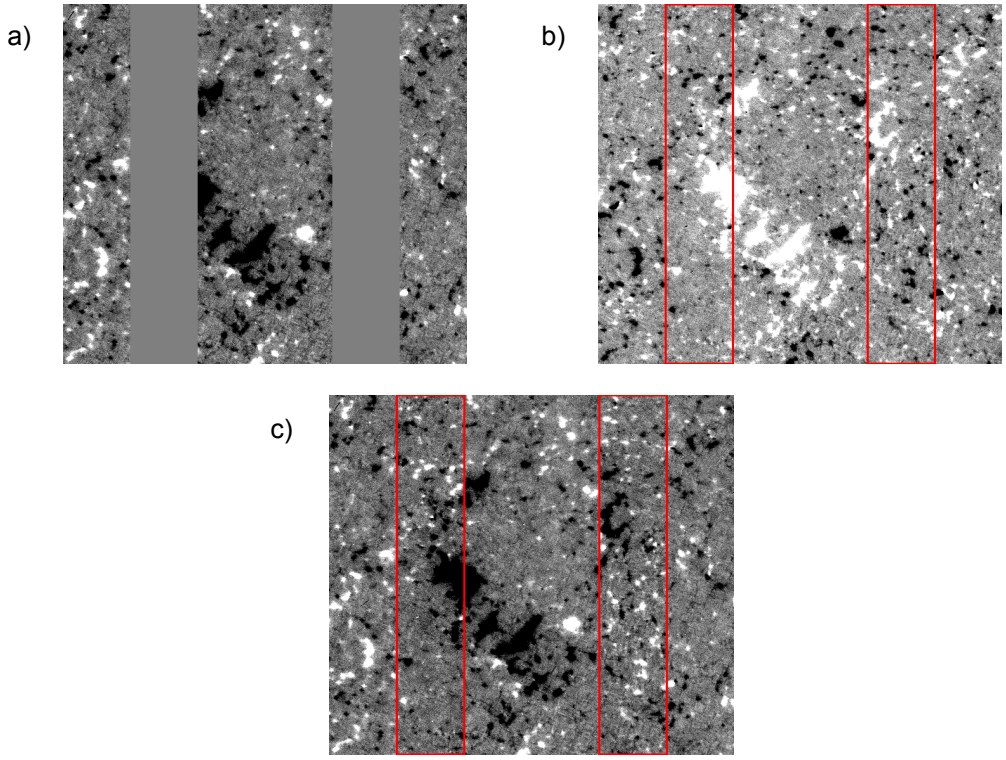

FIGURE 2.6:— Missing strips in Stokes V filtergram (a) are recovered using the signal at the other wavelength (b). The sign of the corresponding parts from image (b) is reversed and such parts are inserted at the positions where the signal in image (a) is missing, as highlighted with red boxes in panel (c).

the image corresponding to the other wavelength. If that image is in good condition, it is sufficient to extract the area of interest, invert the polarity and use it to fill in the missing part in the first image. An example is shown in Figure 2.6. In the selected V map at −160 mÅ (Figure 2.6a), there are two missing strips. The V map at +160 mÅ (panel b) is in good condition so we take the corresponding areas (red boxes), reverse their sign and use them to replace the missing parts of the image at −160 mÅ (c).

If the image at the other wavelength is also damaged, we use the same strategy as for the intensity map. We search for the closest images where the corresponding areas are in good condition and calculate average values with which we replace the missing areas. The only difference is that we can use both wavelengths. If the closest image corresponds to the other wavelength, we reverse the polarity of that image prior to any replacement.

2.5.3 Flat-field correction

Due to the presence of moving air or oil bubbles in the index-matching fluid in the tunable filter, flat-field frames taken with the NFI cannot be used for long-duration observations. Because of this, they are not taken for the HOP 151 observations. Instead, we generate gain tables for each wavelength by averaging all the corresponding intensity filtergrams (upper panels in Figure 2.7). Such "flat-field" images are then used to correct the intensity maps. As can be seen, they do not show solar features. The reason is that the duration of our observations significantly exceed the granule lifetime. Therefore, after averaging thousands of images, that cover up to 40 hours of observations of the same FOV, only persistent structures that are not of the solar origin remain visible. Corrected intensity filtergrams are shown in the bottom panels of Figure 2.7. Comparing them with those without corrections in Figure 2.4, it can be seen that artifacts caused by the bubbles in the tunable filter are successfully removed. Flat-field images are calculated for each observational sequence separately. Since Stokes V is defined as the intensity difference between measurements of clockwise and counterclockwise circularly polarized light, we apply this flat-field correction to V filtergrams too.

Once all the filtergram images of a sequence are prepared, we calculate magnetograms and Dopplergrams from them. LOS magnetograms are calculated by the ratio of I and V images that are obtained combining multiple filtergrams onboard. Since we performed observations at two

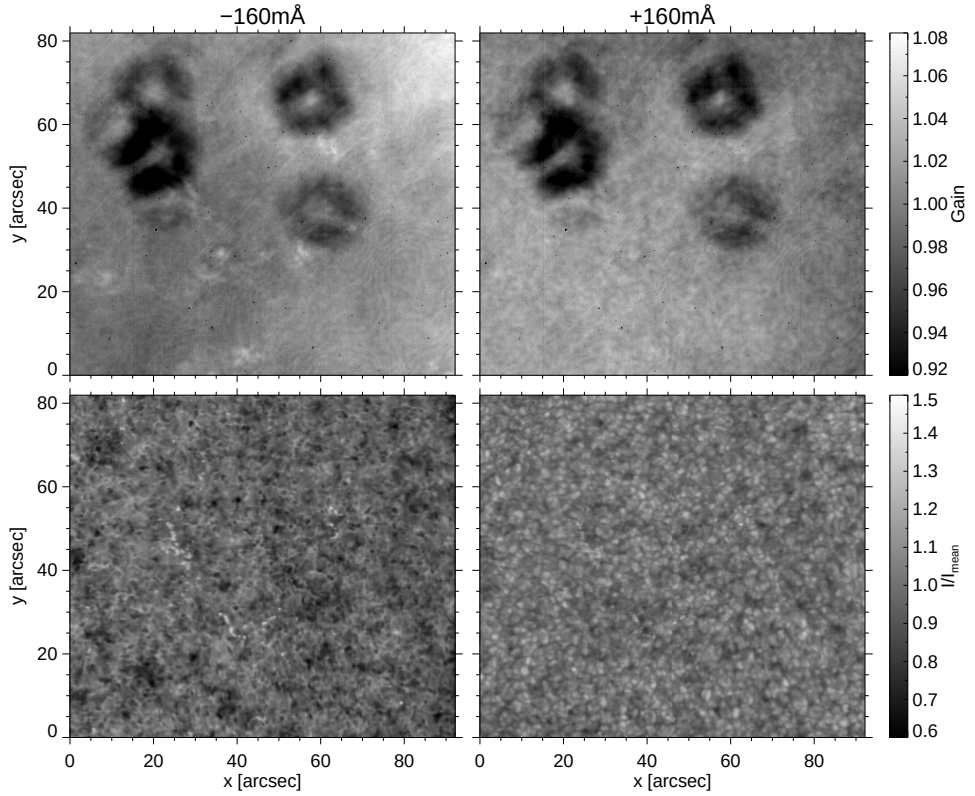

FIGURE 2.7:— Top: Flat-field images derived by averaging all intensity maps for a given wavelength. Bottom: Intensity maps at −160 mÅ and +160 mÅ after flat-field correction.

wavelengths to avoid contaminations of magnetograms by Doppler shifts, we compute the magnetogram signal as:

$$\mathrm{M} = \frac{1}{2}\left(\frac{V_{\mathrm{blue}}}{I_{\mathrm{blue}}} - \frac{V_{\mathrm{red}}}{I_{\mathrm{red}}}\right), \tag{2.1}$$

where "blue" refers to the measurements in the blue wing of the line (-160 mÅ) and "red" to those in the red wing (+160 mÅ).

Dopplergrams (LOS velocity maps) can be derived from any of the spectral lines observed by the NFI. These maps are computed as the ratio of the difference of blue and red wing intensity maps (Stokes I), divided by their sum:

$$\mathrm{D} = \frac{I_{\mathrm{blue}} - I_{\mathrm{red}}}{I_{\mathrm{blue}} + I_{\mathrm{red}}}. \tag{2.2}$$

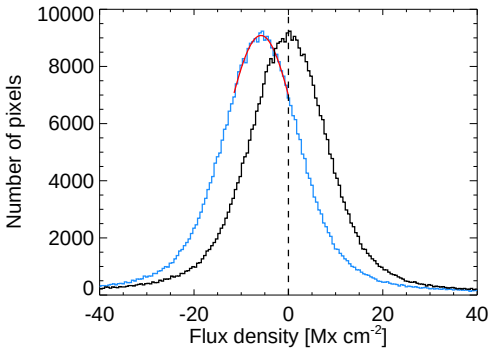

FIGURE 2.8— Distribution function of the magnetogram signal in one of the halves of an NFI magnetogram. The blue solid curve represents the distribution function before correction. The black solid curve shows the same distribution after setting its central position to zero. The red solid curve show a Gaussian fit to the core of the distribution.

The estimated 1σ noise level of NFI Dopplergrams produced in this way is 30 m/s for a Dopplergram formed with $0.16''$ pixels (2×2 summing) with a 0.8 second exposure time.

2.5.4 Systematic changes of magnetogram signal due to Hinode orbital motion

Magnetograms may have systematic changes of the signal resulting from orbital variations of the spacecraft. To remove them, we calculated the distribution of magnetic flux densities for each frame. However, this had to be done separately for the left and right halves of magnetograms because they have different offsets of the background signal, but not the scale of values.

The method is illustrated in Figure 2.8. Here we determine the flux density distribution in one of the halves of a magnetogram image (blue solid curve) and fit its core with a Gaussian, assuming that it represents photon noise (red curve). Any deviation of the central position of the Gaussian from zero was subtracted from all the pixels of the corresponding half frame. The shifted distribution function is shown with the black solid curve. The observed offsets are periodic and show rms values of less than 1.4 G.

2.5.5 Image alignment and trimming

The next step in the reduction process is to align the image sequences. To do this, we first calculate auto-correlation between two consecutive

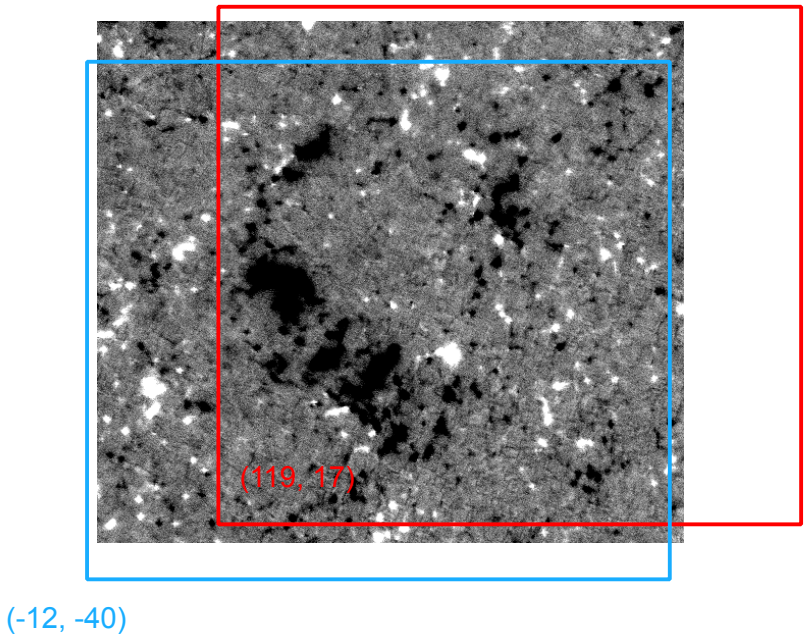

FIGURE 2.9:— Images are aligned and trimmed in order to preserve parts that overlap during the entire sequence. Blue and red boxes show the maximum shifts in the negative and positive X- and Y- directions, respectively. Blue and red numbers are shifts expressed in number pixels.

images to find the offset between them. Then, to align the images we use the Fourier shift theorem[4] which says that if a function is translated by a certain amount, the translation appears in the phase of the Fourier transform. This means that if two images are shifted with respect to each other by some displacement (x, y), they can be aligned in Fourier domain assuming that the shift in the phase domain corresponds to the shift between images in the spatial domain. Because it is easier to overlap objects in magnetograms than in Dopplergrams or intensity maps, we calculate the offsets using the magnetograms. We then align the magnetograms, Dopplergrams and intensity maps, using these offsets.

Due to slow drifts of the FOV, not all parts of the images overlap. To track magnetic features, we trimmed the images in order to preserve the parts that overlap during the entire time sequence. To this purpose, we used the maximum shifts in positive and negative directions along the

[4]We use the IDL procedure `xshift.pro`, written by Paul Seagraves. It can be found at: `http://download.hao.ucar.edu/pub/lites/asp_idl/xshift.pro`.

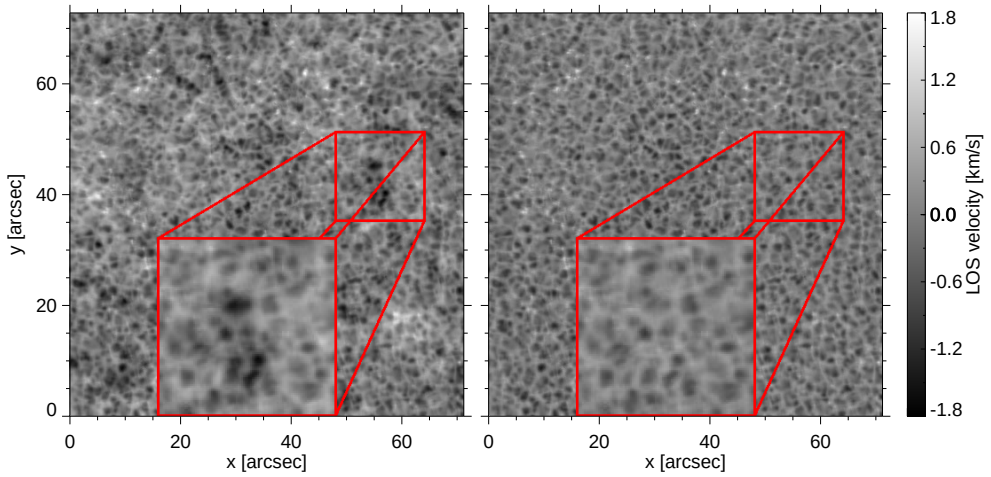

FIGURE 2.10:— We use a subsonic Fourier filter to remove the 5-min photospheric oscillations from the images (left panel). The result is presented on the right panel. In the magnified area one can see how the filtering changes the line-of-sight velocities. Overall, the filtered image looks much smoother.

X- and Y-axes. An example is shown in Figure 2.9. The area common to all images is intersection between blue and red boxes that represent the maximum of the shifts of the images in the sequence. The blue and red numbers are these shifts in pixels. As a result, the common FOV is reduced.

2.5.6 Removal of 5-min oscillations

Photospheric observations are affected by 5-min oscillations which we remove by applying a subsonic filter (Title 2000; Straus et al. 1992). The images are first transformed into the Fourier domain where the number of frequencies is equal to the number of pixels in the spatial domain. The transformed images are then multiplied by a Butterworth-type filter. Such filters are designed to have the frequency response as flat as possible in the passband and to drop to zero in the stopband. They are specified by the two parameters: cuttoff frequency and filter order. The sharpness of the transition from the passband to the stopband is determined by the filter order. Using the Butterworth filter, we suppress all the frequencies corresponding to a phase velocity of $v_p = 4$ km/s or higher.

The effect of removing the 5-min oscillations can be seen in Figure 2.10. In the left panel we present a Dopplergram where the oscillations are not

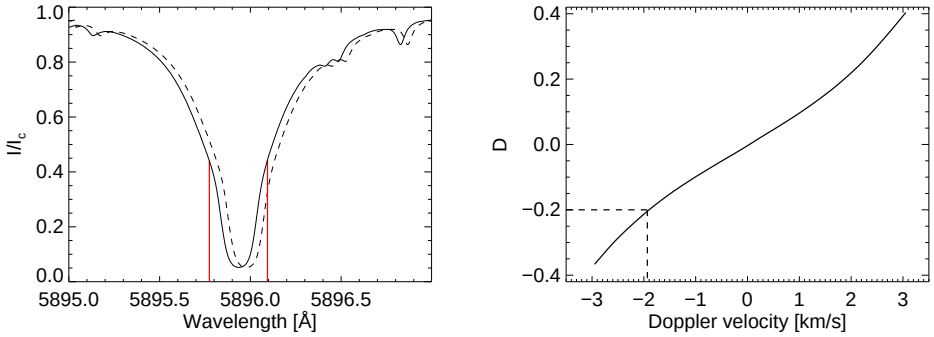

FIGURE 2.11:— To calibrate the Dopplergrams, we shift the spectral line (left panel, solid line) in the range between -2 and 2 km/s (dashed line) and calculate the ratio D between intensities at ±160 mÅ (red vertical lines), and their sum. The ratio as a function of Doppler velocity is plotted on right panel (black line), and calibration constant is derived as a linear fit to it (red line).

removed and in the right panel the same Dopplergram with the oscillations removed. The filtered Dopplergram looks smoother and in the magnified region it can be seen that some velocities are significantly changed. Strong bright and dark diffuse areas in the left panel are attenuated by the filter. More compact features like bright points in intergranular lanes are preserved.

Since the 5-min oscillations are also present in the magnetograms and intensity maps, they are filtered as well.

2.5.7 Calibration of magnetograms and Dopplergrams

The final step in the reduction of the NFI observations is the calibration of the Dopplergrams and magnetograms. We use the Na I D1 line profile from the Kitt Peak FTS-Spectral-Atlas to calibrate the Dopplergram signals. First, we calculate the ratio of differences between the line intensities at two wavelengths and their sum, as a function of the Doppler velocity (Figure 2.11). Shifting the spectral line for velocities in the range from -3 to 3 km s^{-1} (dashed lines in left panel), we determine the ratio, D, at ±160 mÅ. Since the dependence does not follow a perfect linear trend we do not use the slope of the curve as a calibration constant but the curve itself. For example, if we measure $D = -0.2$ in a given pixel, this corresponds to a LOS velocity of -1.93 km s^{-1} to the blue.

The calibration constant transforming the magnetogram signal into

flux density is obtained using the weak-field approximation (Landi Degl'Innocenti & Landolfi 2004). The ratio between V and I is given by:

$$\frac{V(\lambda)}{I(\lambda)} = -\phi_{\rm long} C \frac{{\rm d} \ln I(\lambda)}{{\rm d}\lambda},$$

where $C = 4.67 \cdot 10^{-13} g_{\rm eff} \lambda_0^2$, with λ_0 being the central wavelength (in Å) and $\phi_{\rm long} = f \cos\gamma B$ is the flux density. We determine the value of $\frac{{\rm d} \ln I(\lambda)}{{\rm d}\lambda}$ at $\lambda = \pm 160$ mÅ from the atlas profile . Using the atomic parameters of the line and this value, we obtain a proportionality between M from equation 2.1, and ϕ of the form:

$$\phi_{\rm long} = 9160 \text{ M } [\text{Mx cm}^{-2}],$$

which allows us to derive the flux density from the observed magnetogram signal easily.

To determine the noise of the magnetograms, we compute the standard deviation in a region without clear solar signals. The noise is found to be equal to $\sigma = 6$ G at this stage. To reduce the noise even further, we spatially smoothed the magnetograms using a 3×3 kernel of the form

$$k = \frac{1}{16} \begin{pmatrix} 1 & 2 & 1 \\ 2 & 4 & 2 \\ 1 & 2 & 1 \end{pmatrix}. \tag{2.3}$$

This corresponds to a truncated Gaussian distribution with a full width at half maximum (FWHM) of 2 pixels, which is smaller than the size of the magnetic features studied in this thesis. The result is a minimal degradation of the spatial resolution but a significant improvement of the noise down to $\sigma = 4$ Mx cm^{-2}. Such a low noise level makes these data the most sensitive magnetic field measurements ever taken in the internetwork using a filter instrument. They permit a more reliable identification of the weakest IN magnetic features and their association between consecutive magnetograms. Examples of final magnetograms, Dopplergrams and intensity maps are shown in Figures 2.12 and Figure 2.13. These maps were taken during the first run of HOP 151.

2.6 Summary

In this chapter we have described the Hinode satellite and its instruments. We presented in detail the Narrowband Filter Imager and explained how

filtergrams were recorded in the framework of the Hinode Operation Plan 151. We show the data reduction process step by step, providing explanations and examples of how calibrated Dopplergrams and magnetograms are obtained.

HOP 151 gives us the opportunity to study the quiet Sun magnetism at the highest sensitivity ever achieved with a filter instrument. It provides five data sequences with:

1. Stokes I and V filtergrams in Na I 5896 $\pm$ 160 mÅ;
2. monitoring of the quiet Sun at the disk center;
3. long duration of up to 40 hours;
4. high cadence (60 sec);
5. high resolution ($0\farcs16$);
6. noise level of only 4 Mx cm^{-2} pixel $^{-1}$.

This means that the HOP 151 observations show the evolution of network and internetwork magnetic patches on scales from minutes to days at unprecedented spatial and temporal resolution. In this way, we can analyze for the first time how these fields appear, evolve and are removed from the photosphere. Apart from the photospheric measurements, the HOP 151 data sets also contain chromospheric and coronal observations. This gives the possibility to study how internetwork fields contribute to the high layers of the solar atmosphere.

In this thesis, we will use the HOP 151 data sets to examine how quiet Sun magnetic flux is maintained on the solar surface. These high sensitivity, high resolution measurements will facilitate the identification of magnetic patches in magnetograms, permitting us to detect even the weakest internetwork fields. We will derive the most reliable appearance and disappearance rates of internetwork magnetic patches. In addition to this, we will study their modes of appearance and estimate their contribution to network regions and the solar magnetism in general.

To achieve these goals, the first task is to follow the evolution of individual magnetic patches in the NFI magnetograms. To this purpose, we use an automatic tracking algorithm, which is described in the following chapter.

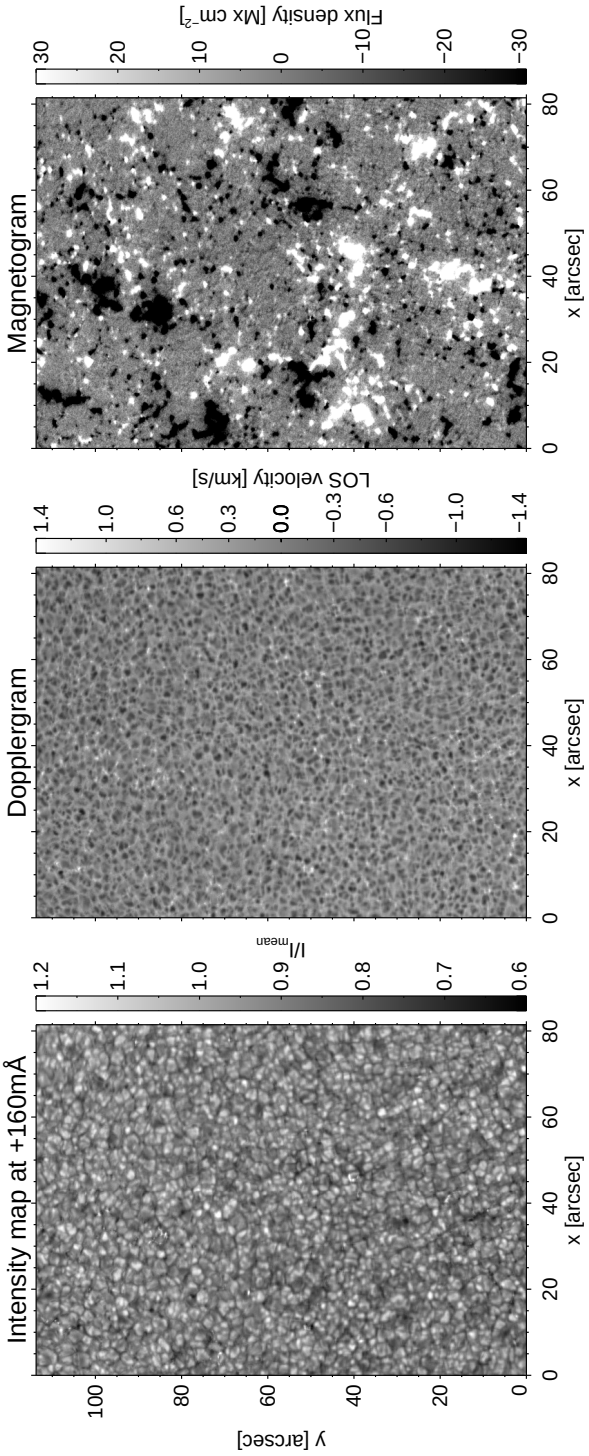

FIGURE 2.12:— Examples of intensity map at +160 mÅ, Dopplergram, and magnetogram from data set 1 after the data reduction process.

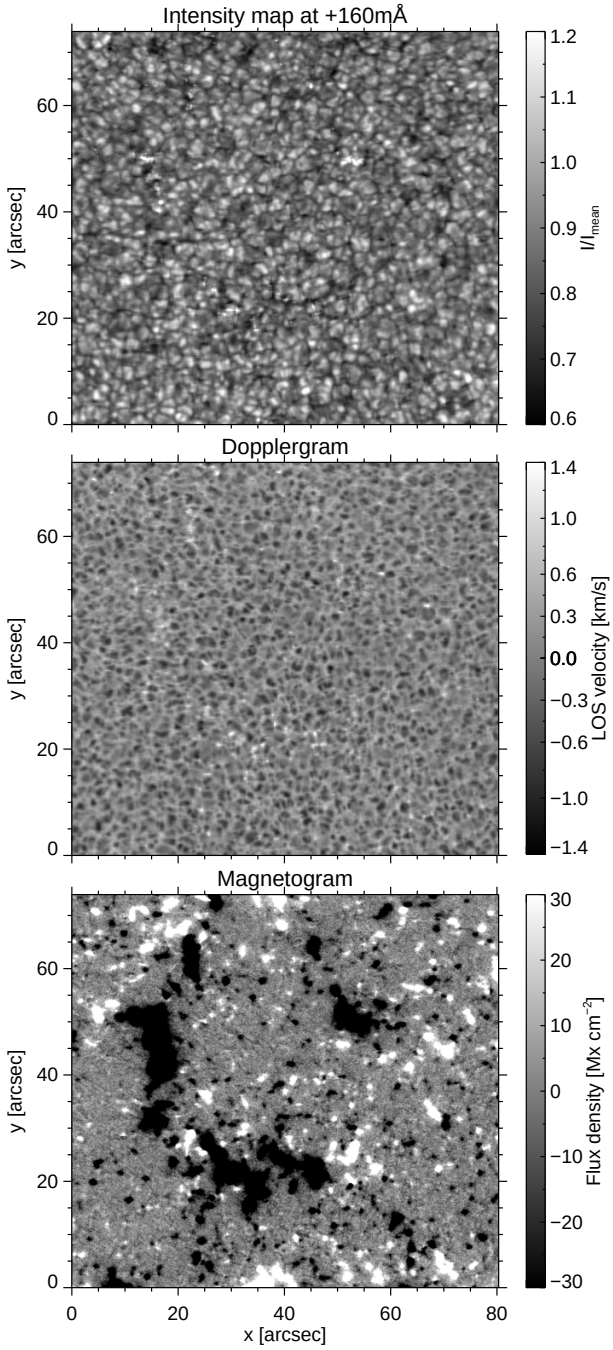

FIGURE 2.13:— Same as Figure 2.12 but for data set 4.

3

Tracking of magnetic features

3.1 Introduction

During the last years, significant efforts have gone into the investigation of quiet Sun magnetic fields thanks to improved observational capabilities. However, we are still far from understanding their origin and how they affect the solar atmosphere. Availability of space observations, such as those from the Hinode satellite, gives us the opportunity to extend our knowledge about the quiet Sun magnetism.

The quiet regions of the solar surface are densely populated with small, weak flux patches. To understand their properties, origin, and contribution to the solar magnetism, we have to study their spatial distribution and temporal evolution. For that purpose, automatic tracking codes are essential. They allow us to determine the physical parameters of solar magnetic patches so that they can be analyzed and combined with other observations and numerical simulations. However, tracking codes are not perfect and their limitations often compromise the goal of studying the quiet Sun magnetism because of the errors they make when elements are identified and/or tracked. These problems need to be corrected for automatic codes to deliver reliable results.

To accomplish this, we have developed a new IDL code which solves the most common problems of tracking algorithms, known for more than a decade. Our code allow us to determine for the first time the history of flux patches in a consistent way, and therefore, the evolution of the flux

in the quiet photosphere.

In this thesis, we will use the YAFTA code to identify and track magnetic elements. In Section 3.2 we describe magnetic feature tracking codes and YAFTA in particular. We explain in Section 3.3 how we solve YAFTA's problems and demonstrate the capabilities of our code.

3.2 Principles of feature tracking codes

Feature tracking algorithms are widely used for statistical analyses of magnetic structures observed on the solar surface. Their main objectives are to identify magnetic elements in magnetogram sequences and to match the identified elements between consecutive frames. During the tracking process, they calculate the physical parameters of each magnetic patch. Recently, several automatic feature tracking algorithms have been developed in order to address scientific questions related to solar magnetic fields (Hagenaar et al. 1999; Parnell 2002; Lamb & DeForest 2003; Welsch & Longcope 2003; Hagenaar & Cheung 2009; Thornton & Parnell 2010; Attie & Innes 2015, see also DeForest et al. 2007). In general, all codes follow the same strategy to track magnetic elements, which can be divided in four steps:

- data preparation;
- detection of magnetic patches;
- identification of patches in subsequent frames;
- calculation of physical parameters and event description.

We will now describe each step and how they are implemented in the YAFTA code[1] (Yet Another Feature Tracking Algorithm; Welsch & Longcope 2003; DeForest et al. 2007), which is used in this thesis. Briefly, YAFTA is a package of IDL routines that accomplishes the above mentioned tasks. It is organized in a modular manner and is relatively easy to modify if necessary.

[1] YAFTA can be downloaded from the author's website at `http://solarmuri.ssl.berkeley.edu/~welsch/public/software/YAFTA`.

3.2.1 Data preparation

In principle, data preparation is not part of the tracking process but experience shows that the results can significantly be affected by the way the observations/magnetograms are reduced. Before applying the tracking code to a given data set, the images should be preprocessed. In this step the main goal is to reduce the noise level (if possible), and to remove any artifacts and/or features that can confuse the tracking algorithm.

Noise can strongly affect the identification of magnetic elements and interactions between them, as we will demonstrate in Section 3.3. Because of this, it plays an exceptionally important role in the tracking process and should be reduced as much as possible. By reducing the noise, one actually decreases the number of false detections of magnetic features, and improves their association across subsequent images. Moreover, a lower noise level leads to a fewer errors in the interpretation of interactions between elements.

In image processing, noise reduction is usually achieved using temporal and/or spatial averaging/smoothing. Averaging in time (combining a few images) means that the temporal resolution will worsen. Because of this it is important to make trade-offs between the degree of averaging and the dynamics of the observed processes. For example, in the case of small-scale internetwork patches it is a good idea to have a temporal resolution of about one minute to get accurate information on lifetime and interactions.

The most common way to spatially smooth an image is to use Gaussian kernels. Convolving an image with such functions (that act as a low-pass filter) results in the removal of the high-frequency components of the image. The FWHM of the Gaussian should be smaller than the size of the studied magnetic features to avoid a large degradation of the spatial resolution.

Depending on the scientific goals, cosmic rays may need to be filtered from space-borne observations because they can affect the lifetime, size, and strength of the tracked features, and even lead to misinterpretation of interactions. Some cosmic rays can be removed during the temporal averaging, while others have to be removed using other techniques. In both cases, it is important to make sure that the real signals are not modified. Often, a simple lifetime threshold turns out to be sufficient to separate real features from cosmic rays.

3.2.2 Detection of magnetic patches

The first task of any tracking code including YAFTA is to distinguish the real magnetic patches from the background signal in a magnetogram image. This step is very important and directly affects the final results. In general, high-resolution magnetograms show a mixture of strong and weak features close to the noise level (left panel in Figure 3.1). The easiest approach to separate real signals from the background is to set a detection threshold.

The threshold level is the value below which the image signal is not considered. Normally, this value is determined by the noise level, σ, and is set to 2σ or higher. This criterion works very well in the case of strong magnetic patches, such as those in active regions and network. For the weak patches of the internetwork, too high thresholds imply that many weak signals will remain undetected. If the code fails to detect a given patch during part of its evolution, its lifetime will not be correctly estimated, nor its trajectory, or the appearance and disappearance modes. On the other hand, too low thresholds will cause numerous detections of false magnetic patches due to the noise. Thus, it is up to the user to decide which threshold works best for a given data set. An example of a quiet Sun magnetogram after a 3σ threshold is applied is shown in the right panel of Figure 3.1.

Occasionally, discrimination of real signals from the noise can be improved by using two thresholds: a lower and an upper one. When a lower threshold value is applied, all pixels with signals above this value are detected and selected. In the next step, adjacent detected pixels are grouped together. To be considered as a flux patch, such a group of pixels must contain at least one pixel with signal higher than the upper threshold. In some implementations, it is required that the upper threshold criterion is fulfilled at some moment of a feature's evolution (not in every frame).

In most cases, thresholding is not sufficient and additional criteria are introduced. These criteria, for example, can be size and lifetime of magnetic features. The lower limit that is used in practice for the size is 3 pixels. This makes it possible to remove many isolated single pixels that most likely are not real signals but noise. Depending on the dynamic nature of the observed processes, the minimum lifetime can be set to two frames, so that only magnetic patches visible in two or more frames are taken into account.

The YAFTA code was originally developed for active region investiga-

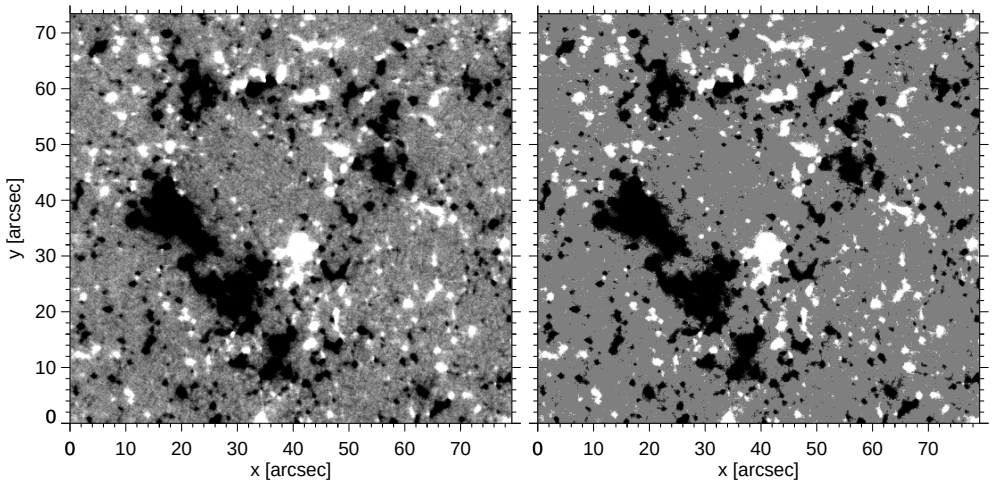

FIGURE 3.1:— *Left panel:* A real magnetogram from our data sets, taken on November 2, 2010 at the disk center and saturated at ± 30 Mx cm^{-2}. *Right panel:* The same magnetogram after a 3σ (12 Mx cm^{-2}) threshold is applied.

tions where flux patches have signals significantly above the noise level. For this reason a simple threshold criterion was sufficient. Later, an upper threshold was implemented. In addition to this, YAFTA uses the size criterion during the detection of flux features.

3.2.3 Identification of magnetic patches

In LOS magnetograms, a signal patch represents a flux concentration, located at a given position with a certain flux density and polarity. In practice, it is a 2D array of pixels that are grouped together. Feature identification is the process of connecting these pixels with a real structure in a given magnetogram.

After all pixels above a certain threshold are selected, the identification algorithm is applied to these pixels. As a result, individual features are identified and a label mask is created. Each feature in the mask has the same integer numeric value (label) in all its pixels. YAFTA uses two different methods to identify magnetic elements:

– The *clumping* method (Parnell 2002) - This method groups all contiguous pixels above the threshold that have the same sign into one patch. The identified magnetic patches may have more than one local maximum.

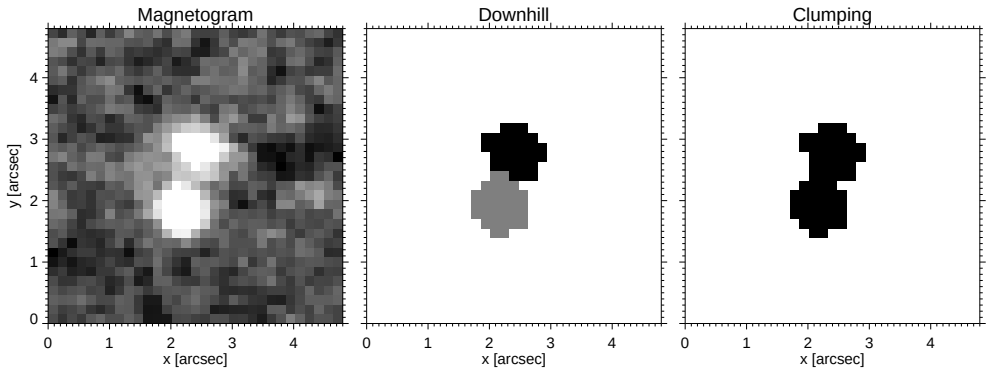

FIGURE 3.2:— *Left panel*: Real magnetogram. Two feature identification methods are applied to it. *Middle panel*: The downhill method finds two local maxima that are recognized as different magnetic patches, shown in gray and black. *Right panel*: The clumping method merges together all contiguous pixels, forming one magnetic patch with two maxima. The detection limit is set to 3σ in both cases.

– The *downhill* method (Welsch & Longcope 2003) - In this case, all pixels above the threshold that lie on the same hill and have the same sign are grouped together. Pixels with signals below the threshold are not taken into account. Pixels located on saddle points are associated with the pixels found in the direction of the steepest uphill gradient.

To separate individual elements inside flux clusters, the downhill method is the best option. However, signal fluctuations can create local maxima which trigger false identifications of flux patches. The clumping method is less sensitive to such fluctuations. Choosing one or another depends on the scientific problem to be investigated.

An example of how the identification of flux patches works in practice is shown in Figure 3.2. Here, the downhill and clumping methods are applied to a real magnetogram using a 3σ detection limit. A magnetic feature is shown in the left panel. The results of the two methods are presented in the form of mask images. The downhill method detects two flux maxima and classifies each of them as a distinct magnetic feature (middle panel). By contrast, the clumping method associates all neighboring pixels into one feature (right panel).

YAFTA groups the pixels together using the downhill or clumping method with the `rankdown.pro` and `contiguous_mask.pro` procedures, respectively. If desired, both methods can be used in the same run. Thus,

the resulting identifications can be compared directly.

3.2.4 Magnetic patch association between images

The association of magnetic patches is the process whereby the detected magnetic elements are identified in a sequence of images. YAFTA uses the criterion of maximum area overlap between two consecutive frames.

In the simplest case (one-to-one match), an element from the previous frame overlaps with only one element in the current frame. The two elements are then taken to be the same feature. However, it may happen that the element overlaps with several same-sign elements from the current frame, that also exist in the previous frame. In that case, YAFTA associates this element with the one in the current frame with whom it shows maximum overlap.

The situation is more complicated when an element (parent) splits into many smaller patches (children). If the newly formed fragments overlap only with their parent in the previous frame, they are considered to be new patches and will receive unique labels. Furthermore, YAFTA also checks how much flux each child contains. The largest child in terms of total absolute flux will keep the label of the parent element.

The same overlap strategy is used when many small elements (parents) merge into one larger element (child). The only difference now is that the child gets the label of the parent with the largest flux content.

Magnetic elements that cannot be associated with flux features in the previous frame are considered as newly appeared elements. Those from the previous frame that do not overlap with any element in the current frame are interpreted as in-situ disappearances.

An illustration of the association process is shown in Figure 3.3. Magnetic elements A and B are seen in the previous frame (upper left panel), and C and D in the current frame (upper right panel). Element C intersects elements A and B but the maximum overlap is with element B, as shown in the bottom left panel. Element B also has the maximum intersection with element C, although it overlaps with D as well. The maximum-overlap method recognizes B and C as the same element evolving with time. Thus, YAFTA will rename C to B before moving forward in time. Element D is identified as a fragment of B and element A is detected as an element that disappeared by merging with C. The result of the identification is shown in the bottom right panel.

For each element in each frame, YAFTA keeps information about their

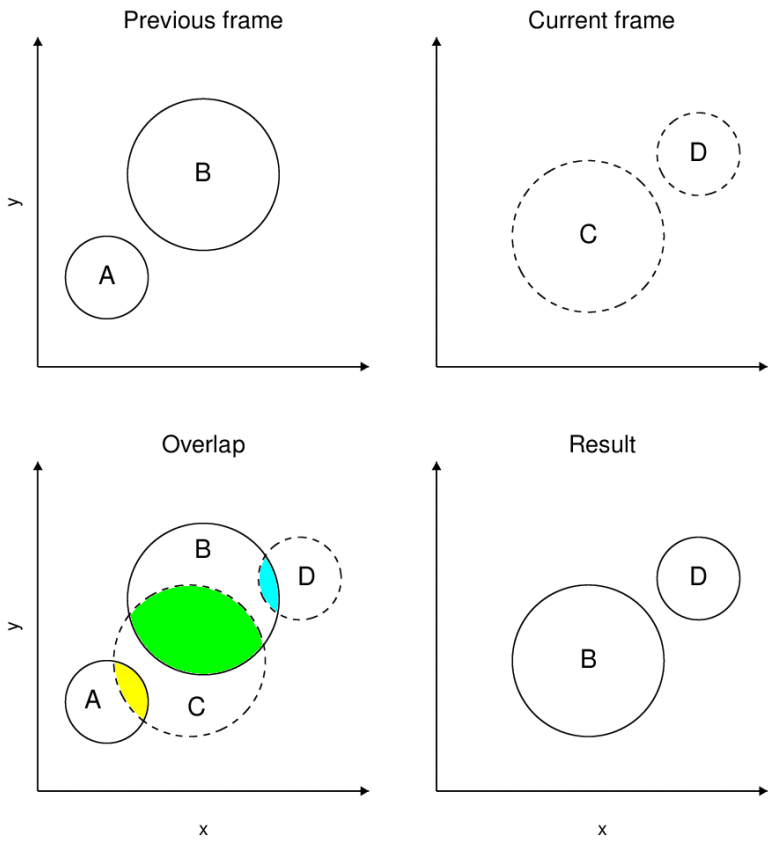

FIGURE 3.3:— Association of magnetic patches. According to YAFTA, elements A and B from the previous frame merge together to form element C and Element D appears by fragmentation of B. The maximum overlap method recognizes B and C as the same element that moved from one frame to the next.

interactions (fragmentations and mergings) and how they appear and disappear. This information is stored in an IDL structure called "features", which has several fields. For example, when an element appears in situ, its first "source" (.src) field is equal to the negative of the frame number in which it becomes visible for the first time. If it appears by fragmentation, the source value is positive and equal to the label of the parent element. On the other hand, if a flux patch disappears in situ, its "termination" (.trm) value is the negative of the frame number in which the patch disappears. When an element disappears by merging, the termination field contain the label of the child element. In all other cases, the termination

and source fields are positive and equal to the label field, which keeps the label of the tracked element.

3.2.5 Physical parameters of magnetic patches

In this Section we list the physical parameters that are computed for each magnetic feature tracked by the YAFTA code and explain how they are defined.

- Magnetic parameters:
  - Magnetic polarity of the patch. It is determined by the sign of the magnetogram signal in a group of connected pixels.
  - Total unsigned magnetic flux: $\Phi = (\sum_{j=1}^{N} |\phi_j|)\mathrm{d}A$. The summation is done over the N pixels of the patch, ϕ_j is the magnetic flux density of pixel j, and $\mathrm{d}A$ is the pixel area.
  - Maximum unsigned magnetic flux density of the patch in each frame, $\max(|\phi_j|)$.
- Geometric parameters:
  - Flux-weighted x and y positions of the patch: $\overline{x} = (\sum_{j=1}^{N} x_j \phi_j)\mathrm{d}A/\Phi$, where x_j is the x coordinate of pixels of the magnetic patch, and similarly for y.
  - x and y coordinates of all the pixels belonging to the element.
  - Size of the patch, computed as the total number of pixels it contains.
- Other parameters:
  - Modes of appearance and disappearance. Magnetic elements may appear in situ or by fragmentation. Flux patches disappear in situ or by merging with a stronger patch.
  - Interactions can be determined by analyzing the termination and source fields.

In Figure 3.4 we show one magnetic element that is tracked from the moment of appearance until it disappears. The evolution of the maximum flux density and total magnetic flux during its lifetime are presented in the upper row (left and right panels, respectively). In the lower left panel

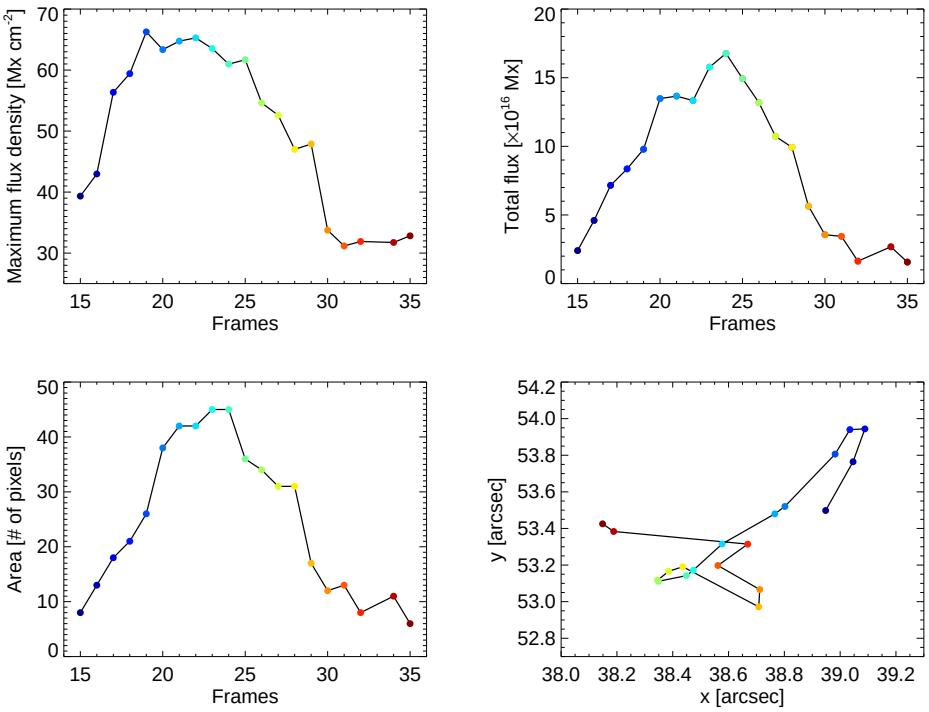

FIGURE 3.4:— Time evolution of the physical parameters calculated for one tracked element. *Upper row*: Maximum magnetic flux density (left) and total magnetic flux (right). *Bottom row*: Size (left) and trajectory (right) of the tracked element.

we can see how its size changes with time. The position of the patch is shown in the lower right panel, revealing its trajectory. The tracked patch grows in flux and size until frame 24. After the parameters reach a maximum, the patch starts to shrink and completely disappears in frame 35. The lifetime of this particular element is 30 minutes, which is longer than the mean lifetime of internetwork elements (seven minutes).

All computed parameters of the tracked element are stored in the IDL structure "features". A new structure is created for each patch at each time step and merged with previously created structures. At the end of the tracking process, the magnetogram sequence, the label mask of each frame, and the "features" structure are stored in an IDL save file. Descriptions of each field of the "features" structure and examples of their use can be found in the YAFTA manual.

3.3 Code for corrections of YAFTA results

The YAFTA code is an important part of our efforts to understand the evolution of quiet Sun magnetic fields. However, the cornerstone is the code we have developed to solve YAFTA's problems. Only with this code we can determine the history of individual flux patches. In this section, we will present how our code resolve the errors made by YAFTA.

Before we describe the problems and give solutions, we will introduce terms that explain the processes necessary to understand the evolution of flux features. High resolution NFI observations show that magnetic elements are in constant motion and often interact with each other. To describe their evolution, we need to follow them from their appearance to disappearance and classify all interaction they may undergo during their lifetimes. In this regard, there are five types of processes (also called *surface processes*), that need to be considered:

- *In-situ appearance*, the process by which new flux elements become visible in the magnetograms for the first time.
- *Merging*, or the coalescence of two or more elements of the same polarity into a larger structure. In this process, only the largest element survives. The smaller elements are considered disappeared features and the flux they contain is incorporated into the surviving element.
- *Fragmentation*, is the opposite of merging. It occurs when an element splits into two or more smaller features (children).
- *Cancellation*, or the mutual disappearance of opposite polarity magnetic elements when they come into close contact.
- *In-situ disappearance*, a fading whereby magnetic elements disappear from the solar surface without an obvious interaction with any other feature.

As mentioned before, YAFTA assigns a unique label to each newly detected feature, which allows us to trace back its history and origin. Magnetic elements change their labels when they merge with a stronger flux patch, cancel completely with an opposite-polarity element, or disappear in situ. Likewise, the fragments of a feature get new labels except the stronger one, which maintains the label of the parent.

Unfortunately, YAFTA, as any other automatic feature tracking code, frequently misinterpret surface processes. Thus, the same magnetic feature may erroneously change its label many times during its lifetime, which makes it difficult to determine its history correctly. This normally happens because of noise but also because of flaws of the tracking algorithm. As a consequence, three types of errors occur:

- wrong detections of appearance and disappearance events;
- magnetic patches exhibit nonphysical evolution (abrupt changes of their physical parameters);
- incorrect number of interactions between flux patches.

To derive reliable results we have to correct these errors. Therefore, we need to identify and solve the following problems:

- false detection of in-situ disappearances followed by appearances of magnetic elements, which leads to the first error;
- misidentifications of elements due to merging and fragmentation processes, which can cause any of the errors specified above.

In the following sections, we will describe in detail the aforementioned types of errors, show examples, and present our strategy to correct them.

3.3.1 False detection of in-situ disappearances followed by appearances

The *Hinode* NFI magnetograms contain large numbers of small, weak flux features close to the noise level. The easiest approach to separate them from the background is to set a detection threshold. However, weak patches may fall below the threshold level and surpass it again multiple times during their lifetimes due to intrinsic flux fluctuations. Whenever this occurs, YAFTA detects a disappearance followed by an in-situ appearance, although it is the same flux structure. This artificially increases the appearance and disappearance rates. Setting the threshold level to 3σ and the minimum size of flux features to 4 pixels yields about 7% of false disappearance and appearance events in our data sets. This is equivalent to an increase of 8% in the total initial flux of the elements that appear in-situ, which is not real.

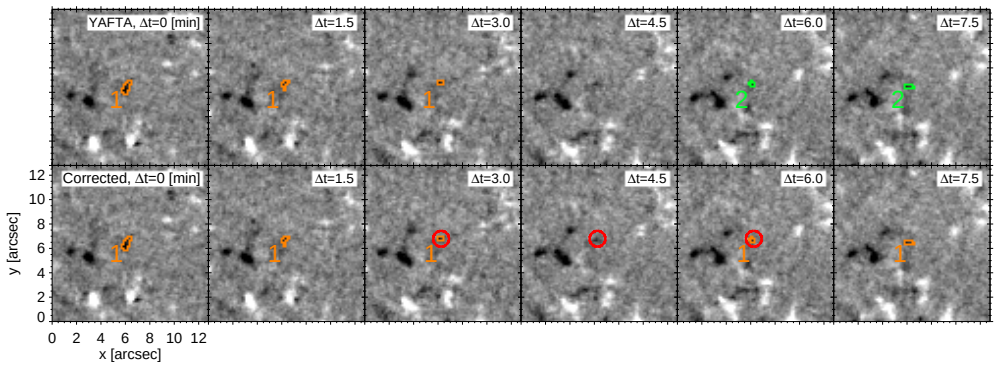

FIGURE 3.5:— False detection of disappearance and appearance events. *Upper row*: Due to signal fluctuations, YAFTA fails to detect a previously existing flux patch (orange contour, label 1) at $\Delta t = 4.5$ minutes. At $\Delta t = 6$ minutes, another flux patch is detected at more or less the same location and identified as a new flux feature appearing in situ (green contours, label 2). *Bottom row*: Our method corrects the YAFTA results recognizing that the element appearing at $\Delta t = 6$ minutes is the same patch that was visible from 0 to 3 minutes. The red circles visible from 3 until 6 minutes have a radius of 4 pixels and represent the area in which we expect the appearance of a new element.

Figure 3.5 shows an example of how temporal changes in the flux content of an element are misinterpreted by YAFTA as the disappearance of the element followed by the appearance of a new element, and how we correct for this error. In the upper row we can see the evolution of a small magnetic patch (orange contour, label 1), which according to YAFTA disappears in situ at $\Delta t = 4.5$ minutes. However, in this frame, the flux concentration is still visible in the magnetogram image with a weaker signal. It is not detected by YAFTA as a magnetic element because it does not satisfy the selection criteria of at least 4 contiguous pixels with signals above 3σ. In the next frame, $\Delta t = 6$ minutes, YAFTA detects the appearance of a new magnetic element at the same location (green contour, label 2). This new element is actually the old element, now with a stronger signal than it had before the disappearance.

To correct for this, we look for elements disappearing in-situ and check if a new magnetic element of the same polarity appears nearby in any of the next three frames. The region we examine is a circle having its center at the position of the flux-weighted center of the disappeared element (bottom row, $\Delta t = 3$ minutes, red circle). We first search for the appearance of a new element in the frame $\Delta t = 6$ minutes using a circle of radius 2 pixels. If there are no new elements, the radius is increased to 4

pixels and we look if patch appears in the following two frames. If so, we consider it to be the same element as the previously disappeared one if their fluxes and sizes agree to within a factor of 3. An additional requirement is that at least 30% of the area of the newly appeared element is inside the circle. These criteria are satisfied in the example of Figure 3.5, and therefore the new element detected at $\Delta t = 6$ minutes is given the same label and contour color as the magnetic element that disappeared at $\Delta t = 4.5$ minutes.

While correcting for false disappearances and appearances, we also check magnetic elements that last only one frame. These elements are consider to be part of a longer-lived appearing (or disappearing) patch if they overlap more than 70%.

3.3.2 Errors caused by merging and fragmentation processes

During their lifetime, magnetic elements may undergo fragmentations and mergings with other flux patches. When these two processes occur one after another, they may go undetected if they take place in the same frame and/or lead to erroneous changes of the labels of the magnetic elements. As a result, we either get wrong information about the origin and evolution of the flux patches or we lose track of the elements. Because of this, it is important to interpret mergings and fragmentations with great care.

We recognize three situations in which mergings and fragmentations produce false identifications of flux patches:

- a merging promptly followed by a fragmentation;
- flux exchange between patches because fragmentation and merging occur in the same frame;
- fragmentation is followed by merging.

We will now describe these scenarios, their consequences and demonstrate our strategy to correct them.

Merging followed by fragmentation

A common problem is the connection of a small magnetic element with a stronger patch only in one frame. When there are a few pixels between two magnetic elements, noise may raise the signal above the threshold level in those pixels and temporally connect the two structures. Since the

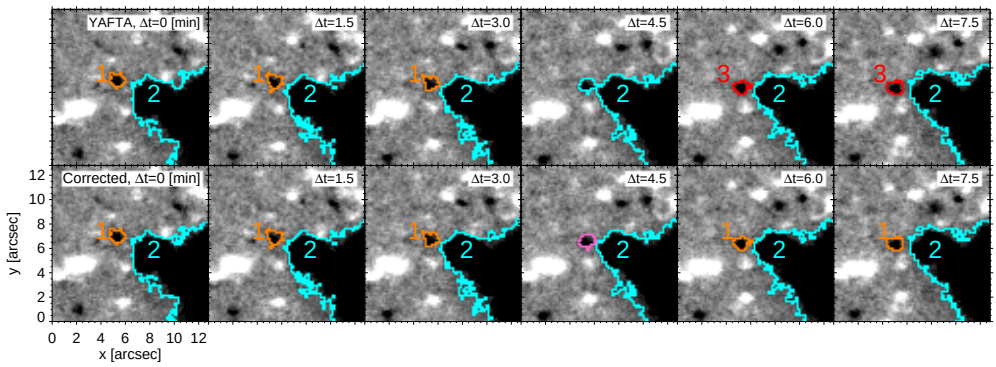

FIGURE 3.6:— Example of a magnetic element merging with and fragmenting from a stronger element. *Upper row*: the smaller element (orange contours, label 1) and the stronger element (blue contours, label 2) are shown as they are detected by YAFTA. Element 1 merges with the element 2 at $\Delta t = 4.5$ minutes and fragments at $\Delta t = 6$ minutes. From this moment on, the smaller patch is recognized by YAFTA as new magnetic element (red contours, label 3). *Bottom row*: interpretation of the same process by our method. Although, the smaller patch (label 1) merges with and fragments from the stronger patch (label 2), it is properly identified as the same element in all frames. The violet contour at $\Delta t = 4.5$ minutes encompasses the pixels associated with the element 1.

two elements do not really interact, the rate of mergings and fragmentations are artificially increased. Moreover, from that moment on, YAFTA considers the small patch as an element that disappears by merging with a stronger patch. When it gets detached from the stronger patch, it is identified as a new element. This makes it impossible to follow the complete history of the weaker element. Usually this problem happens at the borders of supergranular cells and around clusters of elements, where numerous small patches are located close to stronger features. In an NFI magnetogram sequence with dimensions 500×500 pixels, one can expect about 5 misidentified elements per frame due to this problem.

Figure 3.6 shows an example. The YAFTA interpretation is displayed in the upper row. A small flux patch (orange contour, label 1) merges with a stronger patch (blue contour, label 2) at $\Delta t = 4.5$ minutes. The smaller patch is connected to the larger one only in this frame and loses its label. It is detected to fragment from the larger patch at $\Delta t = 6$ minutes. In that frame YAFTA identifies the smaller patch as a new magnetic element resulting from fragmentation of the larger patch. This element is assigned the new label 3.

Our correction of this process is shown in the bottom row in Figure

3.6. To properly identify element 1 as the same flux feature in all frames we use a criterion based on area area overlap. In this particular example, we compare the logical mask of magnetic element 1 at $\Delta t = 3$ with the mask of all elements in the next frames where it is no longer present, according to YAFTA. The overlapping pixels, located inside the region enclosed by the violet contour, are assumed to belong to the disappeared element 1. At $\Delta t = 6$, they overlap by more than 50% with element 3, and also contain its flux-weighted center. Because of this, we re-label element 3 into 1 and identify it as the continuation of element 1. Finally, we update the YAFTA's output parameters and masks so they reflect these changes. We do not correct disappearing elements if there is no overlap in the following three frames.

Exchange of flux between magnetic elements

Magnetic elements of the same polarity may exchange flux if they are located close to each other. This occurs when a flux patch fragments from an element and merges with the other element in the same frame. Since both fragmentation and merging occur in the same frame, YAFTA does not detect these processes and interpret the changes as the intrinsic evolution of the elements. As a result, we miss some interactions between magnetic patches. Also, if the flux exchanged between the two elements is large enough, we may get wrong information about the origin of one of the patches. In addition to this, their physical parameters would change by a few factors. This frequently occurs in highly populated regions such as network and may have important consequences for analyses in which the origin of the patches needs to be known with accuracy.

We give an example in Figure 3.7. In the upper row we see the temporal evolution of magnetic element 1 (blue contour) and element 2 (yellow contour). At $\Delta t = 4.5$ minutes, element 1 splits and the smaller fragment merges with element 2 in the same frame. According to YAFTA, however, elements 1 and 2 go through an abrupt change of flux and size, which is interpreted as the evolution of the elements.

The solution to this problem is shown in the bottom row. The idea is to find all elements whose size and/or flux changes by more than a factor of 2 between two consecutive frames. This is what happens to element 2 at $\Delta t = 4.5$ minutes. In the next step we check whether YAFTA has found elements that interact with element 2 in this frame, and whether those interactions can explain the evolution of element 2. If no merging event

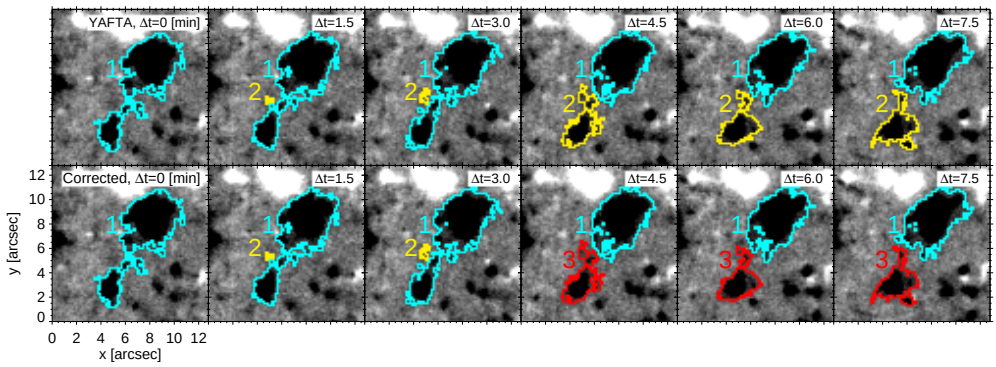

FIGURE 3.7:— Flux exchange between two magnetic elements. *Upper row*: the small flux patch (yellow contour, label 2) is located close to the larger patch (blue contours, label 1). At $\Delta t = 4.5$ minutes, the larger patch fragments, and its fragment merges in the same frame with the element 2. According to YAFTA, the elements 1 and 2 in this frame drastically change in flux and size, while their interactions are not detected. *Bottom row*: when the element 1 fragments at $\Delta t = 4.5$ minutes, it adds flux to the element 2. The interaction is recognized by our method and the element 2 is detected as an element that disappears by merging process. The newly formed fragment (red contour, label 3) is detected as a new patch.

involving flux patch 2 is detected in this frame, then it means that the flux change of this element most likely occurred due to flux exchange with some other element in its vicinity. Next, using the same overlapping criterion as in the previous case, we determine if element 2 at $\Delta t = 4.5$ overlaps with any element in the previous frame. If so, the label of element 2 at $\Delta t = 4.5$ minutes is changed to 3 (red contour). Element 3 is considered as a new element from this moment, originating from fragmentation of element 1. At the same time, element 2 is marked as a patch that disappears by merging with element 3. The history records of elements 1 and 2 in YAFTA's output are updated and element 3 is added to the list of detected elements. We make about 4 such corrections per frame in our data sets.

We also correct for a similar cases in which a magnetic element (A) merges with a stronger element (B) and at the same time, splits and creates a small fragment (C). We again have the problem that merging and fragmentation occur in the same frame and because of that, these processes are not detected by YAFTA. In this case, YAFTA erroneously recognize fragment C as element A. However, a proper identification of elements would imply that element A disappears by merging with element B, while element C is a new element formed by fragmentation of element A.

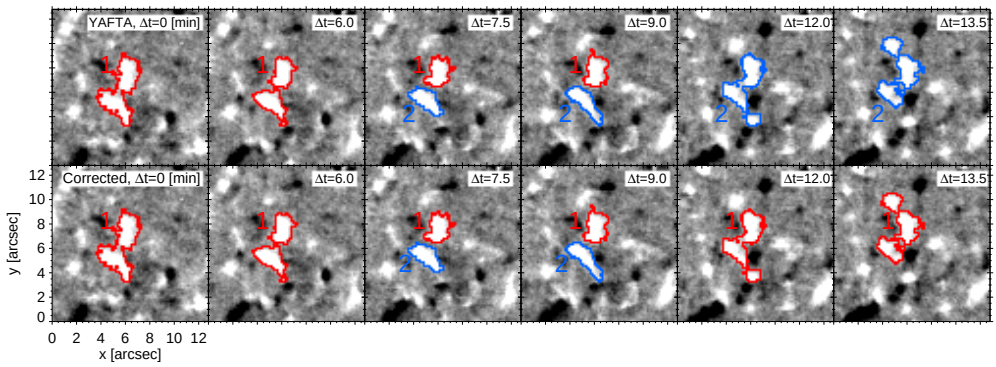

FIGURE 3.8:— Interaction of parent and child elements. *Upper row*: At $\Delta t = 7.5$ minutes magnetic element 2 (blue contour) fragments from element 1 (parent element). Element 2 is visible as an individual element in the following two frames and at $\Delta t = 12$ minutes, merges with its parent. Since in this frame element 2 has more flux than element 1, element 1 loses its identity. From this moment on, the entire flux structure is recognized as element 2. *Bottom row*: Our method considers a child element (blue contour, label 2) as a lower-level hierarchy element in each frame in which it exists. Thus, when a child element merges with its parent ($\Delta t = 12$), it loses its label, regardless of its flux content.

Fragmentation followed by merging

Finally, we consider fragments that have short lifetimes and disappear by merging with their parents. Any fragment may undergo such a process. By forbidding them to change the labels of their parents we preserve the information about the origin and correct history of the parent elements.

Figure 3.8 (upper row), displays an example of the interaction between a parent and a child element as seen by YAFTA. Element 1 (red contour) splits at $\Delta t = 7.5$ minutes and the child element (blue contour, label 2) is formed. Element 2 gains flux with time and merges with its parent at $\Delta t = 12$ minutes. It survives the interaction while the parent element loses its identity since it has less flux than the child. In the following frames, we can follow the evolution of the child element. Taking into account a hierarchy between magnetic elements, our method (bottom row) takes the child element as the one that disappears by merging with its parent, although it is stronger in flux. Now the parent element survives the interaction and is visible in the subsequent frames. In this way we keep information about the evolution of element 1 and its origin. In our data sets, we have to apply this correction about once per frame.

Interactions between parent and child elements may also unnecessar-

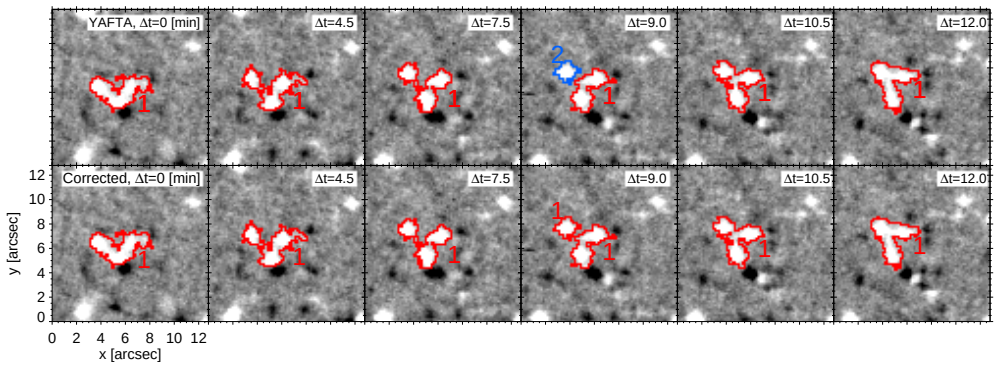

FIGURE 3.9:— Enhanced interpretation of fragmentation process. *Upper row*: Magnetic element 1 (red contour) fragments at $\Delta t = 9$ minutes. Its fragment, labeled as magnetic element 2 (blue contour), is detected as a unique flux feature in one frame only. At $\Delta t = 10.5$ minutes the element 2 merged with the element 1. *Bottom row*: With our method the element 2 from the upper row is recognized as part of the element 1. Hence, at $\Delta t = 9$ minutes, it carries the same label and the red contour as the element 1.

ily increase the number of interactions. For example, Figure 3.9 (upper panel), shows the temporal evolution of a strong magnetic element (red contour, label 1) that fragments at $\Delta t = 9$ minutes. One of its fragments (blue contour, label 2) lives as an individual patch in one frame only (at $\Delta t = 9$). At $\Delta t = 10.5$ minutes, this element merges with its parent (label 1). When fragments are separated from their parents in three or less frames, we do not consider them as individual elements. Instead, as shown in Figure 3.9 (bottom panel), such elements are assumed to be parts of the parent, and hence carry the same label (and the red contour in this case). Such a scenario is very often in the NFI magnetograms and we detect about 20 of them per frame in our data.

3.4 Summary

In this chapter we have described the principles of automatic feature tracking algorithms, and how magnetic patches are detected, identified and tracked in time and space. We have explained how these steps are implemented in the YAFTA code used in this thesis. We employ YAFTA to follow the evolution of magnetic elements in the NFI magnetograms from appearance to disappearance. For all detected patches, YAFTA calculates

a set of parameters that we use to study the quiet Sun magnetism.

During the tracking process, YAFTA often misidentifies magnetic elements and their interactions due to the noise of the magnetograms. When this happens, the origin and the evolution of the elements are not determined correctly. Because of this, it is difficult (sometimes impossible) to follow the evolution of individual patches, and therefore the quiet Sun fields cannot be accurately investigated. We have developed an IDL code to correct for this problem. The code allow us to determine correctly:

1. appearance and disappearance modes of flux patches;
2. temporal and spatial evolution;
3. variations of their physical parameters;
4. number and type of interactions between elements.

Our corrections of the YAFTA results are essential for proper estimation of the quiet Sun flux budget. Thanks to them, we can reliably follow the history of individual flux features, which has not been feasible with tracking codes developed until now. With this, we can accurately calculate the flux in network and internetwork over the entire Sun, and study their temporal and spatial evolution. Moreover, we will shed new light on how the quiet Sun flux is maintained on the solar surface.

4

Flux budget of the quiet Sun

4.1 Introduction

At any one time, most of the solar surface is devoid of sunspots and active regions. This "quiet" Sun (QS) occupies more than 85% of the total solar surface (Harvey & Zwaan 1993). In polarized light, the QS shows a reticular pattern of strong kG fields called the photospheric network (NE), and tiny magnetic elements in the regions in between, the so-called internetwork (IN). The NE outlines the boundaries of supergranular cells, while the IN closely corresponds to the interior of supergranular cells. Being ubiquitous, NE and IN magnetic fields may be crucial for the total flux budget of the solar atmosphere and therefore also for its energy budget. Because of this, it is important to know the flux present in the QS and how it varies spatially and temporally.

According to Schrijver & Harvey (1994), the total flux of active regions at solar maximum is $\sim 8 \times 10^{23}$ Mx over the entire Sun. However, it is much more difficult to determine the contribution of the NE and IN to the flux budget of the solar surface. The reason is that measurements in the QS require high spatial resolution, sensitivity, cadence, and long temporal coverage, which have not been achieved until the HOP 151 observations. This made the identification of QS features very challenging. As a consequence, there are estimations of the total NE and IN fluxes, but they differ significantly by up to an order of magnitude.

As seen in the SOHO/MDI observations, the NE carries a total flux

of 10^{23}-10^{24} Mx over the entire solar surface (Simon et al. 2001; Hagenaar et al. 2003, 2008). The Hinode/NFI magnetograms have verified these findings (Zhou et al. 2013). On the other hand, several ground-based observations indicated that the weak IN elements may harbor up to half of the QS magnetic flux. Using longitudinal magnetograms from the Big Bear Solar Observatory, Wang et al. (1995) estimated that more than 20% of the total QS flux resides in the IN. Soon after that, Meunier et al. (1998) determined that contribution of magnetic fields weaker than 1 kG is around 66% on average. Lites (2002) suggested that the IN harbors half of the QS flux, which is supported by the results from Zhou et al. (2013) based on the analysis of 6 individual NFI magnetograms. The disagreement between the results is caused by usage of different methods along with observations with moderate temporal coverage and/or spatial resolution. Nevertheless, the estimations do agree that the IN contributes considerably to the QS flux.

Since the NE and IN are important components of the solar magnetism, it is essential to determine their fluxes with more accuracy. The HOP 151 observations allow us to calculate the total NE and IN fluxes in a consistent way, and for the first time, to observe their temporal evolution on scales from hours to days. Moreover, our data give us the unique opportunity to study whether the QS flux exhibit spatial variations by examining individual supergranular cells and their surroundings. To do this, we sum the flux of magnetic elements detected with YAFTA in NE and IN regions. Therefore, we first have to separate the NE from the IN in the selected data sets. This is explained in Section 4.3. Then, we determine the properties of the detected QS structures (Section 4.4), and calculate the total NE and IN fluxes in Section 4.5. Finally, we will describe the evolution of magnetic flux in individual supergranular cells (Section 4.6).

4.2 Selection of data sets

From the five data sets obtained in the framework of HOP 151, we decided to use two of them throughout the thesis. These are data sets 1 and 4, displayed in Figures 2.12 and 2.13. Details about these observations are listed in Table 2.3.

Although being the shortest sequence recorded, data set 1 is exceptionally valuable. It has the largest FOV among all HOP 151 observations, and contains several supergranular cells and NE areas. The large FOV

permits us to derive statistically significant estimates of the NE and IN fluxes that do not depend on the evolution of single cells. At the same time, we can also use this data set to study the sources and sinks of magnetic flux in individual supergranules. One of them is located at the center of the FOV and can be followed from the formation phase until it becomes a fully developed supergranular cells.

Data set 4 is complementary to data set 1. It has a smaller FOV (like other data sets), but a much longer duration. Despite the smaller FOV, several supergranules are visible. The largest one, with its adjacent NE, is located perfectly at the center of the FOV. The ∼40 hours of continuous measurements of data set 4 allow us to determine how the IN and NE fluxes vary with time. Moreover, this observational sequence is complemented by XRT and EIS observations, making it suitable for future investigations of the emergence of IN flux in the photosphere and above.

4.3 Separation of NE and IN Regions

To calculate the total flux of the NE and IN and study their temporal evolution we have to consider NE and IN elements separately. However, YAFTA does not know if the detected elements belong to the NE or IN, so we have to find criteria to classify them. To identify NE and IN regions, some authors use criteria based on the flux density and/or size of the magnetic elements. However, the separation is difficult because the QS flux distribution is continuous and does not show a clear boundary between the IN and NE (Hagenaar et al. 2003; Thornton & Parnell 2010; Zhou et al. 2013). To avoid the uncertainties associated with the use of a fixed flux threshold, we define the IN as the interior of supergranular cells. The space beyond the IN is the NE.

Supergranular cells are found using the Dopplergram time sequences. We divide them in 2 hr intervals and apply Local Correlation Tracking (LCT; November & Simon 1988) to each subsequence. Periods of 2 hr are long enough to wash out granular and mesogranular flows, and short enough so that the evolution of supergranular cells is captured with sufficient temporal resolution. The LCT algorithm calculates horizontal velocities by comparing small subfields in two successive images. The subfields are defined by a Gaussian tracking window of FWHM of 60 pixels (9.″6). With this criterion, we suppress small-scale convective patterns, keeping only the large scale supergranular flows. From the resulting horizontal ve-

locity field, we calculate divergence maps. The borders of NE regions are identified by tracking the evolution of passively advected tracers (corks) on the divergence maps as shown in the examples of Figure 4.1. Assuming that the NE flux is located at the edges of supergranules, we manually define the cell interior following the cork distributions and avoiding strong magnetic flux structures (pink contours in the right panels). To obtain a smooth transition of the cell boundaries from one subsequence to the next, we use linear interpolation. The evolution of the borders between two consecutive subsequences can be seen in Figure 4.1.

Magnetic features that appear in the interior of supergranular cells (i.e., inside the boundaries defined above) are taken to be IN elements. Elements born by fragmentation of an IN element are also classified as IN patches. IN elements keep their character unless they merge with NE features or cancel with them inside a NE region, in which case they become part of the NE and are tagged accordingly.

The identification of NE patches is more involved. In the first frame of the sequences, elements that have their flux-weighted centers (FWC) inside of a NE region are considered to be NE features. Also, only in the first frame, elements that are touching a NE region are counted as NE elements because we do not know their history.

Since NE patches are moving with time, we check their area overlap to identify them in the following frames. For all $i > 1$ frames, magnetic features are marked as NE elements if they overlap more than 70% with NE structures from the previous $i - 1$ frame or if their FWCs are located inside any of the NE patches detected in the $i - 1$ frame.

When an element appears by fragmentation, it is considered to belong to the NE if its parent is already marked as a NE structure. At any time, an element that appears in situ inside the NE is considered to be part of the NE. Only when NE fragments enter into IN region and merge with stronger IN elements, they convert into IN patches from that moment on. This is done for computational convenience—otherwise they would quickly turn all IN patches into NE features through mergings with other elements inside the supergranular cell. Figure 4.2 shows examples of NE and IN patches detected in selected frames in data sets 1 and 4. Pink contours represent the boundaries between the IN and the NE.

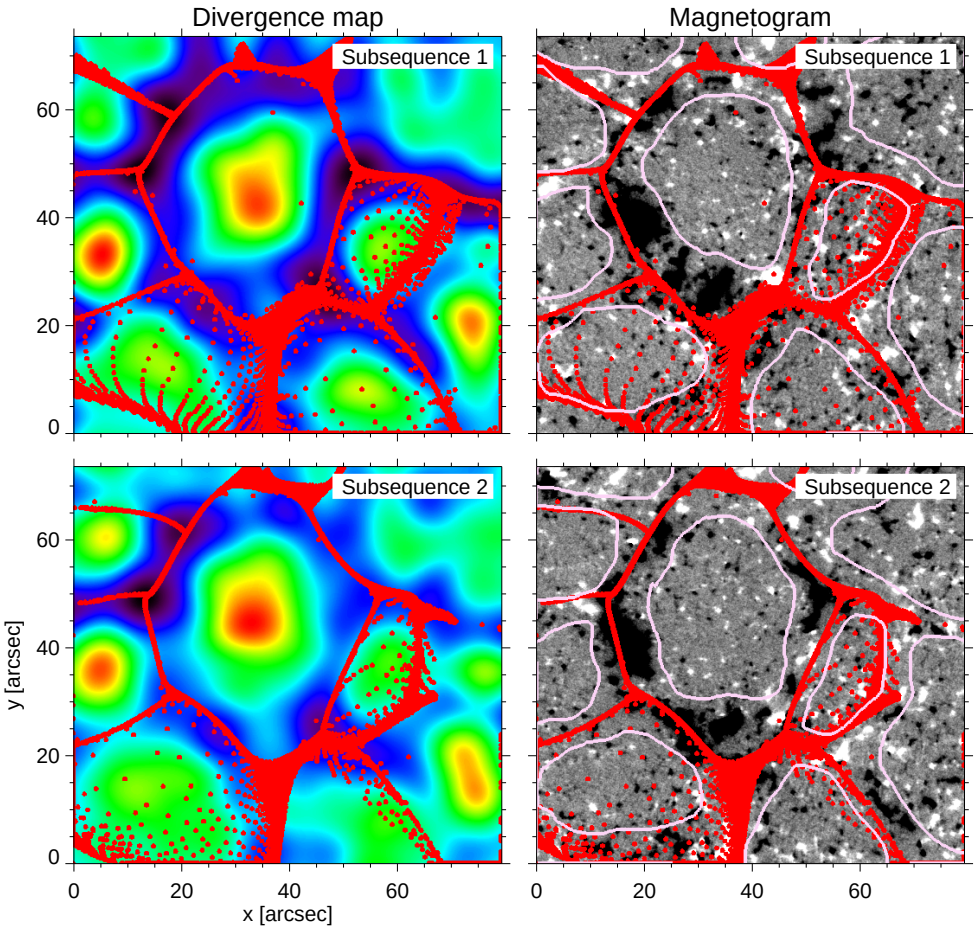

FIGURE 4.1:— Local correlation tracking of two consecutive Dopplergram subsequences from data set 4. *Left column:* Divergence maps and corks passively advected on them. *Right column:* Borders of supergranular cells (pink contours) on the corresponding magnetograms.

4.4 Properties of IN and NE elements

The first step in characterizing the QS flux is to determine the properties of the patches detected in the magnetograms. The most important physical parameters are the flux density, the size and the total unsigned flux. With the flux density and the size of the patches, the total unsigned flux is computed. This is the quantity that will be used to estimate the flux budget of the quiet Sun.

To characterize the properties of IN and NE patches, we use 265,933

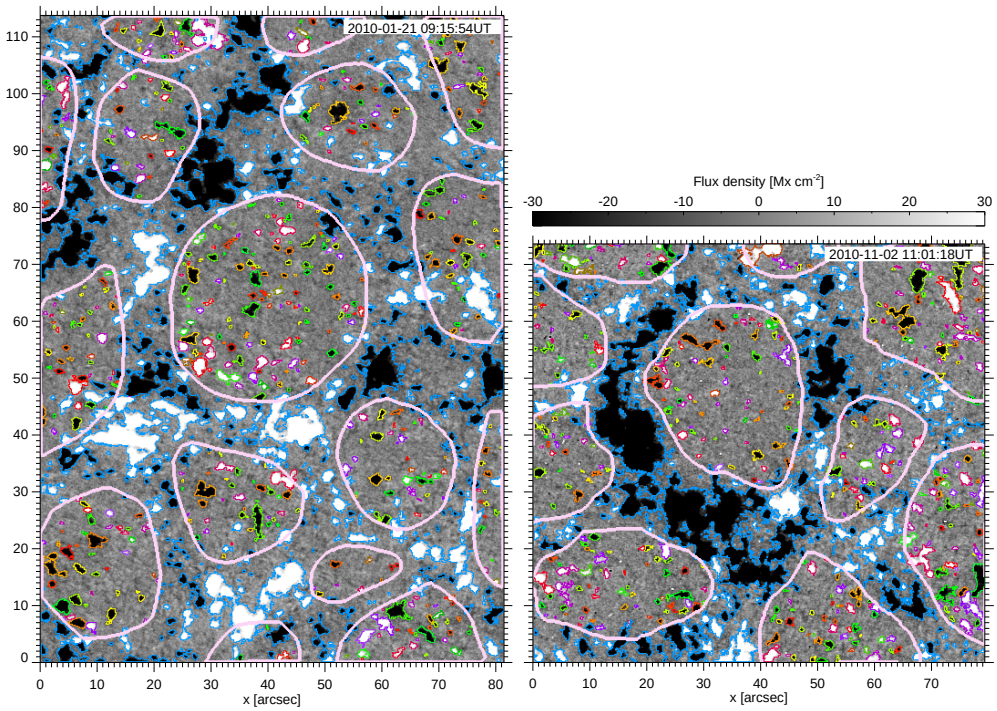

FIGURE 4.2:— NE and IN features in data sets 1 (left panel) and 4 (right panel). The former are identified with blue contours, the latter with other colors. The border of IN regions are marked with pink lines.

and 316,097 elements detected by YAFTA in the entire FOV of data set 1 and 4, respectively. IN patches are noticeably more abundant than NE patches, accounting for more than 60% of all the elements. Such a result is expected from their larger appearance rates and shorter lifetimes.

4.4.1 Magnetic flux density

The mean unsigned magnetic flux density of an element is defined as:

$$\overline{\phi} = \sum_{i=1}^{N} |\phi_i|/N,$$

where N is the total number of pixels of the element and ϕ_i is the flux density for each pixel i. The distributions of mean flux densities for NE and IN patches in data sets 1 and 4 are shown in the upper panels of Figure 4.3. They are very similar, with peaks around 26 Mx cm^{-2} for

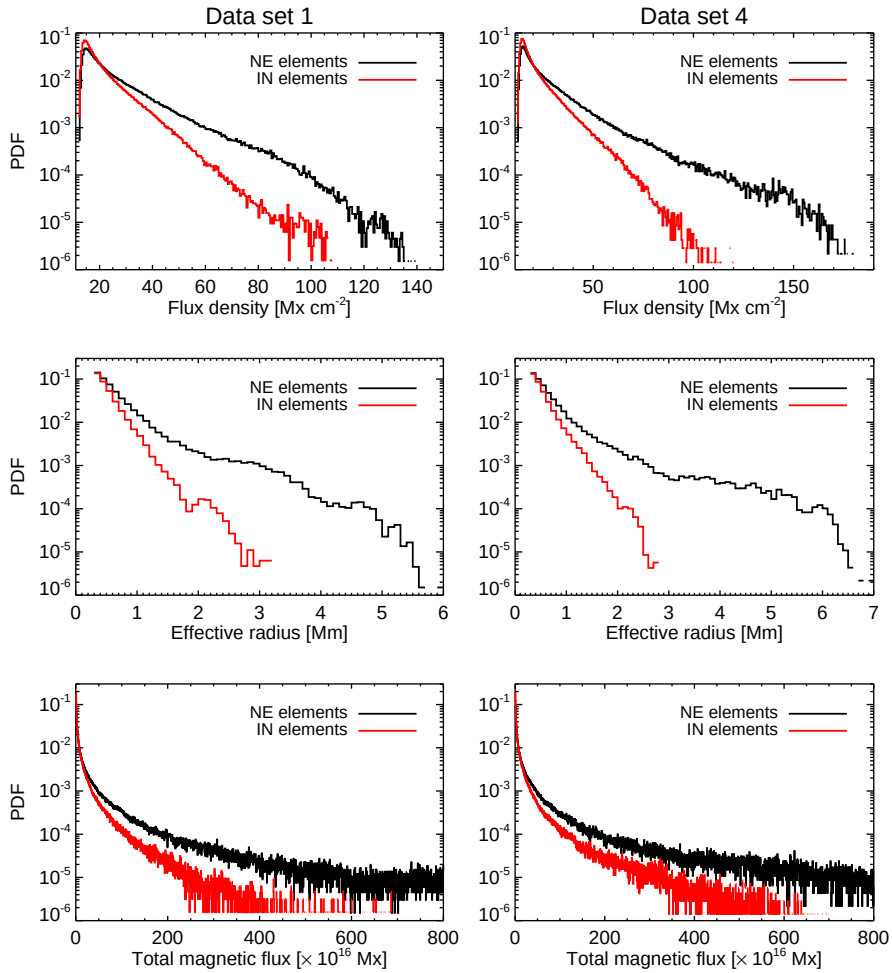

FIGURE 4.3:— Distributions of the flux density (top panels), the size (middle panels) and the total flux (bottom panels). They are calculated separately for NE (black curve) and IN patches (red curve) in data sets 1 (left column) and 4 (right column).

NE and 20 Mx cm^{-2} for IN elements. However, the maximum mean flux densities are 180 Mx cm^{-2} and 120 Mx cm^{-2}, respectively. The strongest IN flux features correspond to those appearing in clusters. Usually, same-sign patches in clusters merge together to form stronger structures and eventually form NE elements. The cutoff at 12 Mx cm^{-2} is a consequence of the criteria used to identify magnetic patches.

4.4.2 Size

The distributions of the size of the detected elements are displayed in the middle panels of Figure 4.3. The mean effective radius of NE elements is determined to be around 1.4 Mm. IN elements are in general smaller, with an effective radius of approximately 0.7 Mm. However, some IN features appearing in clusters may reach the size of strong NE patches. The largest NE and IN features detected in our data have radii of 7 Mm and 3 Mm, respectively.

4.4.3 Total magnetic flux

The total flux distributions for the two data sets are similar (Figure 4.3, bottom panels). In the data sets used here, IN elements have a total unsigned flux of about 13×10^{16} Mx. The net flux is less than approximately 10^{16} Mx, indicating that the two polarities are nearly balanced. By contrast, NE elements are much stronger, with mean unsigned fluxes of 72×10^{16} Mx in data set 1 and 123×10^{16} Mx in data set 4. Both time sequences exhibit a certain amount of NE flux imbalance. The largest occurs in data set 4, where the net flux of the NE patches is 79×10^{16} Mx, or 65% of the mean unsigned flux. The calculated parameters are summarized in Table 4.1.

4.5 Total flux of the NE and IN

After we compute the flux of individual magnetic features we can examine the temporal evolution of the total NE flux in the two data sets (Figure 4.4). The total flux (black curve) has been calculated adding the unsigned fluxes of all detected NE elements. We also show the flux of positive and negative patches (blue and red curves, respectively). Gaps in the curves are the result of transmission problems and data recorder overflows. Other short interruptions coincide with magnetograms that contain recovered stripes.

The total unsigned NE flux in data set 1 is 4.25×10^{20} Mx on average. For data set 4, the corresponding value is 3.98×10^{20} Mx. Thus, the NE harbors a total flux of $5.5 - 8.0 \times 10^{23}$ Mx over the entire Sun. The temporal evolution of the total flux inside the NE in data sets 1 and 4 remain stable over time, showing only small fluctuations (less than 5% and 8% rms, respectively). This indicates that the NE reached a steady state.

TABLE 4.1:— Physical parameters of the detected IN and IN magnetic elements.

	Data set 1	Data set 4
Total number of elements	265 933	316 097
IN regions		
Total IN elements	160 859	215 775
Positive IN elements	80 293	108 902
Negative IN elements	80 566	106 873
Mean unsigned flux [$\times 10^{16}$ Mx]	12.7	13.6
Mean flux [$\times 10^{16}$ Mx]	−1.1	−0.08
Mean flux density [Mx cm^{-2}]	20.1	20.2
Mean effective radius [Mm]	0.73	0.74
NE regions		
Total NE elements	105 074	100 322
Positive NE elements	50 777	43 065
Negative NE elements	54 297	57 257
Mean unsigned flux [$\times 10^{16}$ Mx]	71.7	123.3
Mean flux [$\times 10^{16}$ Mx]	−7.6	−78.6
Mean flux density [Mx cm^{-2}]	25.6	25.9
Mean effective radius [Mm]	1.3	1.5

Individual supergranular cells are appearing, evolving, and disappearing in the time sequences, but the curves are stable and do not react to these changing conditions. FOV is sufficiently large as for the results not to depend on their variations. Negative polarity elements contribute 55% of the total NE flux in data set 1, whereas the NE regions of data set 4 are predominantly unipolar with 81% of the flux being negative.

Just like in NE regions, the magnetic flux of the IN exhibits steady evolution (Figure 4.5). The total IN fluxes are in average 6.9×10^{19} Mx and 6.5×10^{19} Mx, respectively. The rms fluctuations are larger than in the NE but do not exceed 14% of the total IN flux. The IN is practically in balance where negative flux accounts to 55% (data set 1) and 51% (data set 4).

We find that 14% of the total QS (NE+IN) flux is in the IN. However, the minimum and maximum contributions of the IN to the QS flux are 10% and 20%, respectively.

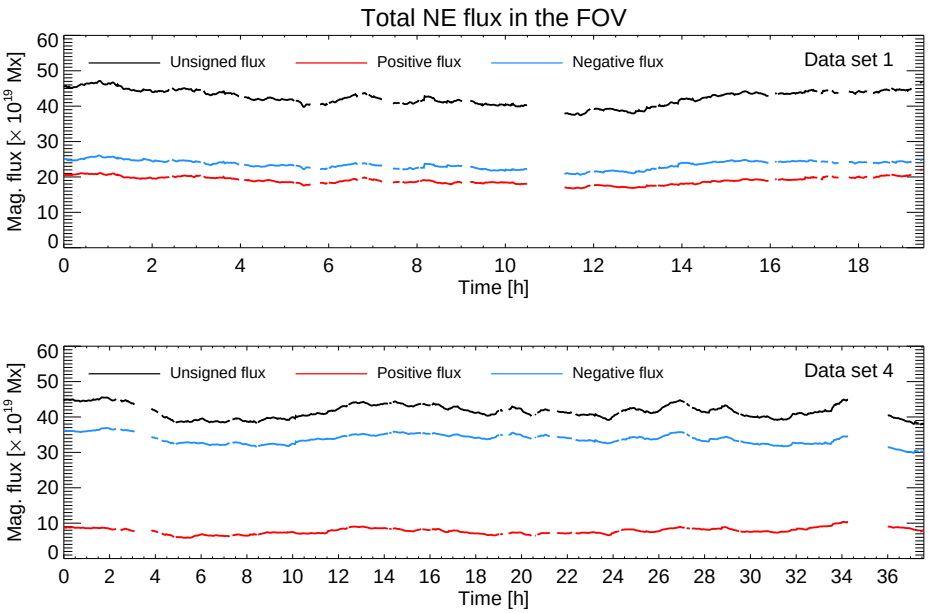

FIGURE 4.4:— Temporal evolution of the total unsigned, positive and negative flux of NE regions (black, red and blue curves) in data sets 1 and 4.

4.6 Flux budget of individual supergranular cells

To understand whether the QS flux manifests spatial variations we have to study the evolution of individual supergranular cells. In data sets 1 and 4 we can examine two well defined supergranules. They are shown in Figure 4.6. NE patches around the cells are marked with blue contours and IN elements with contours other than blue. The IN region is enclosed by pink contour. We will now describe in detail these cells. For the sake of illustration of the complete evolution of a supergranular cell, we will start with the cell visible in data set 4 for which we also have the SDO observations.

Data set 4 shows the temporal evolution of a mature supergranular cell located at the center of the solar disk. The exact location with its surrounding can be seen in Figure 4.7, which displays observations of the Sun obtained with the Atmospheric Imaging Assembly (AIA; Lemen et al. 2012) onboard the SDO, and with the HMI. They were recorded on 2 November 2010 at 16:00 UT. From top to bottom, the panels represent the corona (193 Å), the quiet corona and upper transition region (171 Å),

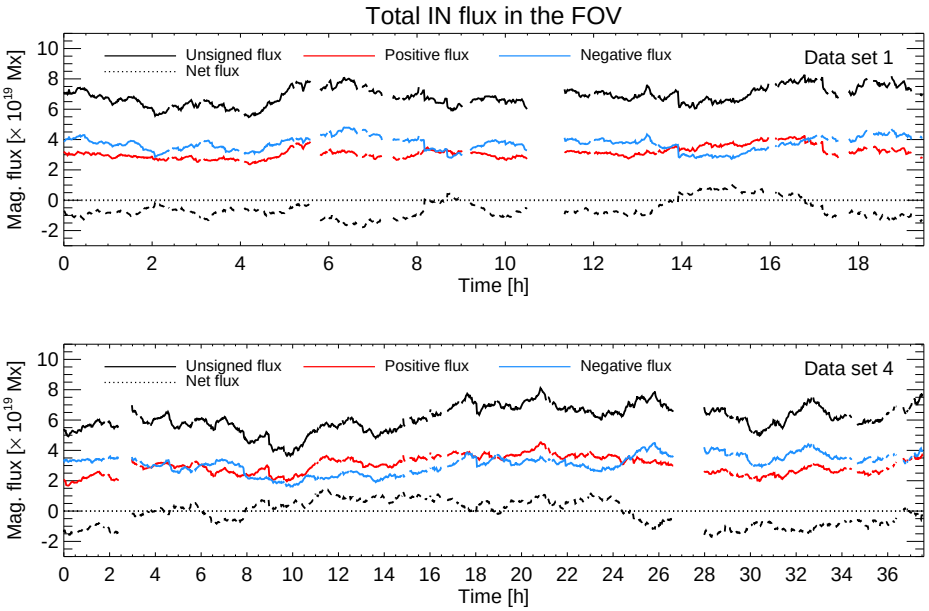

FIGURE 4.5:— Temporal evolution of the IN flux in data sets 1 and 4. The total unsigned, positive and negative fluxes are shown with the black, red and blue curves, respectively. The dashed line represents the net flux.

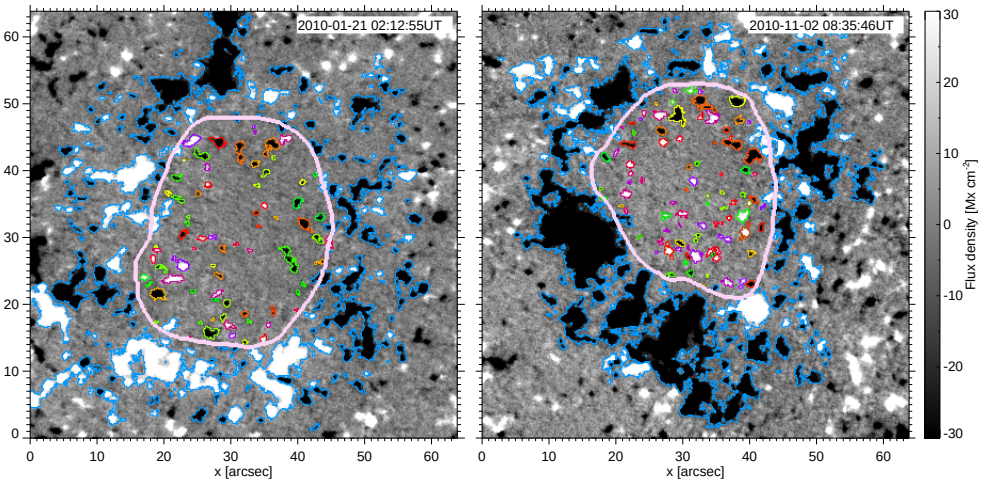

FIGURE 4.6:— Individual supergranular cells in data sets 1 and 4 (left and right, respectively). The cell interiors are outlined by pink contours and the surrounding NE flux features are marked with blue contours. IN patches have contours other than blue.

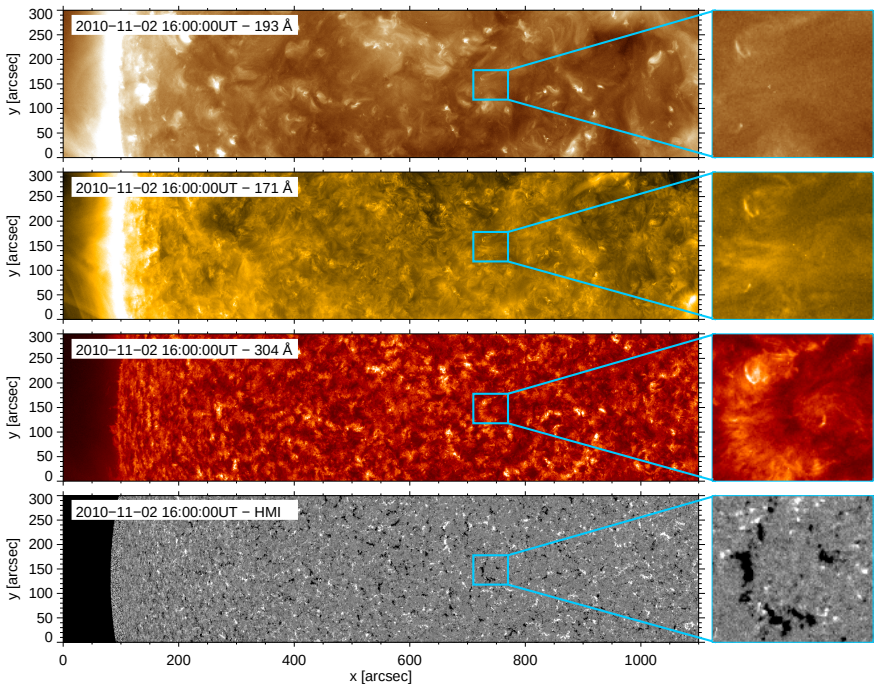

FIGURE 4.7:— SDO images showing the Sun around the region seen in data set 4. They were taken on 2 November 2010 at 16:00 UT. From top to bottom are displayed SDO/AIA channels at 193, 171, and 304 Å, and the HMI longitudinal magnetogram. The blue squares outline the supergranular cell from data set 4, and are zoomed-in in the right column.

chromospheric and transition region plasma (304 Å), and photospheric longitudinal magnetogram (HMI). We can see that the cell occupies very quiet area. The emission in the AIA passbands is visible above the NE, in the chromosphere. At times, it is also detected in the interior of the supergranule. This is probably caused by cancellations between IN and NE elements. In the transition region and corona, the signal is weak although some features can be seen in the NE. The other AIA coronal channels do not reveal any activity.

Figure 4.8 shows the entire evolution of the cell as seen by the SDO/HMI. Its lifetime is $\sim$ 50 hours. The upper left panel shows the formation phase of the supergranule, and its end is displayed in the lower right panel. From the HMI magnetograms we know that the cell started to form about 5-6 hours before the first NFI magnetogram was taken. It can be clearly recognized for 5-6 more hours after the NFI observations ended. Thus,

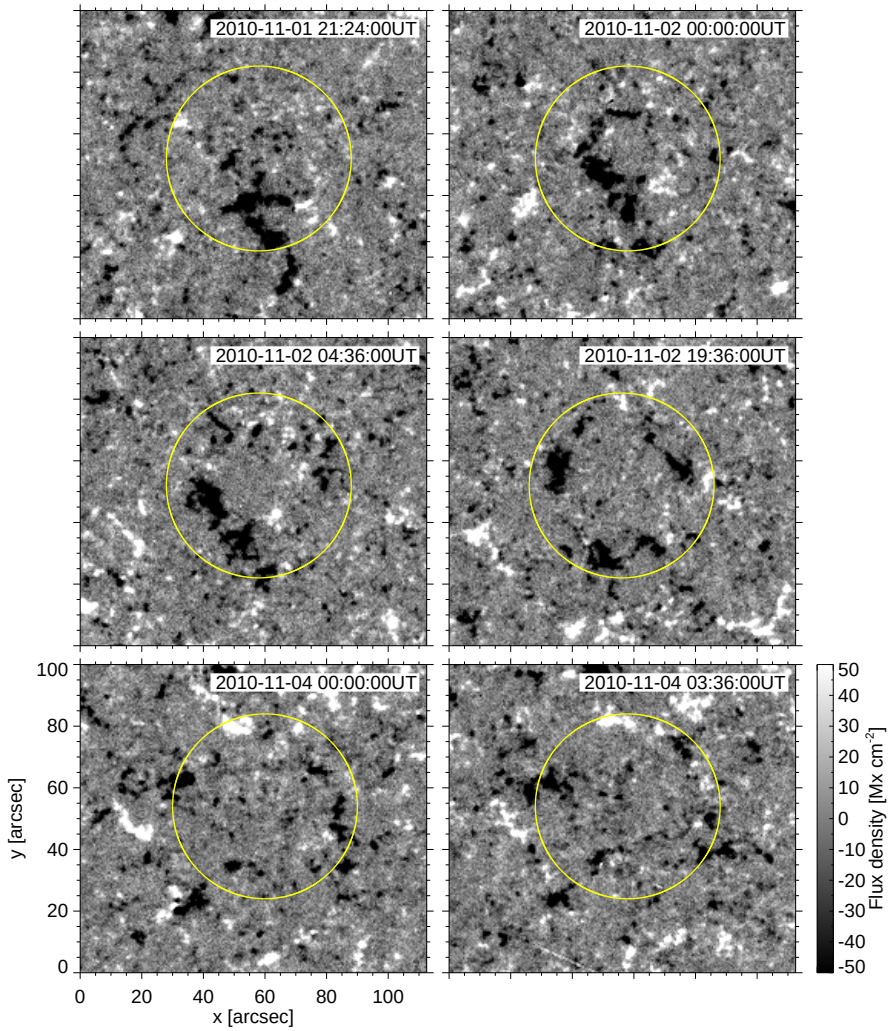

FIGURE 4.8:— SDO/HMI longitudinal magnetograms showing the development and the disintergration of the supergranular cell observed with the Hinode/NFI on 02-03 November 2010. The cell is roughly enclosed by the yellow circle. From the upper left to the bottom right panel we can see the full evolution of the supergranular cell from appearance to disappearance. The middle panels correspond to the first and last frames in the NFI sequence.

with data set 4 we cover approximately 80% of its temporal evolution, capturing the late formation and early disappearance phase of the cell.

Although the HMI observations track the supergranule from its appearance to disappearance, we can not use them to study IN magnetic

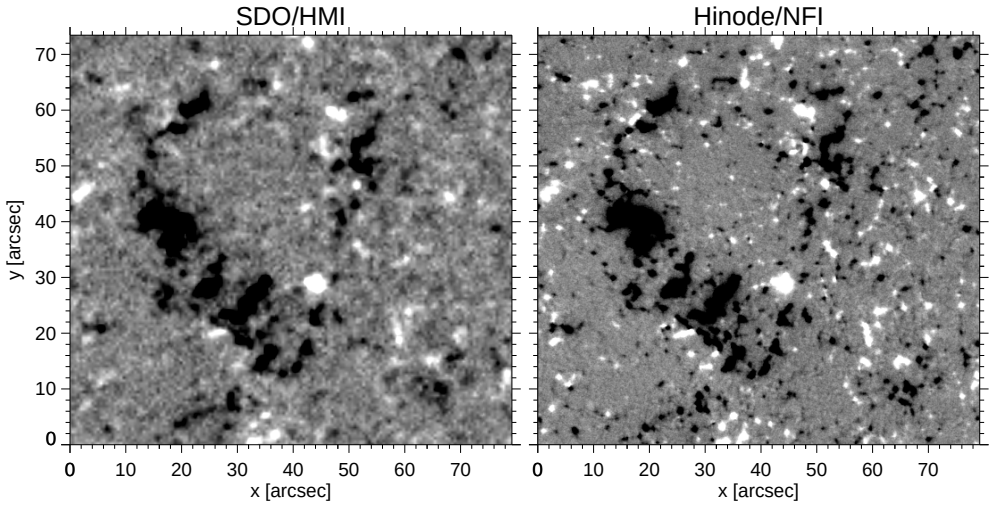

FIGURE 4.9:— Comparison of the same supergranular cell observed with the HMI (left panel) and the NFI (right panel). In the HMI observations only the strong NE patches are visible. The NFI magnetogram has much higher spatial resolution and sensitivity, showing weak internetwork features inside the cell. The magnetograms were taken on 2 November 2010 at 08:36. They are saturated at ± 50 Mx cm^{-2}.

fields. From Figure 4.9, we can easily see advantage of high-sensitivity, high spatial resolution observations such as those from the NFI. The HMI observes the Sun with a spatial resolution of $1''$ and moderate sensitivity, and therefore only NE structures can be seen. By contrast, the NFI magnetogram (right panel) reveals a carpet of weak IN elements all over the FOV.

Figure 4.10 shows the flux history of the supergranule of data set 4 and the surrounding NE, along with the sizes of the two regions. The total unsigned flux in the interior of the cell is on average 1.3×10^{19} Mx, while in the NE it is by an order of magnitude larger (3.55×10^{20} Mx). In terms of polarity balance, the IN region is practically in equilibrium where only 55% of the total unsigned flux comes from the negative polarity features. Contrary to the IN, the NE region is dominantly negative, 86% of the flux is of negative polarity, which is maintained over time. However, such flux imbalance is not produced solely by flux generated in the interior of the supergranule. Most of the strong negative NE patches are formed much before the cell itself. From the HMI magnetograms it can be seen that these NE elements migrated from south to north. They created the NE

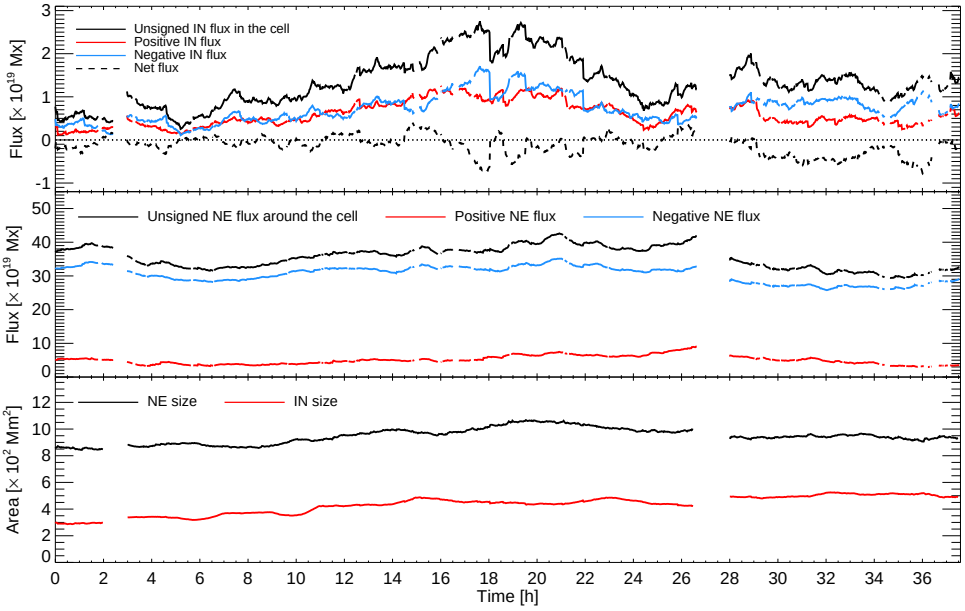

FIGURE 4.10:— The total fluxes and area variations of the supergranular cell of data set 4. *Top panel:* The total unsigned (black), positive (red) and negative (blue) IN flux inside the supergranular cell. *Middle panel:* The total unsigned NE flux is shown with black solid curve. Its positive and negative components are marked with red and blue lines, respectively.*Bottom panel:* Area of NE (black) and IN (red) regions.

region together with the flux appeared in two large clusters (ephemeral regions) in the same zone.

The total flux of the IN grows substantially with time. The main reason is appearance of the flux clusters. In this particular case, it increased from 0.3×10^{19} Mx to 2.8×10^{19} Mx, i.e., by a factor of 9 in the period from 4 to 18 hours. After strong patches left the cell and entered into NE region, the IN flux started to diminish. The flux also increased due to growing area of the IN region (from 290 to 520 Mm^2), but this is the secondary effect.

During $\sim$ 37 hours of observations, the unsigned NE flux of the central cell did not change a lot, while it size increased from 800 to 1100 Mm^2. The rms variation of the total unsigned flux of the NE is 15%.

The temporal evolution of the supergranule of data set 1 is displayed in Figure 4.11. Similarly to the cell of data set 4, total unsigned flux in the IN is 1.4×10^{19} Mx on average. The total flux of the NE is again

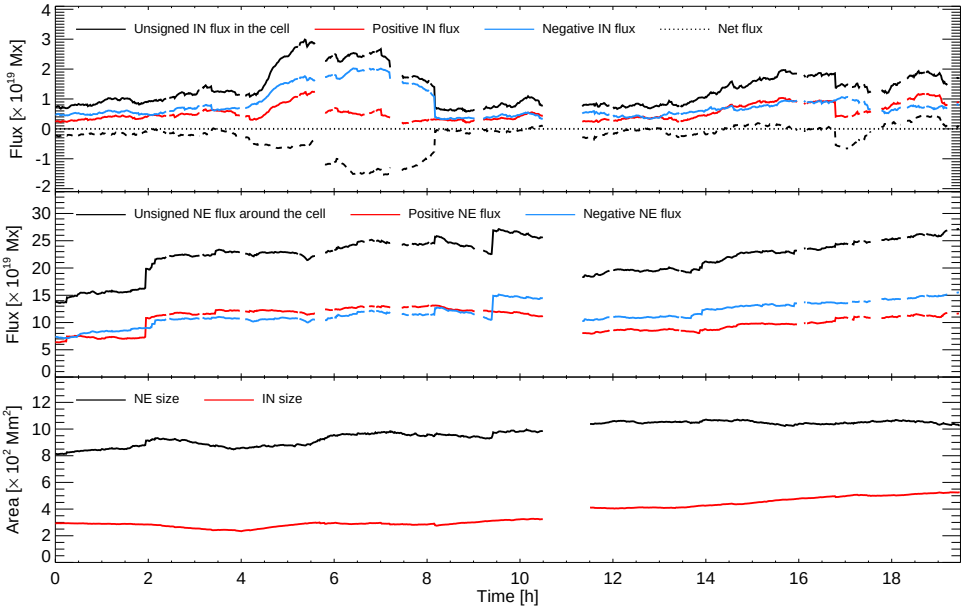

FIGURE 4.11:— Same as Figure 4.10 but for data set 1.

much higher and accounts to 2.2×10^{20} Mx.

The cell is slightly negative in both IN and NE regions. On average, 60% of the IN and 53% of the NE flux is negative. However, this numbers do not imply that more negative elements appear inside the cell. The dominant negative polarity is due to interactions between IN and NE features. For example, the flux imbalance between 5 and 8 hr is mainly generated by mergings of strong, positive IN patches (that appear in clusters) with NE patches. The negative counterparts remain inside the cell. In this way, the IN region lost positive flux.

The supergranule of data set 1 goes through its formation phase at the beginning of the observations. At that moment, the flux in its interior (0.8×10^{19} Mx) and the surrounding NE (13.8×10^{19} Mx) is relatively small. With the appearance of strong clusters around 4 hr, the supergranule increases its flux by a factor of 5. Magnetic elements formed inside the IN region migrate toward the NE and interact with patches there, increasing the total NE flux. The most apparent case occurs at 8 hr when strong IN features (formed in clusters) leave the cell. In this way, they increase the negative flux of the NE and reduce the total IN flux to 0.8×10^{19} Mx. The subsequent evolution of the supergranule reveals that the IN flux increases

significantly whenever clusters appear on the solar surface (as at 14 hr). Just like in the cell of data set 4, the area expansion from 230 Mm^2 to 530 Mm^2 have moderate effect on the growth of flux.

The surrounding NE gain flux from the IN elements but also from the patches coming from outer regions. This is manifested as a sudden increase of NE flux, for example at 2 and 9 hr. By the end of the observations, the total NE flux reached 27.2×10^{19} Mx. At the bottom panel, we can see that the size of the NE region increased from 800 Mm^2 to 1070 Mm^2.

4.7 Summary and conclusions

In this chapter we studied the evolution of IN and NE magnetic flux using data sets 1 and 4 obtained in the framework of the HOP 151 observational proposal. These measurements give us the opportunity to study for the first time the evolution of QS magnetic fields in the range 10^{16}-10^{20} Mx on scales from hours to days.

To estimate the contribution of the IN and NE to the QS flux budget we had to analyzed them separately. To this purpose, we used local correlation tracking to distinguish between IN and NE regions and set of criteria to accordingly classify detected flux patches.

We calculated the characteristic physical parameters and their distributions for IN and NE elements. These parameters are the flux density, the size and the total unsigned flux. Their mean values for IN features are 20 Mx cm^{-2}, 0.7 Mm, and $\sim 13 \times 10^{16}$ Mx, respectively. NE magnetic elements have higher flux densities (26 Mx cm^{-2}) than IN elements, and are larger on average (1.4 Mm). They have total fluxes of up to $\sim 120 \times 10^{16}$ Mx.

In our observations, the total IN and NE fluxes in the FOV are very stable and exhibit only small variations with time, showing the steady-state nature of the QS fields. Regarding the global characteristics of IN and NE regions our main findings are the following.

1. On average, 14% of the QS flux is in the form of IN elements. Small variations of $\pm 5\%$ are possible.

2. Extrapolating our results on the entire solar surface, the total IN and NE fluxes are $0.7 - 1.1 \times 10^{23}$ Mx and $5.5 - 8.0 \times 10^{23}$ Mx, respectively.

3. IN regions are in nearly perfect polarity balance. By contrast, NE regions show clear polarity imbalances. The largest imbalance is measured in data set 4, and is 85% in favor of negative flux.

The temporal evolution of the IN flux of the two supergranular cells studied here is very similar. Its main characteristics are summarized bellow.

4. The mean unsigned IN flux of individual supergranules is $\sim 1.4 \times 10^{19}$ Mx.

5. The total flux of the IN is changing significantly when clusters of magnetic elements appear. At these moments, IN flux may increase almost by an order of magnitude.

Our results suggest that IN regions are very dynamic. They gain rapidly a lot of flux, but it is also efficiently removed from the IN. This may have important consequences for the maintenance and origin of the QS fields. To explain the changes of flux content in individual cells we will have to determine flux appearance and disappearance rates.

The NE regions around the two supergranular cells are very different. The NE flux in data set 1 is increasing with time, as the cell develops, with average value being $\sim 2.3 \times 10^{20}$ Mx. The positive and negative fluxes remain in balance during the evolution. On the other hand, the mean total flux is much higher in data set 4 ($\sim 3.5 \times 10^{20}$ Mx). This NE is dominantly unipolar, suggesting that it is not formed only by the IN patches generated in the interior of the cell it encloses. However, this does not exclude the possibility that NE is formed by IN flux from different supergranular cells.

To understand how NE features are formed, in the next chapter we will study contribution of IN flux to the NE.

5

Contribution of the IN to the NE magnetic flux

5.1 Introduction

In the previous chapter we have found that the solar IN harbors a total unsigned flux of $\sim 9 \times 10^{22}$ Mx over the entire solar surface, while the NE contains $\sim 6.7 \times 10^{23}$ Mx. Thus, the NE flux is about 7 times larger than the IN flux and comparable to the flux of active regions.

Despite its importance, the origin of the NE flux is still an open question. It is generally accepted that the NE is maintained by the appearance of so-called ephemeral regions (ERs), strong bipolar structures that emerge into the solar surface near the boundaries of supergranular cells (Harvey et al. 1975b; Title 2000; Chae et al. 2001; Hagenaar 2001; Hagenaar et al. 2003, 2008). Schrijver et al. (1997) developed a set of equations to model the distribution and evolution of the NE flux taking into account the balance between flux emergence, fragmentation, merging, and cancellation of ERs. They determined the flux emergence rate of ERs to be 7.2×10^{22} Mx day^{-1} from data taken by SOHO/MDI and concluded that bipolar ERs alone can explain the flux of the NE, with only a small fraction of the NE originating from active regions. Indeed, they found that the total NE flux can be replaced by newly emerged ERs in 1.5–3 days. The ratio of the total NE flux to the ER flux appearance rate gave a similar flux replacement time of 40 hours (Schrijver et al. 1998). Using a

kinematic model, Simon et al. (2001) studied the transport of ER fragments by granular and supergranular flows and verified that the injection of bipolar ERs at the rates observed with MDI would lead to a statistically stable NE. Hagenaar et al. (2003) confirmed the importance of ERs for the maintenance of the NE and inferred flux replacement times of 8–19 hours, also using MDI observations. Later, Hagenaar et al. (2008) revised this value down to only 1–2 hours based on higher cadence MDI magnetograms.

However, the NE is also in close contact with the very dynamical and changing IN, a reservoir of flux that may play an important role in sustaining the photospheric NE. This possibility was first explored in the 1980s, the conclusion being that the short-lived IN elements cannot account for more than 10% of the total NE flux (Martin 1990). However, such an estimate was obtained from the ground using observations of moderate-to-poor spatial resolution. Lamb et al. (2008) suggested that the IN elements hidden to MDI and other ground-based magnetograms may supply more flux to the NE than ERs. With the much better stability and larger sensitivity of the Hinode HOP 151 observations, we are in a position to assess in a reliable way the actual contribution of the IN to the NE flux and revise the conclusions if necessary. Here we will tackle this problem by analyzing the interactions between IN elements and NE patches in the full FOV of data sets 1 and 4, over the full duration of the observations.

In Section 5.2 we explain how we calculate the IN contribution to the NE flux and in Section 5.3 we show the results. We also estimate the fraction of the IN contribution to the NE due to ERs in Section 5.5. We then discuss how the NE flux is maintained on the solar surface in Section 5.6, and give a summary in Section 5.7.

5.2 Calculation of the IN contribution to the NE

To study how IN magnetic elements contribute to the maintenance of the NE, we have to look for the IN features that interact with NE patches. Merging and cancellation are the only two processes through which IN elements can modify the flux of the NE. These processes involve a direct interaction between IN and NE elements. IN features that merge with NE patches add flux to the NE, while those canceling with opposite-polarity elements remove flux from the NE. Their respective contributions are

determined as follows.

5.2.1 Merging events

When an IN element merges with an NE patch, the flux it contributes to the NE is calculated in the frame where it is visible as an individual feature for the last time. We consider only the pixels of the IN element that do not overlap with any of the NE patches of the previous frame, to avoid including NE flux due to fragments that YAFTA may have erroneously added to the IN feature. The same is done for IN elements that enter the NE and merge with NE elements but survive the interaction because they are dominant in flux.

To be as accurate as possible, we check in each frame whether all the pixels of the IN elements contributing to the NE are detected correctly. This is important because there may be some pixels exchanged between the IN and NE elements that we are not aware of because they carry small amounts of flux. Since these pixels are attached to elements that do not change their flux and/or size by more than a factor of 2, they are not corrected by the method explained in Section 3.3.2. We account for this by calculating the difference between logical masks of NE elements in frame i and frame $i-1$. All pixels different from zero in the difference mask are assigned the flux densities they had in frame i. On such "partial" magnetogram we apply the downhill method. Every flux structure larger than 16 pixels exceeding a signal threshold of 3σ is taken to be a magnetic element. Finally, we dilate these features to the nearest neighboring pixel. If they overlap the NE mask from the current frame and their flux-weighted centers are not located inside of the NE region, they are counted as contributing IN fragments. We note that we use the downhill method only to this purpose. Calculating contribution of the IN elements to the NE using the downhill method instead of the clumping method would not be suitable because the interpretation of interactions between flux patches would be much more difficult (if at all possible).

A complex example of an IN element merging with NE patches is shown in Figure 5.1. This element interacts with other IN features during the sequence (e.g., at $\Delta t = 9.0$ and 15.0 min). The red contours indicate the flux contributed to the NE by each of the IN elements.

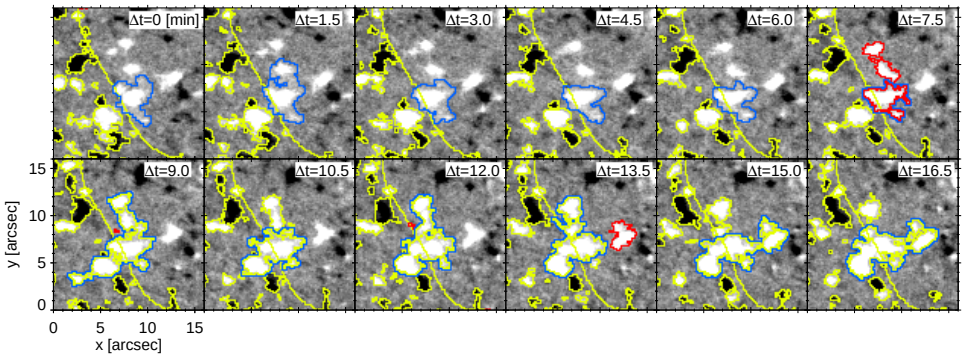

FIGURE 5.1:— Example of flux transfer from the IN to the NE through merging. An IN element (blue contours) merges with a NE patch at $\Delta t = 9.0$ min and becomes a NE feature itself. NE elements are indicated with yellow contours. This specific IN patch undergoes several mergings with other IN patches during the sequence, revealing the full complexity of interactions between magnetic flux concentrations. For example, two smaller IN features to the North merge with it at $\Delta t = 9.0$ min. The same happens with another IN element to the West at $\Delta t = 15.0$ min. The red contours mark the boundaries of the IN patch right before merging with the NE, as well as the boundaries of the other IN elements that will become part of it. The flux they enclose is lost by the IN upon interaction of IN elements with NE patches.

5.2.2 Cancellation events

Cancellation events are found by searching for all closely located, opposite-polarity elements that disappear in the current frame. More precisely, we take an IN element at the moment of disappearance, dilate its border by two pixels and, if it overlaps an NE patch of opposite polarity, count the IN element as a canceling flux feature. To determine how much flux it removes from the NE, we go back in time and take the total flux of the IN element at the moment when the cancellation started (i.e., when the IN patch touched the opposite-polarity NE element for the first time). This flux is corrected for all the changes caused by the merging and fragmentation processes that might happen during the cancellation event.

The same procedure is repeated for NE elements that disappear by cancellation with IN elements. The latter may survive the process, but they remove flux from the NE. Their contribution is taken to be the flux of the NE patch at the beginning of the cancellation.

In Figure 5.2 we show an example of an IN feature canceling with NE patches and how the interaction is interpreted.

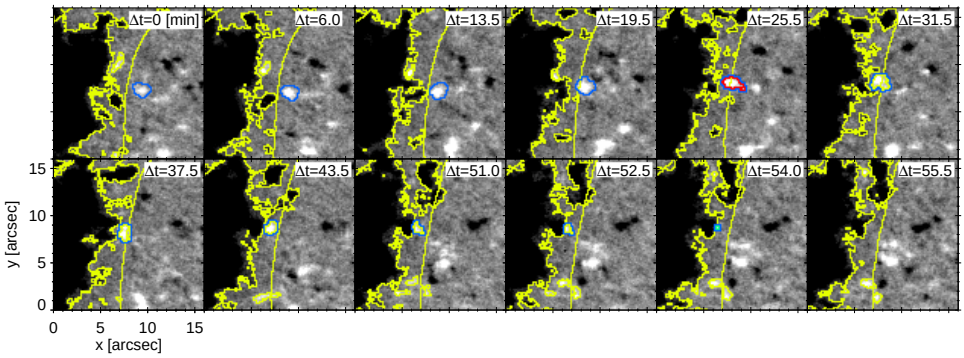

FIGURE 5.2:— Example of an IN element (blue contours) canceling with NE patches (yellow contours). The contours are those provided by YAFTA, except that the blue ones have been expanded by 1 pixel for visualization purposes. The red contours mark the flux used to compute the contribution of the IN element to the NE. The green contour at $\Delta t = 54$ min outlines the canceling IN element in the last frame where it is visible.

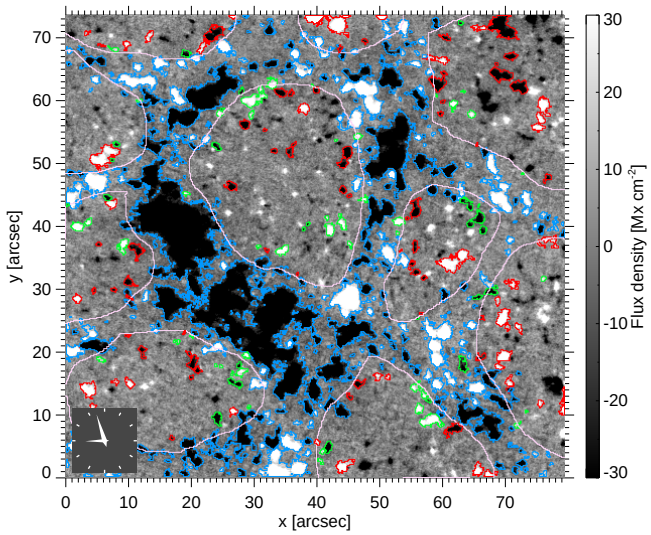

FIGURE 5.3:— Snapshot from an animation of data set 4 showing the IN flux patches that will eventually supply flux to the NE. Red contours mark IN elements contributing to the NE through merging processes while those undergoing cancellations are outlined with green contours. Blue contours represent NE patches. The borders of supergranular cells are marked with pink contours.

5.2.3 Total contribution

To calculate how much IN flux is deposited in the NE through interactions between IN and NE elements, we sum up the (unsigned) flux of all the

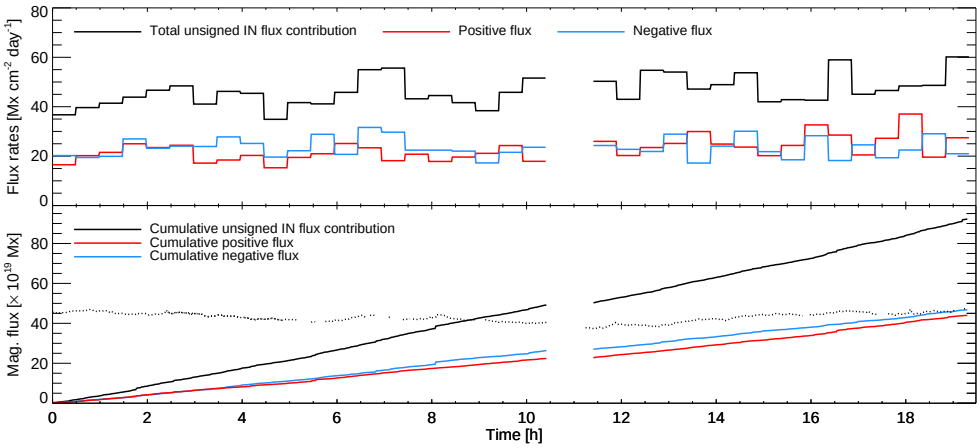

FIGURE 5.4:— Contribution of the IN to the NE in the full FOV of data set 1. We use 30 minute bins to represent the data. *Top panel:* Total contribution (black), defined as the sum of the unsigned flux of the IN elements that merge or cancel with NE patches. The positive and negative flux contributions are also shown (red and blue, respectively). *Bottom panel:* Cumulative contribution of the IN to the NE flux. The solid line represents the total unsigned IN flux transferred to the NE, while the red and blue lines show the positive and negative IN flux that reaches the NE. The total unsigned NE flux in the entire FOV is indicated by the dotted line.

IN elements undergoing mergings and cancellations with NE patches over the full FOV. Then, we compute the corresponding flux transfer rates per unit area and unit time.

The animation[1] of Figure 5.3 shows all the IN elements that eventually merge and cancel with NE patches in red and green, respectively, for data set 4. They have been identified as explained in the previous subsections, using the YAFTA tracking results corrected by our code. NE elements are outlined with blue contours.

5.3 IN flux contribution to the NE

The black curve in the top panel of Figure 5.4 shows the total unsigned IN flux deposited in the NE as a function of time for data set 1. The data points have been binned in 30 minute intervals. The average flux transfer rate is 44 Mx cm^{-2} day^{-1} in the full FOV, or 2.6×10^{24} Mx day^{-2} over the entire solar surface. The curve shows fluctuations due to strong IN

[1]The movie can be downloaded from `http://spg.iaa.es/pub/downloads/apjGosic_2014.mp4`.

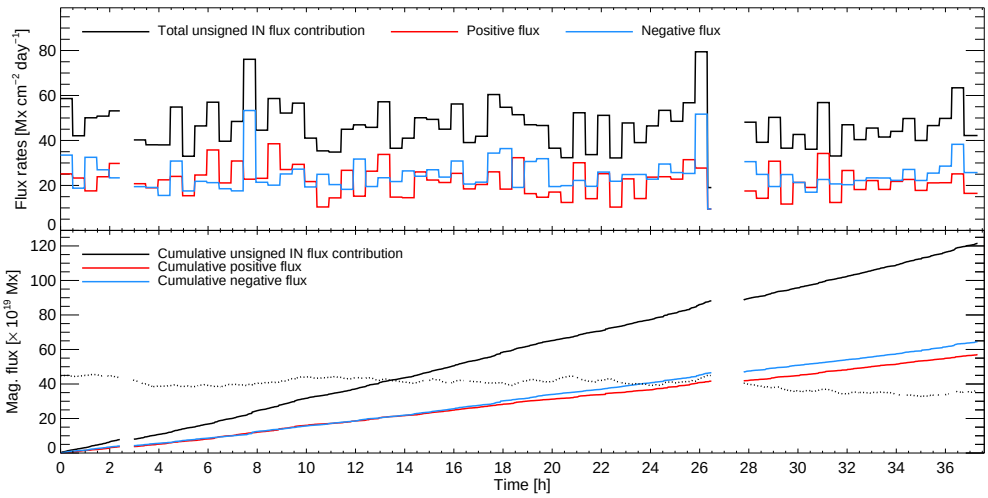

FIGURE 5.5:— Same as Figure 5.4, but for data set 4.

magnetic elements that appear in clusters and eventually migrate to the NE, where they interact with NE patches. The most prominent examples occur at 7 and 16 hr. The positive and negative IN fluxes reaching the NE are very similar, as can be seen by comparing the red and blue curves. On average, 52% of the total IN flux transferred to the NE is negative and 48% is positive. This nearly perfect polarity balance is a consequence of the polarity balance that exists in the IN regions of data set 1 (see Table 4.1 and Figure 4.5).

In the bottom panel of Figure 5.4 we show the cumulative IN contribution to the NE considering all the fux deposited in the NE (black line). The slope of the curve does not change with time, indicating that the IN supplies flux to the NE steadily. The dotted line shows the unsigned NE flux present in the FOV. Very remarkably, in only 9 hours the NE receives from the IN as much flux as it contains. About half of this flux is negative and the rest is positive, so the net flux of the NE is barely modified. However, the IN supplies an enormous amount of negative flux to the NE and a similar amount of positive flux. This represents the largest source of flux for the NE known to date.

The IN contribution to the NE flux in data set 4 is displayed in the top panel of Figure 5.5. Just like in data set 1, the curves show variations caused by interactions of strong IN elements with NE features. On

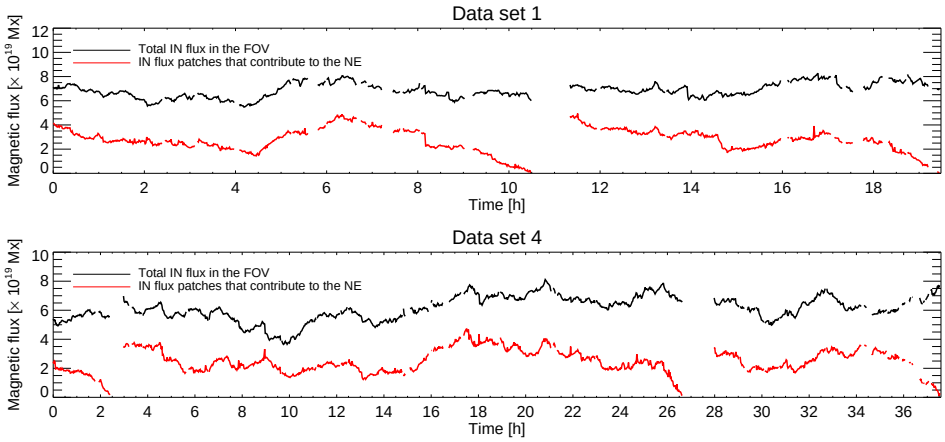

FIGURE 5.6:— Fraction of the total IN magnetic flux that converts into NE flux, for data sets 1 and 4 (top and bottom, respectively). The red curves show the instantaneous flux carried by the IN patches that will convert to the NE at any later time. They are on average 2.8 and 2.7 $\times 10^{19}$ Mx in data sets 1 and 4, respectively. For reference, the black curves represent the corresponding total unsigned IN flux in the entire FOV of the two data sets (6.9 and 6.5 $\times 10^{19}$ Mx, respectively).

average, the IN injects flux into the NE at a rate of 45 Mx cm^{-2} day^{-1}, or 2.7×10^{24} Mx day^{-1} over the entire solar surface (black curve). Nearly 53% of the total IN flux transferred to the NE is negative and 47% is positive (blue and red curves, respectively). Thus, also in this case there is almost perfect balance of positive and negative fluxes.

We display the cumulative flux contribution from the IN to the NE in the bottom panel of Figure 5.5. The black solid line represents the total unsigned IN flux transferred to the NE, while the red and blue lines show the positive and negative flux contributions, respectively. Again, the dotted line indicates the total NE flux in the FOV. According to these curves, the IN transfers to NE regions as much flux as they contain in only 13.5 hr.

Our results clearly demonstrate that the IN continually supplies flux to the NE through interaction of IN elements with NE patches. The consequences of this will be discussed later.

5.4 Fraction of the IN flux transferred to the NE

After appearing in the interior of supergranular cells, IN elements migrate toward the cell boundaries where the NE resides. However, not all IN elements end up in the NE, since many of them disappear in situ or cancel with other IN elements before reaching the NE. Here we study what fraction of the IN flux actually makes it to the NE.

The black curves in Figure 5.6 show the temporal evolution of the IN flux in the entire FOV of data sets 1 and 4 (c.f. Figure 4.5). The total flux carried by the IN patches that interact with the NE at any later time is indicated with the red curves. They are on average 2.8 $\times 10^{19}$ Mx in data set 1 and 2.7 $\times 10^{19}$ Mx in data set 4. For this calculation we take into account all fragmentations and partial cancellations that the elements may undergo before interacting with the NE. Close to the end of each continuous observing period there are artificial drops of the IN flux contributing to the NE. They reflect the lack of information about the evolution of IN elements during the data gaps. Some of the elements may interact with the NE, but they are not counted because it is not possible to identify them, producing drops in the curves.

On average, we find that 41% of the IN flux in the interior of supergranules eventually contribute to the NE. Both data sets show very similar percentages. The rest of elements disappear inside the IN by cancellations or in-situ fading and never reach the NE. Thus, a significant fraction of the observed IN flux is incorporated into the NE, emphasizing the importance of the IN for the maintenance—and arguably also the existence—of the magnetic NE.

5.5 Contribution of ERs to the NE

The current paradigm is that ERs provide the flux needed to maintain the network. This view appears to be in conflict with the enormous amount of flux transfered by IN elements to the NE, which would indicate that the main source of flux for the NE is actually the IN and not ERs. To examine this apparent conflict, we have determined the percentage of the IN flux transfered to the NE that is due to ERs.

Detecting ERs in the Hinode magnetograms is difficult because YAFTA does not recognize the presence of large-scale structures. To circumvent this problem, we manually identified ERs as clusters of mixed-polarity flux

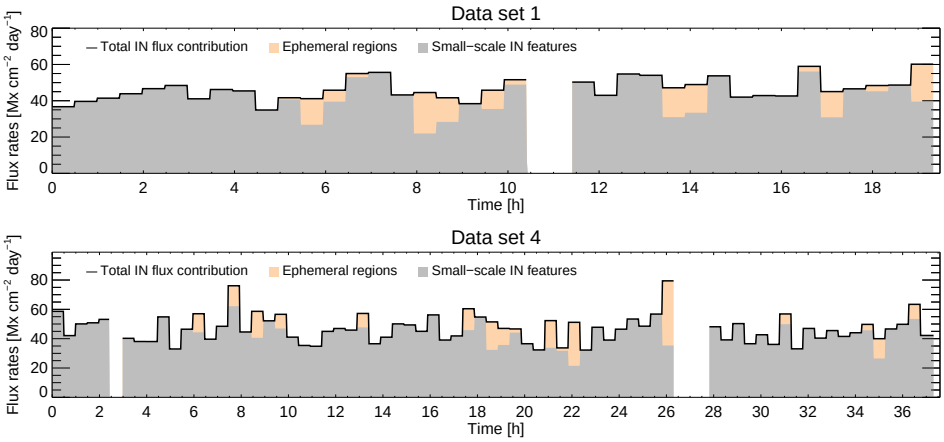

FIGURE 5.7:— IN contribution to the NE flux in the form of isolated IN elements (gray shaded areas) and ER patches (orange shaded areas). The total IN contribution is represented by the black curves.

patches appearing together and separating from each other with time. To qualify as an ER, at least one element in the cluster had to reach a flux content of 3×10^{18} Mx, the threshold set by Hagenaar et al. (2003). The individual ER patches were then tracked and counted as contributing to the NE if they had interactions with NE elements. We detected five such ERs in data set 1 and nine in data set 2, roughly consistent with the appearance rate of 430 per hour estimated by Chae et al. (2001) over the entire solar surface. Moreover, the total unsigned flux brought to the surface by ERs in our data sets is $\sim 2.8 \times 10^{23}$ Mx day^{-1}, which surpasses the appearance rate of 7.2×10^{22} Mx day^{-1} estimated by Schrijver et al. (1997). Therefore, we detect more flux appearing in ERs than it was derived from MDI data.

The contribution from ERs to the NE flux is shown in Figure 5.7. The black curves represent the total IN contribution to the NE already displayed in the top panels of Figures 5.4 and 5.5. For each 30 minute bin we separate the flux transferred to the NE by isolated IN patches (gray shaded areas) and the ER patches described above (orange shaded areas).

As can be seen, ERs play only a minor role in the flux transfer from the IN to the NE. In both data sets, they inject about 1.9×10^{23} Mx day^{-1} into the NE, but this is less than $\sim$8% of the total IN flux that reaches the NE in the two data sets. Thus, despite the large amount of flux they carry, ERs are not the main contributors to the NE flux. More than 90%

of the flux transfered to the NE comes from weak, isolated IN patches.

5.6 Discussion

We have shown that IN elements continuously supply flux to the NE, confirming the prediction by Lamb et al. (2008) that it should be possible to observed interactions between NE and IN elements on spatial scales not accessible to MDI. Indeed, we find that up to 41% of the magnetic flux that appears inside supergranular cells moves to the edges of supergranules and interacts with the NE. This occurs through mergings and cancellations of IN patches with NE elements. The former process adds IN field lines to the NE, while the later removes NE field lines. Mergings dominate over cancellations by a factor of $\sim$3.8 in data set 1 and $\sim$3.6 in data set 4, respectively (Gošić et al. 2014). The much higher rate of mergings we observe is in agreement with the results of (Iida et al. 2012, 2015), who studied the interactions between NE patches and also found a dominance of mergings over cancellations. However, its origin is still unknown.

The positive and negative IN fluxes transferred to the NE are very similar. Therefore, the IN does not add significant net flux to the NE, which is a consequence of the nearly perfect polarity balance of the IN. However, the IN deposits an enormous amount of unsigned flux in the NE, at a rate of $1.5 \pm 0.1 \times 10^{24}$ Mx day^{-1} over the entire solar surface. This means that the IN is capable of supplying the total NE flux in only 11 ± 2 hr.

Our estimates of the IN contribution to the NE flux are more realistic than those derived from MDI in two ways. First, MDI could not see most of the IN flux, while we use very sensitive NFI observations to detect the weak patches of the IN. Second, we obtain the instantaneous rate of flux transfer to the NE by adding the unsigned flux of all the IN elements that merge or cancel with NE features. This is a direct approach. In the past, methods based on average flux appearance and disappearance rates were used. Such methods can only give approximate results because a large fraction of the elements included in the average rates never interact with the NE, and therefore should not be counted. With these two improvements, our analysis shows that the temporal scale on which the IN could supply the total NE flux is of order 10 hr, i.e., much shorter than the 36–72 hours reported by Schrijver et al. (1997) but also significantly longer than the 1 hr found by Hagenaar et al. (2008).

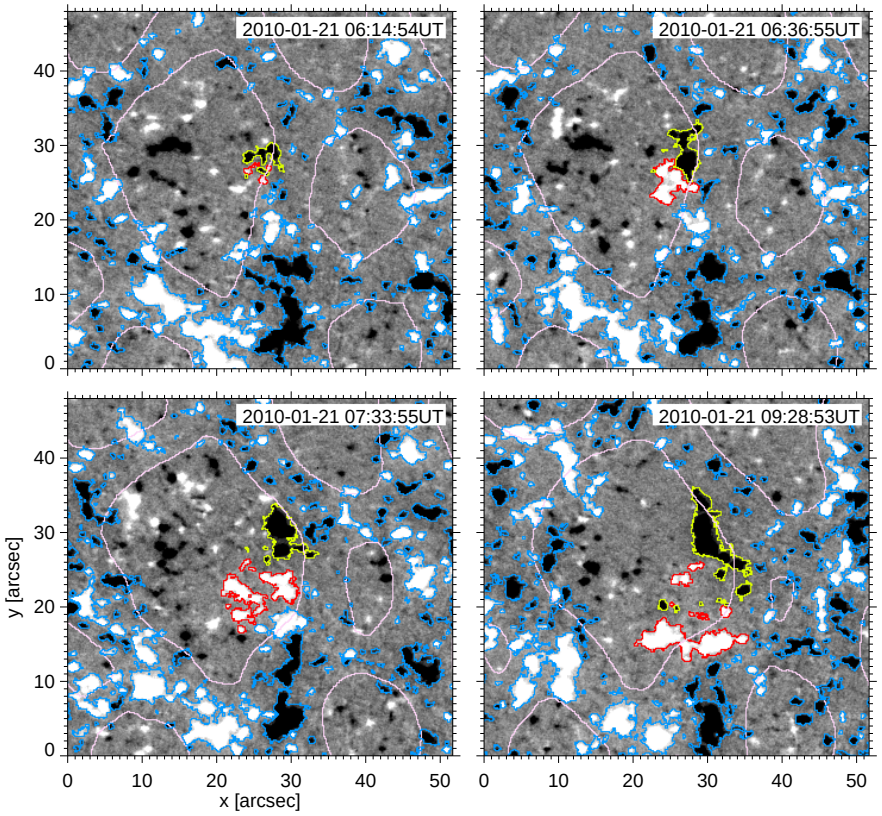

FIGURE 5.8:— Example of an ephemeral region (red and yellow contours) appearing at the border of the supergranular cell (pink contour) seen in data set 1. Network features are marked with the blue contours.

To see see how this result fits in with the currently accepted picture of NE flux maintenance, we have analyzed the contribution of ERs to the NE in our data sets. We considered as ERs all the clusters of mixed polarity patches emerging in the same area with at least one of the patches reaching 3×10^{18} Mx. An example of a detected ER is shown in Figure 5.8. From the upper left to the bottom right panel, we can see how a small number of magnetic elements emerge on the solar surface, just to be followed by a bunch of flux features that rapidly increase in flux and size. Many of them undergo mergings or cancellations with other patches of the cluster and/or with patches in their vicinity. Slowly, the positive and negative

elements separate from each other forming large, strong individual flux structures. In this particular case, the patches of the ER appeared at the border of the supergranular cell. The total unsigned flux carried by the ER is $\sim 1.4 \times 10^{19}$ Mx. It was observed during almost 4 hours, after which it converted into NE features. Such an evolution is the one expected for ERs: they appear at the border of supergranules, bring a substantial amount of flux to the surface, expand the cell borders, and eventually become part of the NE (Wang 1988a; Harvey & Zwaan 1993; Hagenaar 2001).

During the approximately 58 hr of monitoring of the QS performed with the Hinode NFI, we saw 14 ERs. This implies a total ER flux appearance rate of $\sim 2.8 \times 10^{23}$ Mx day^{-1} over the entire solar surface, which is slightly larger than the $\sim 7.2 \times 10^{22}$ Mx day^{-1} reported by Schrijver et al. (1997). In our observations, ERs transfer flux to the NE at a rate of $\sim 1.9 \times 10^{23}$ Mx day^{-1}, but this accounts for less than 10% of the total IN flux deposited in the NE. Therefore, we do not only observe a similar ER contribution to the NE as other authors, but we also detect a new, hitherto unknown contribution of small, weak IN elements that is actually 14 times larger. This suggests that the IN is the primary source of flux for the photospheric NE.

Thus, we are faced with a change of paradigm, since IN elements (and not ERs) seem to be the main contributors to the NE flux. However, it is important to recall that our NFI magnetograms show a continuous transition between ERs, clusters of IN elements, small-scale magnetic loops, and weak isolated IN elements (see Figure 4.3). An example of the emergence of a very small ER (or a large cluster of IN flux patches) is displayed in Figure 5.9. The properties and evolution of this feature are practically the same as those of the ER presented in Figure 5.8, the only difference being that it appears near the center of the supergranule rather than near the NE border. This cluster brought 5×10^{18} Mx to the solar surface and would have been too weak to be detected in observations of modest sensitivity and spatial resolution. This may explain why we observe more flux appearing in ERs than other authors. We recognize similar patterns of emerging flux everywhere inside IN regions and on all spatial scales. Therefore, we propose that there is no difference between ERs and clusters of IN elements: they all form part of a continuous flux and size distribution of magnetic elements in the solar IN.

Despite the large amount of IN flux transferred to the NE, the total

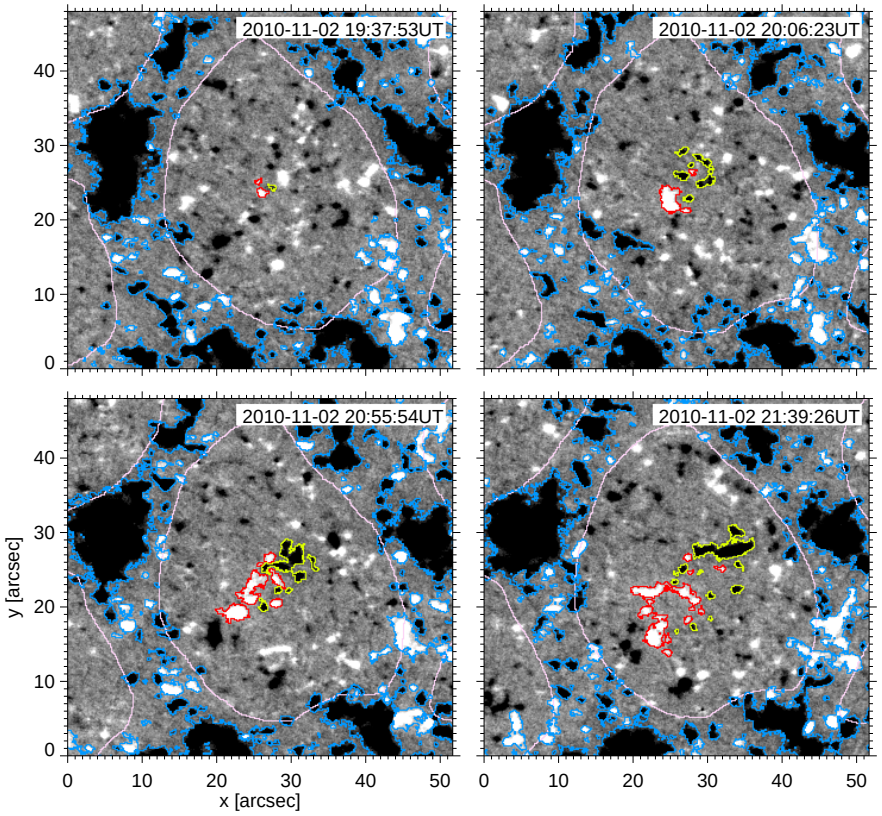

FIGURE 5.9:— Cluster of IN elements appearing inside of the central supergranular cell of data set 4.

NE flux does not change significantly with time. The input from the IN should increase both the positive and negative NE fluxes continually, but we do not observe them to grow. For this reason, the NE must be losing flux at a similar rate, i.e., NE field lines must be disappearing vigorously by cancellation or in-situ fading of magnetic elements. Through those processes, all the NE field lines can be expected to be replaced by IN field lines on relatively short time scales.

Such a reprocessing of magnetic fields may have important consequences for the energetics and dynamics of the upper atmosphere. Actually, cancellations of IN and NE features at the borders of supergranular cells often produce transient brightenings in the chromosphere and tran-

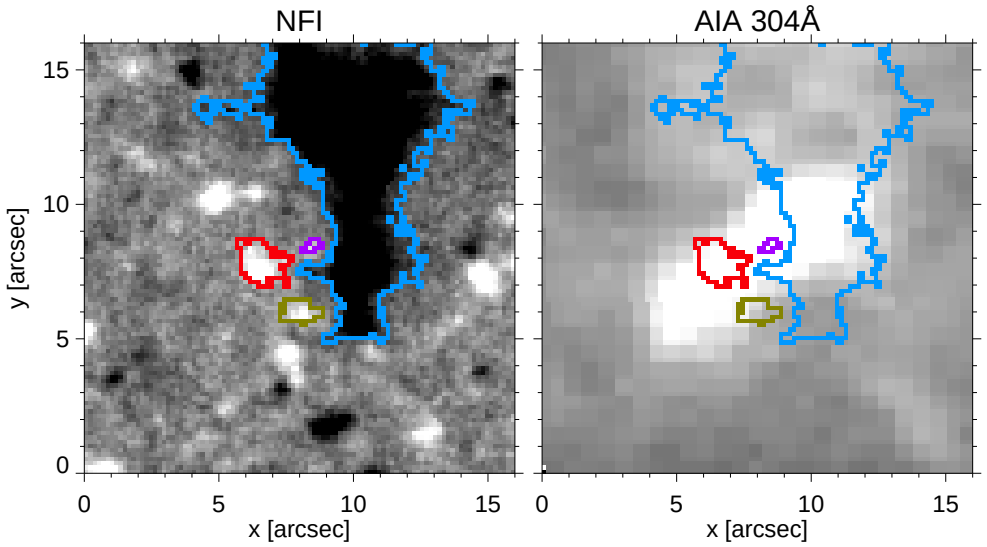

FIGURE 5.10:— Small positive polarity IN patches cancel with a strong negative polarity NE feature (left panel). This is associated with transient emission in the SDO/AIA 304 Å channel.

sition region. These events might be the signature of energy release and plasma heating, probably driven by magnetic reconnection of IN and NE field lines. An example is presented in Figure 5.10. The left panel shows small IN positive patches canceling with a large negative polarity NE patch (blue contour). A very strong, short-lived brightening can be seen above the cancellation site in AIA 304 Å images, indicating energy release (right panel). This example suggests that IN flux structures may be important contributors to chromospheric heating. The effects of mergings of IN elements with NE patches have not been explored as of yet and thus remain unknown.

5.7 Summary

Our goal in this chapter was to assess whether IN regions can provide sufficient flux to maintain the photospheric NE. To that end, we used unique HOP 151 observations to track IN and NE magnetic patches. We studied their interactions and calculated the flux contribution of the IN to the NE. The main conclusions of this analysis can be summarized as follows:

1. Small-scale IN elements are the main source of flux for the NE. The rate at witch the IN transfers flux to the NE is 1.5×10^{24} Mx day^{-1} over the entire solar surface.

2. The IN supplies as much unsigned flux as is present in the NE in only 11 ± 2 hours. Through mergings and cancellations, IN field lines can be expected to replace all the NE field lines on relatively short time scales.

3. The IN does not increase the net flux of the NE, since it supplies roughly the same amount of positive and negative flux.

4. Only about 10% of the total IN flux transferred to the NE is due to ERs. However, our data suggest that ERs are also IN magnetic structures representing the upper end of the IN flux and size distributions.

We have shown that most of the IN flux transferred to the NE comes from weak, isolated IN elements whose contribution was neglected until now. The maintenance of the solar IN itself, however, remains poorly understood. To shed light on that issue, we have to determine the instantaneous flux appearance and disappearance rates in the IN. This will be done in the next chapter. The goal is to reproduce the observed evolution of the total flux content of individual supergranular cells.

6

Internetwork flux appearance and disappearance rates

6.1 Introduction

Internetwork (IN) magnetic fields are observed to fill the interior of supergranular cells, enclosed by the photospheric network (NE). In Chapter 4 we showed that IN features harbor some 10^{23} Mx over the entire solar surface, which accounts for about 15% of the total quiet Sun (NE+IN) flux. To understand how the flux is maintained with time, we have to calculate precisely its appearance and disappearance rates.

Previous results indicated an enormous flux appearance rate in IN regions. The values quoted in the literature range from 10^{24} Mx day^{-1} (Zirin 1987) to 3×10^{26} Mx day^{-1} (Thornton & Parnell 2010). All of them are significantly larger than the 6×10^{21} Mx day^{-1} brought to the surface by active regions during the maximum of the solar cycle (Schrijver & Harvey 1994). However, the published rates vary by more than 2 orders of magnitude, indicating that they are not well determined yet. Much of the difference is probably due to the methods used to derive them. For example, some authors rely on automatic tracking algorithms while others prefer a manual detection of magnetic elements. Both approaches are affected by uncertainties and/or subjectivity (see, e.g., DeForest et al. 2007). Differences in the spatial resolution, noise level, cadence, and duration of the observations may also lead to different results. Another source

of disagreement is the fact that many estimates are based on fitting the observed flux distributions with power laws, rather than on following the evolution of individual elements. This method assumes constant appearance rates, but in reality we do not know if the flux appears at a constant rate or there are spatial and temporal variations across the solar surface.

To understand the flux balance of IN regions, we have to evaluate the processes by which flux is injected into and removed from the interior of supergranular cells. The IN gains flux through in-situ appearance of magnetic elements. Sometimes bipolar structures can be clearly identified, but most elements seem to appear as unipolar patches. On the other hand, flux is removed from the cell interior by fading (disappearance of features without obvious interactions with other elements) and cancellation. Fading has been reported to be the dominant process, accounting for 83% of the flux removal in the quiet Sun (Lamb et al. 2013). These authors determined a flux disappearance rate of 2.4×10^{26} Mx day^{-1} over the entire solar surface, but they did not distinguish between NE and IN regions.

Another important sink of IN flux that has been neglected until now is conversion of IN features into NE elements. Upon appearance, many IN patches reach the NE and interact with NE elements, disappearing from the supergranular cells. This is an essential mechanism to understand the flux balance of quiet Sun regions.

In this chapter we determine the rates of the four processes mentioned above, namely in-situ appearance, fading, cancellation, and flux transfer to the NE. To achieve that, we focus on the two individual supergranular cells visible in data sets 1 and 4 and compute the instantaneous fluxes that appear and disappear in their interiors.

6.2 Method

To determine the instantaneous flux appearance and disappearance rates in the two supergranular cells described in Chapter 4 we have to detect and track all the individual magnetic elements visible in their interiors. This is accomplished using YAFTA and correcting the tracking results as explained in Chapter 3. YAFTA allow us to follow individual flux patches from birth to death and see how their flux change with time.

Supergranular cells gain flux through in-situ appearance of magnetic elements and their subsequent evolution. The flux contributed by an el-

ement to the IN is not only its initial flux, but also any intrinsic flux increase it may experience with time. We refer to the sum of both contributions as total appeared flux. Flux disappears from the cell when IN elements fade inside the supergranule, cancel totally or partially with opposite-polarity IN elements, or leave the supergranule and interact with NE elements (flux transfer to the NE). Below we explain how the rates of these processes are calculated as a function of time.

6.2.1 Flux sources

The flux that appears in situ in a given frame is computed considering all IN patches that become visible for the first time in that frame. Identifying those elements is easy because YAFTA tags them with new labels. If the elements do not undergo interactions, their maximum flux is taken to be the flux they bring to the solar surface. IN elements tend to increase in flux upon appearance, so the maximum flux is usually several times the initial flux. When interactions occur, however, the maximum flux is not a good indicator of the flux appearing on the surface, because the element may simply grow through mergings with like-polarity patches. The flux gained in this way does not represent new flux and should not be counted. On the other hand, an element that appears in situ can fragment a few frames later, and the fragments themselves may continue to gain flux. Such a flux increase needs to be added to the flux appearance rate. Fragments are tagged by YAFTA as children of their parents, so they are easy to detect.

Thus, one has to be careful with interactions to derive reliable flux appearance rates. In practice, we go through each of the elements assigned a new label by YAFTA in a given frame—either because they appeared in situ or because they fragmented from an existing element. We examine how they gain flux over time, correct for mergings and fragmentations, and sum all the contributions to get the total flux they bring to the surface. The process is illustrated schematically in Figure 6.1. The solid line represents the flux evolution of an IN element during its lifetime. The moments of appearance, disappearance, and interactions are marked with dots. Each dot has a value from $F0$ to $F10$, which corresponds to the flux content in those particular moments. $F2$ and $F7$ coincide with sudden flux increases due to mergings with weaker elements. The maximum observed flux is $F7$, but this value is the result of one such merging. $F5$ would be the maximum flux in the absence of interactions. There are two fragmentations, which decrease the flux from $F3$ to $F4$ and

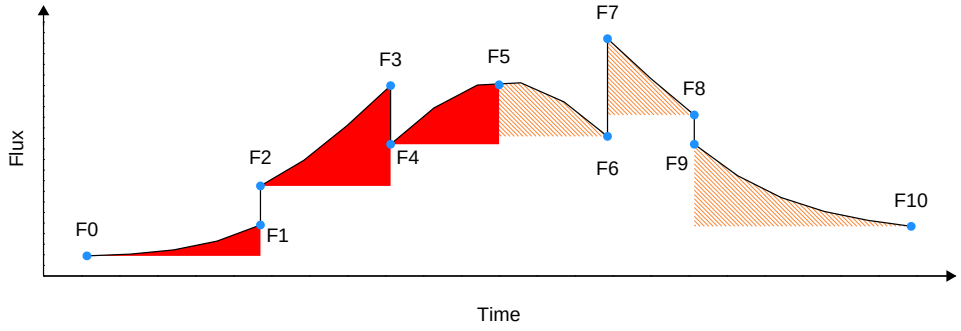

FIGURE 6.1:— Sketch of the flux evolution of typical IN magnetic elements. The red shaded areas represent flux gained by an element during its lifetime. The orange shaded areas represent the flux lost by fading until the element disappears (either by in-situ fading, cancellation, or merging with a stronger flux patch). Blue dots mark the moments of appearance, disappearance, and interactions.

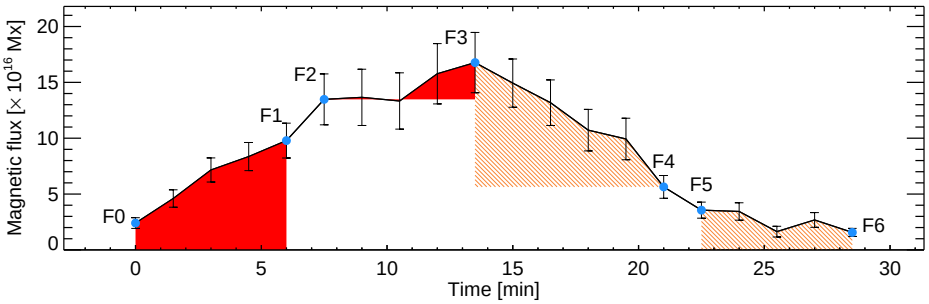

FIGURE 6.2:— Same as Figure 6.1 but for a real magnetic element detected with YAFTA.

from $F8$ to $F9$, respectively.

We calculate the total flux the element brings to the supergranular cell by adding together the initial flux F_{init} and the flux increases from one checkpoint to the next (blue dots), i.e.,

$$F_{\text{app}} = F_{\text{init}} + (F1 - F0) + (F3 - F2) + (F5 - F4). \tag{6.1}$$

If the element appeared in situ, we take $F_{\text{init}} = F0$. If it is a fragment of an existing patch, then $F_{\text{init}} = 0$. The flux F_{init} is assigned to the moment the element was first detected (also for fragments). The other contributions in equation (6.1) are evenly distributed over their corresponding intervals.

Now the evolution of a real IN element that appears in situ is shown in

Figure 6.2. In this case, $F_{\rm init} = 0$. The flux increases from $F0$ to $F1$ after which the element merges with a weaker IN feature and the flux abruptly increases to $F2$. Later, the maximum flux is reached ($F3$). Therefore, the total appeared flux in this case is $F_{\rm app} = (F1 - F0) + (F3 - F2) = 1.3 \times 10^{17}$ Mx.

By adding the flux carried by the patches that appear in-situ and through fragmentation we obtain the total flux appearance rate. For completeness, we also compute the flux appearance rate using only the initial flux of the features that appear in situ. We do this because the initial flux is a well-defined quantity that does not depend on interactions between flux patches. This rate represents the flux that discrete magnetic elements bring to the solar IN right at the moment of appearance, before they experience any perturbation.

It should be clear by now that a very accurate tracking of magnetic elements is mandatory to obtain reliable flux appearance rates. In particular, false detections of disappearances followed by appearances of the same element must be avoided. This problem occurs frequently due to fluctuations in the signal of the magnetic elements. They may exhibit flux densities below the detection threshold during a few frames, only to return to their previous state after such episodes. We correct for this problem as explained in Section 3.3.1. The correction decreases both the flux appearance and disappearance rates by 10%, compared with the original YAFTA results.

Another problem that we have to take care of is in-situ appearance of IN elements followed by merging with existing NE patches in the same frame. YAFTA does not detect these features and therefore their flux is not included in the flux appearance rates. We identify such elements by comparing the shapes of the NE elements that are inside the cell with the shapes they had in the previous frame, looking for large size changes. When we find 16 or more contiguous pixels in the non-overlapping area, they are taken to be a newly-appeared IN element which merged with the NE patch right away. In our observations, such a correction increases the appearance rates by approximately 5%. Yet, this is only a lower limit because elements smaller than 16 pixels are not counted in (to avoid errors induced by the intrinsic shape variation of NE patches from frame to frame).

6.2.2 Flux sinks

The three mechanisms through which IN flux disappears from the interior of supergranular cells are flux fading, cancellation and transfer to the NE. In the following we explain how we compute the rates of these processes.

Flux disappearance by fading

The simplest process of flux disappearance from the supergranule is in-situ fading, whereby IN magnetic elements disappear in a given frame without interacting with other features in their vicinity. YAFTA tags fading events as in-situ disappearances, so their detection is relatively straightforward (but see below). The flux they remove from the IN is calculated in a similar way as the flux that appears on the solar surface. If the element does not undergo interactions, the flux lost by fading is the maximum flux it attains during its lifetime. When interactions occur, we determine how the flux decreases from one interaction to the next. In the example of Figure 6.1, the total flux removed by fading would be:

$$F_{\text{fading}} = (F5 - F6) + (F7 - F8) + (F9 - F10) + F_{\text{final}}. \tag{6.2}$$

$F_{\text{final}} = F10$ if the element disappears completely by fading. If the patch loses its label at $F10$ because of a merging with a stronger feature (either from the IN or from the NE), then $F_{\text{final}} = 0$ to avoid counting the flux it had right before the merging. This means we still calculate the flux lost by fading before elements merge with stronger features.

We will use again the example in Figure 6.2 to show how the total faded flux is calculated in practice. The element starts to fade from 13.5 min. Before disappearing completely, it loses flux from $F4$ to $F5$ because of fragmentation occurring at 22.5 min. Since the patch disappears by fading, F_{final} is taken to be $F6$ and, therefore, the total flux lost is calculated as $F_{\text{fading}} = (F3 - F4) + (F5 - F6) + F6 = 15 \times 10^{16}$ Mx.

Flux removal by cancellation

The second mechanism capable of removing flux from the IN is cancellation of opposite-polarity patches. It turns out that YAFTA does not identify this as a process different from in-situ disappearance. To detect cancellations, we use the YAFTA output and look for IN elements that

disappear at most 2 pixels away from an opposite-polarity IN patch. The flux lost by the supergranular cell through this process is equal to the flux that the two canceling features had at the beginning of the cancellation. If the magnetic elements merge with other patches or fragment during the process, we keep track of the changes and revise the total canceled flux accordingly. In partial cancellations with one surviving feature, the canceled flux is taken to be twice the flux of the feature that disappeared completely. Partial cancellations where neither of the elements disappear are very difficult to detect, so we do not account for them. As a consequence, our flux cancellation rates may be smaller than the actual ones. However, the total disappearance rate is correct, because the flux removed in those cases is counted as fading flux. For all the magnetic elements that cancel out, we check if they lose flux before the cancellation starts and ascribe any observed flux drop to fading.

6.2.3 Transfer of the IN flux to the NE

The third mechanism of flux removal from the IN is transfer to the NE. Many IN elements are sufficiently persistent to drift toward the supergranular border (e.g., Orozco Suárez et al. 2012b), where they merge or cancel with NE patches. In both cases, the IN loses flux. These processes are explained in detail in Section 5.2, and examples are shown in Figures 5.1 and 5.2). Just as a reminder, the basic idea is to follow the evolution of each IN flux structure to determine if they interact with a NE patch. The flux lost by the IN is taken to be the flux of the IN element in the frame before the merging or cancellation occurred.

We note that the IN flux our code detects to appear in situ and immediately merge with NE features is counted also as IN flux transferred to the NE, which increases the total flux disappearance rate by almost 5% compared with the plain YAFTA results.

6.2.4 Uncertainties

The main source of error in the YAFTA tracking is the misidentification of magnetic elements that fade and reappear again. As explained in Section 3.3.1, the method we use to correct for this problem depends on a number of (free) parameters such as circle radius, overlapping area, flux, and size criteria. These parameters have been adjusted manually to yield the best possible results, but of course they have an impact on the appearance

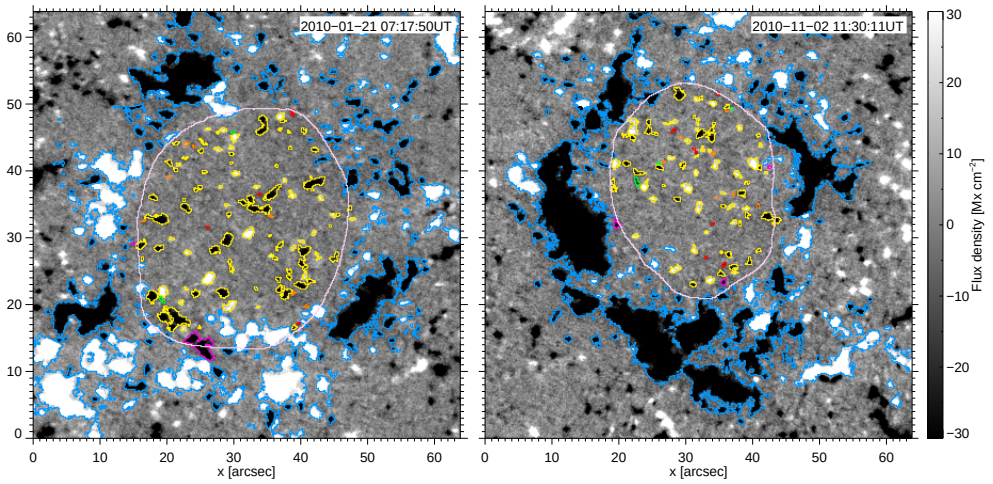

FIGURE 6.3:— Individual supergranular cells in data sets 1 and 4 (left and right, respectively). The cell interiors are outlined by pink contours and the surrounding NE flux features are marked with blue contours. The red contours show IN elements that appear in situ in these frames. Magnetic flux disappears from the cell interiors when elements fade (orange), cancel out (green) or enter the NE and interact with NE features (purple). IN patches that do not undergo any of those processes in the displayed frames are indicated with yellow contours.

and disappearance rates. In what follows we estimate the uncertainties introduced by the choice of parameters.

We use two limiting cases. The first case represents the plain YAFTA results. Here, many magnetic elements are erroneously identified as different structures when their flux drops below the 3σ level and later rises above it.

The other limiting case is computed using only one parameter, namely the radius of the circle in which we look for reappearing elements. If a new magnetic feature shows up inside or touches the border of a circle of radius 4 pixels, then that feature is considered to be the continuation of the previously disappeared element. This criterion is too lax, producing bad identifications of many elements that are detected as reoccurring flux patches. The appearance and disappearance rates in this extreme case are 18% and 14% lower than those from the non-corrected YAFTA output.

The combination of parameters we actually use in the analysis leads to more strict criteria for the identification of these elements. Thus, the corrected appearance and disappearance rates are 10% lower than those obtained with the plain YAFTA tracking, and 14%-10% larger than those

resulting from the second limiting case. Therefore, an upper limit for the uncertainty caused by the choice of parameters is ±14%.

6.3 Results

In this section we will explain how IN regions gain and lose flux. To this purpose we calculate the instantaneous appearance and disappearance rates. To understand whether individual supergranules show spatial variations we also analyze the appearance and disappearance rates depending on the location inside the cells.

The supergranules studied in this chapter are shown in Figure 6.3. The IN elements that appear in situ (red contours), disappear by fading (orange), cancel out (green) and convert to the NE (purple).

6.3.1 Appearance and disappearance rates

Figure 6.4 displays the rates at which the IN gains and loses flux in the supergranular cell of data set 1 as a function of time. The data points are binned in 30 minute intervals.

The top panel of the figure shows the flux appearance rate (solid curve) as a function of time. On average, newly appeared features bring 117 Mx cm^{-2} day^{-1} to the surface. The flux appearance rate computed using the initial flux of the elements (dashed line) is 38 Mx cm^{-2} day^{-1}, with very little fluctuations. The appearance rate increases when strong magnetic elements pop up in the interior of the cell in form of clusters. This happens for example, between 1 and 6 hr. In that period, the instantaneous appearance rate reached up to $\sim$ 200 Mx cm^{-2} day^{-1}.

The middle panel of Figure 6.4 shows the flux removed from the cell by interactions with NE patches (purple curve), fading (orange curve), and cancellations (green curve). Flux transfer from the IN to the NE turns out to be a very important process of flux disappearance from the supergranule, at an average rate of 53 Mx cm^{-2} day^{-1}. This process shows large temporal variations in the selected cell. The peaks between 6 and 8 hr, for example, were produced by strong IN patches leaving the IN and merging with the NE. In addition to this mechanism, flux disappears from the supergranule through fading at a rate of 46 Mx cm^{-2} day^{-1} and through cancellations at a rate of 20 Mx cm^{-2} day^{-1}. Thus, fading and transfer to the NE are equally important sinks of flux for this cell, with cancellations playing a secondary role.

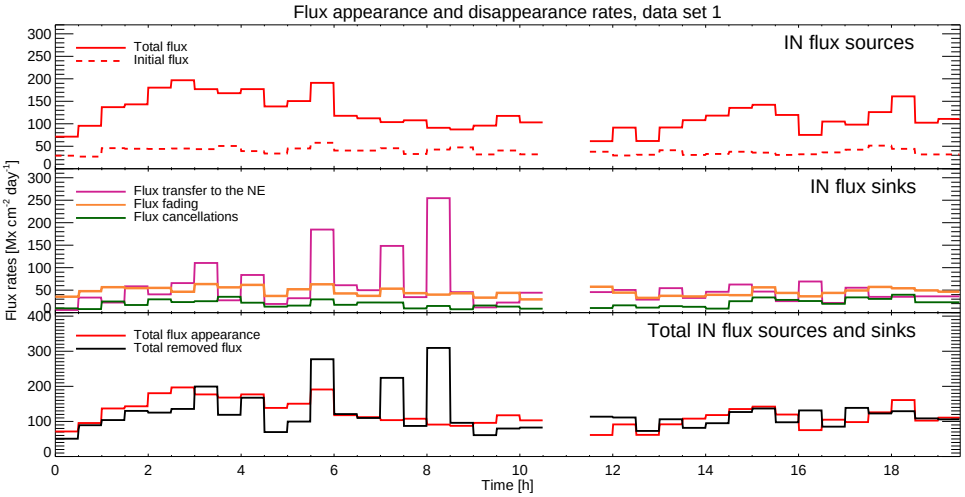

FIGURE 6.4:— Rates at which the central supergranule of data set 1 gains and loses magnetic flux. The data are binned in 30 minute intervals. *Top panel:* The source of IN flux is in-situ appearance of magnetic features and their subsequent evolution (red solid curve). The red dashed line shows the initial flux of elements that appear in situ. *Middle panel:* Flux is removed from the cell by three mechanisms, namely interaction of IN patches with NE elements (flux transfer to the NE; purple), in-situ disappearance of magnetic elements (orange), and cancellation of IN features (green). *Bottom panel:* Total rates at which flux is accumulated (red solid line) and removed (black solid line) from the cell. The latter is defined as the sum of the flux sinks displayed in the middle panel.

The sources and sinks of magnetic flux are summed up and shown in the bottom panel of Figure 6.4 with red and black lines, respectively. As can be seen, the flux appearance and removal rates are similar, but their peaks do not coincide exactly. The reason for this is that magnetic elements tend to grow in flux with time, reach their maximum, and disappear at a later time, depending on their intrinsic evolution and the interactions they undergo.

Figure 6.5 summarizes the results for the supergranular cell of data set 4. We observe a total flux appearance rate of 122 Mx cm^{-2} day^{-1}, the initial flux appearance rate is very stable at 41 Mx cm^{-2} day^{-1} (dashed line).

Also in this case, transfer of IN flux to the NE and fading are the main flux removal mechanisms (second panel of Figure 6.5). The rates at which the cell loses flux through interactions with the NE is 47 Mx cm^{-2} day^{-1}. Fading is slightly larger, accounting for 59 Mx cm^{-2} day^{-1}, while cancella-

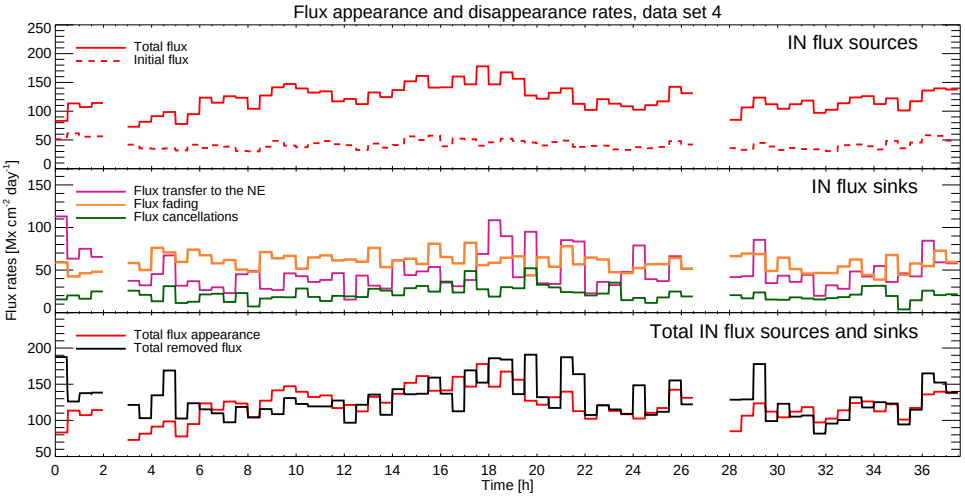

FIGURE 6.5:— Same as Figure 6.4, for the central supergranule of data set 4.

tions proceed at a rate of 25 Mx cm^{-2} day^{-1}. In general, IN patches that convert into NE elements are small, but occasionally we detect strong IN features carrying much flux away from the cell interior. These events are easily distinguishable at, e.g., the beginning of the time sequence or 18 hr. The cancellation rates are smaller but more stable than the flux transfer to the NE.

Just like in data set 1, the supergranular cell of data set 4 gains and loses flux at nearly the same rate (Figure 6.5, bottom panel).

6.3.2 Spatial variations of appearance and disappearance rates

To understand whether the properties of individual supergranular cells depend on location, we determine how appearance and disappearance rates change with the radial distance from the center of the supergranular cells. To do this, we divide the cells into ten rings of equal width. The rings have the shape of the supergranular borders at any time (see Figure 6.6). We then calculate how many elements appear/disappear inside of each ring over time and integrate their fluxes. In this case we use the initial/final fluxes of magnetic patches because these fluxes are not affected by interactions. They will clearly show whether mechanisms responsible for appearance and disappearance of flux patches have any preferences with respect to location.

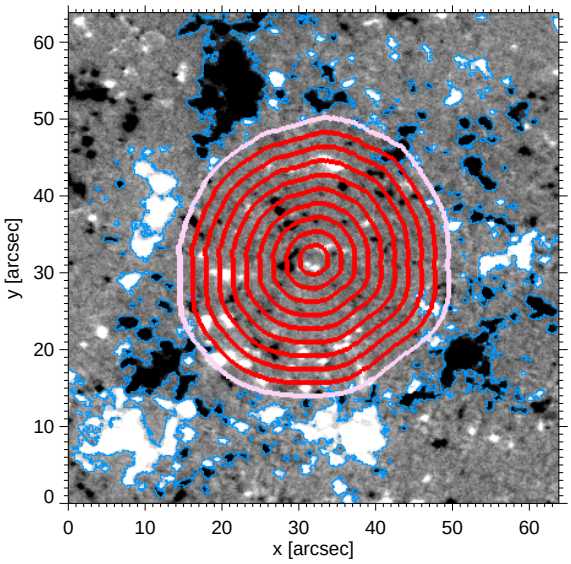

FIGURE 6.6:— Example of the equidistant rings (red contours) that are used to study the spatial variations of the supergranular cells of data set 1. The boundary of the cell is marked with the pink contour.

In Figure 6.7 (top panels) we show the initial flux appearance rate as a function of normalized distance inside the supergranules of data sets 1 (left panel) and 4 (right panel). In both cases, the flux appearance rate increases toward to the border of the cells. This suggests that formation of magnetic patches is not homogeneous over the area. In addition to this, slightly more negative elements appear. Their appearance rates account for 54% and 53% in data set 1 and 4, respectively.

By contrast, the disappearance rate is practically constant with distance (Figure 6.7, middle panels). Again, more negative flux fades out, 55% of the total faded flux (using final fluxes) in data set 1, and 52% in data set 4. This is expected because more negative elements appear in-situ.

The bottom panels show that the cancellation rate also increases toward the cells boundaries. In this case, we do not distinguish between positive and negative flux contributions as they are equal by definition. The maximum is attained at $r = 0.65$ in data set 1, and at $r = 0.95$ in data set 2.

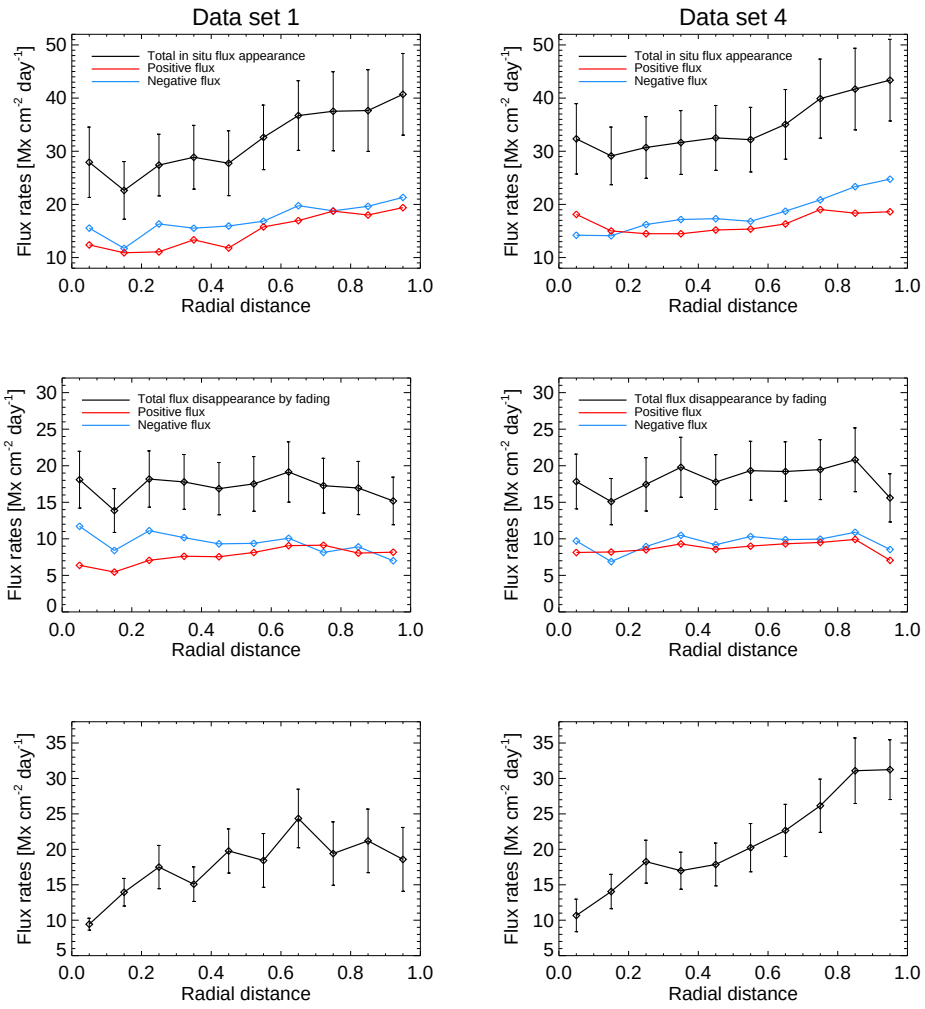

FIGURE 6.7:— Appearance and disappearance rates as functions of the radial distance from the center of the supergranular cells. A distance of 1 represents the cell boundary. Results for data set 1 are shown in the left column and for data set 4 in the right column. *Top panels:* Initial flux appearance rates. *Middle panels:* Fading rate, which is determined using the flux of the magnetic elements before they completely disappear. *Bottom panels:* Cancellation rates. Vertical black lines represent error bars. Error bars for positive and negative fluxes are omitted for clarity.

6.4 Discussion

Table 6.1 summarizes the appearance and disappearance rates we have from the analysis of the Hinode/NFI observations. The quality of our

TABLE 6.1:— IN flux appearance and disappearance rates (Mx cm^{-2} day^{-1}).

	Data set 1	Data set 4	Mean
Appearance			
In-situ	117	122	119.5
Disappearance			
Fading	46	59	52.5
Cancellation	20	25	22.5
Transfer to NE	53	47	50
Total	119	131	125
Disappearance/Appearance	1.02	1.07	1.04

method can be assessed from Figures 6.8 and 6.9. They show the temporal evolution of the total unsigned IN flux (red curves) in data sets 1 and 4, respectively. These curves are derived summing the unsigned fluxes of all detected IN elements. The black curves show the evolution of the reconstructed flux, which is calculated by setting manually an initial flux value and integrating with time the total appeared and disappeared flux.

According to our results, in-situ appearance of magnetic elements in IN regions occurs at a rate of ∼120 Mx cm^{-2} day^{-1} (∼40 Mx cm^{-2} day^{-1} if the initial flux of the magnetic elements is considered). The total flux appearance rate is nearly the same for the two individual supergranular cells studied here, but it changes whenever clusters of magnetic elements emerge into the surface. In those moments, the instantaneous rates can be as large as 200 Mx cm^{-2} day^{-1}.

Our total appearance rate implies that the flux brought to the entire solar surface by IN elements, 7.3×10^{24} Mx day^{-1}, is larger than the 3×10^{22}–1.5×10^{24} Mx day^{-1} injected by bipolar structures such as ephemeral regions (Schrijver et al. 1997; Title 2000; Chae et al. 2001; Hagenaar 2001; Hagenaar et al. 2008), the 2.6×10^{24} Mx day^{-1} brought to the solar surface by horizontal IN fields (Lites et al. 1996b), and the $\sim 10^{24}$ Mx day^{-1} carried by small-scale magnetic loops emerging in the solar IN (Zirin 1987; Martínez González & Bellot Rubio 2009). On the other hand, our values are significantly lower than those reported by Thornton & Parnell (2010) and Zhou et al. (2013), also based on Hinode NFI measurements. Still, they are enormous.

The removal of flux from supergranular cells occurs mainly through

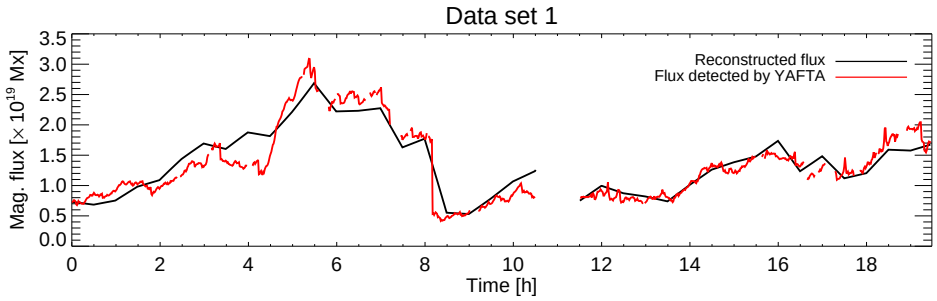

FIGURE 6.8:— The temporal evolution of the total unsigned IN flux in the interior of the supergranule of data set 1 (red line) and the flux reconstructed from the appearance and disappearance rates (black curve).

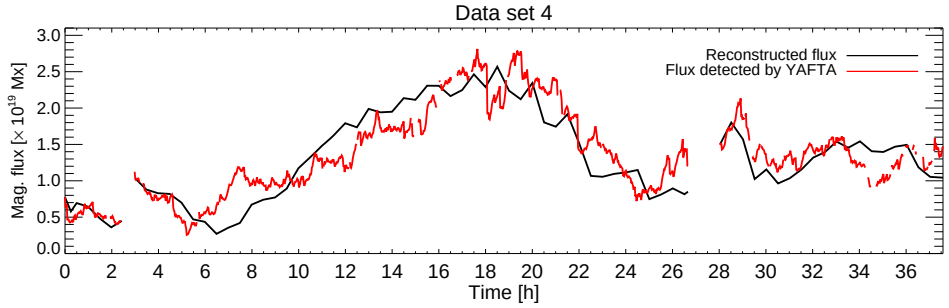

FIGURE 6.9:— Same as Figure 6.8 but for data set 2.

interactions of IN features with NE patches and in-situ fading, at rates of $\sim$50 Mx cm^{-2} day^{-1} and $\sim$53 Mx cm^{-2} day^{-1}, respectively. These two mechanisms account for about 40% and 42% of the total flux lost by IN regions, respectively. The rest disappears by cancellation of IN elements, at a rate of $\sim$23 Mx cm^{-2} day^{-1} which is nearly the same in the two supergranules we have studied.

Our results show that the total disappearance rate implied by the three mechanisms capable of removing flux from the IN is similar to the rate at which the supergranules gain flux. They coincide to within about 4%, reflecting the steady state nature of the solar IN. The small imbalance we observe is probably not real, but a result of our limited magnetic sensitivity and ability to detect and interpret interactions between IN patches.

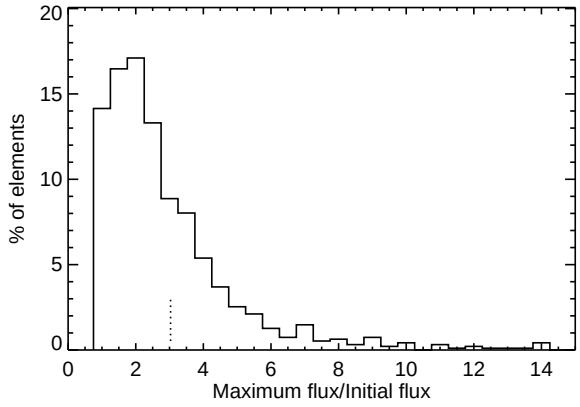

FIGURE 6.10:— Histogram of the ratio between the maximum and the initial flux of the IN elements that appear in situ, live for at least 4 frames (6 minutes), and never interact with other elements in data set 4. The mean and median of the distribution are 3.0 and 2.4, respectively.

IN magnetic elements appear all over the interior of supergranular cells, not only at their centers. Actually, we find that the flux appearance rate increases with distance from the center of the supergranules. This means that the mechanism which produces the appearance of magnetic flux is more effective with the radial distance, reaching the maximum close to the border. This is consistent with previous results by Wang (1988a), Martínez González et al. (2012b) and Stangalini (2014). They all point out that magnetic elements have a slight preference to appear close to the supergranular borders. Stangalini (2014) argued that this may be caused by the supergranular velocity field. This idea comes from the results of Orozco Suárez et al. (2012b). They determined that the radial velocities of magnetic elements depend on the location within the supergranules. The velocities first increase and then drop toward the boundary. It may happen that due to this effect, the flux is accumulated at the edges of the cells. This would cause more efficient coalescence of flux structures, including the background flux not accessible to our observations until the flux is intensified sufficiently to appear in magnetograms. There is also the possibility that newly formed patches close to the borders are flux recycled from the NE, explaining why the appearance rates increase there.

Fading of magnetic elements is practically constant with distance, therefore the mechanism which drives the fading operates equally every-

where in the cell. Cancellations and flux transfer to the NE are more frequent near the boundary of the supergranular cells. Taking into account all sink mechanisms, more flux is removed from the cell as the radial distance increases.

Comparing the total and initial appearance rates it is clear that magnetic elements grow in flux upon appearance. In our data, the average initial flux of IN elements is 1.3×10^{16} Mx. As can be seen in Figure 6.10, their maximum flux is on average 3.0 times larger than the initial flux. This has been determined using all IN elements that appear in situ, live for more than six minutes, and never interact with other features (Gošić 2012), so it is an intrinsic change. Such a flux increase explains why the ratio between the total and initial flux appearance rates is also about 3.

The fact that magnetic elements gain flux after their appearance is puzzling but may convey important information on the origin of the IN flux. One possibility is that the increase is simply due to continuous flux emergence on the surface. Another possibility is that the magnetic features are formed by coalescence of undetected background flux which is too weak to stand out above the noise level until sufficient flux has accumulated, as proposed by Lamb et al. (2008, 2010). This process may continue after the feature is first detected, increasing its flux. Changes in the magnetic field inclination, with the structures becoming more vertical with time, is another possible explanation for the flux increase detected by longitudinal magnetograms (Bellot Rubio & Orozco Suárez 2015). It is necessary to confirm whether or not these mechanisms operate on the solar surface and understand how they affect observations, because of their implications. For example, if a large fraction of the flux that appears in situ is due to coalescence and not to genuine bipolar emergence, then the actual amount of new flux brought to the surface may be significantly smaller than suggested by current analyses. In that case, part of the flux observed in intergranular cells would actually be recycled (network?) flux whose magnetic connectivity is impossible to trace after substantial reprocessing. In fact, increase of the flux appearance rates with radial distance supports the idea that part of the IN flux observed to pop up on the solar surface is indeed recycled flux. Near the NE, one can expect to find a larger amount of recycled flux, and therefore, more vigorous coalescence of background flux, leading to larger IN flux appearance rates, as observed. To clarify these issues, the modes of appearance of IN elements has to be investigated.

6.5 Conclusions

In this chapter we determined the total appearance and disappearance rates in the two supergranular cells of data sets 1 and 4. We studied their temporal and spatial evolution to understand how they gain and lose flux, and whether these processes depend on the location. We summarize bellow our main conclusions.

1. IN elements in the two supergranular cells appear at an enormous, and the same rate of $\sim$120 Mx cm^{-2} day^{-1}. The appearance rate is not constant with time.

2. The disappearance rate is $\sim$125 Mx cm^{-2} day^{-1}, which means that the appearance and disappearance rates are in balance.

3. In terms of magnetic flux, supergranular cells show spatial variations. Appearance rate of IN elements is much more efficient at the border of supergranular cells, as well as the flux removal. This results support the idea of flux recycling (at least around NE regions).

4. IN flux transfer to the NE is very important mechanism, being responsible for removal of $\sim$ 40% of the IN flux.

7

Conclusions and Future Work

In this thesis we have studied the evolution of the quit Sun flux at the unprecedented spatial and temporal resolution. We used long duration observations with the highest sensitivity ever achieved with a filter instrument, using Hinode Narrowband Filter Imager. This chapter summarizes the conclusions drawn in the thesis and give our plans for future work.

In the frame of the Hinode observational program entitled as "Flux replacement in the photospheric network and internetwork" (HOP 151), five observational runs were made until now. We used the data sets obtained on January 20-21, 2010 and November 2-3, 2010. The observed spectral region contains Na I D1 resonance line at 589.6 nm. The data sets are characterized by high sensitivity of only 4 Mx cm^{-2}, the spatial resolution of 0.16 arcsec/pixel and the cadence of $\sim$60 s. They continuously monitored the same supergranular cells on the solar surface for up to 40 hours without interruptions. All these requirements are needed to investigate the evolution of individual IN patches and surrounding NE regions. In fact, these measurements allowed us to study for the first time the temporal evolution of quiet Sun magnetic elements in the range 10^{16}-10^{20} Mx from minutes to days.

To determine the history of individual flux features in the solar photosphere we have developed an IDL code which resolves the main problems of the YAFTA feature tracking algorithm. Only with this code we could track the spatial and temporal evolution of IN and NE patches. More precisely, our code provides accurate interpretation of:

1. appearance and disappearance modes of magnetic elements;
2. subsequent temporal and spatial evolution;
3. variations of physical parameters of flux features;
4. and interactions between them;

which was not possible to accomplish with currently available tracking codes. With our corrections of the YAFTA results we can reliably calculate the flux harbored in NE and IN regions on the Sun, and study their temporal and spatial fluctuations.

To this purpose, we have examined separately IN and NE flux features. We classify them on the basis of their dynamical properties and evolution of supergranular cells which is examined by means of local correlation tracking. We calculated the distributions of their characteristic physical parameters such as the flux density, the size and the total unsigned flux. The latter is used to estimate the flux budget of IN and NE regions. We examined how the flux in the two regions evolve with time. Our conclusions are:

1. IN and NE fluxes in the full FOV are very stable and exhibit only small fluctuations with time, which indicates their steady-state nature.
2. IN flux contributes to 15% of the total unsigned QS flux. The rest is in form of NE patches.
3. The total unsigned IN and NE fluxes over the entire solar surface are $0.7 - 1.1 \times 10^{23}$ Mx and $5.5 - 8.0 \times 10^{23}$ Mx, respectively.
4. IN regions are in nearly perfect polarity balance, while NE regions exhibit clear polarity imbalances which goes up to 85% of the total flux in favor of negative polarity elements.

We estimated that the total NE flux is comparable to the total flux in active regions, which testifies to their importance. Because of this it was crucial to investigate how the NE flux is formed and maintained in the QS. Since NE is coupled to the supergranular flow fields and surrounded by IN features, our hypothesis was that small-scale IN flux may contribute to the NE and possibly provide the answer to the origin of NE flux.

We now know that IN regions inside individual supergranular cells are very dynamic. They harbor mean unsigned flux of $\sim 1.4 \times 10^{19}$ Mx, which may increase by an order of magnitude when clusters of flux patches appear. Many of them reach the NE region. Thus, it seems reasonable to study whether IN elements may be responsible for maintenance of NE flux. To this purpose, we followed IN and NE magnetic patches and analyzed their interactions. IN features change NE flux through merging and cancellation processes. We determined that in this way, IN deposits enormous amounts of flux to the NE, which has been unknown until now. Because of this we concluded that:

1. Small-scale IN elements are the main source of flux for the NE and consequently for the entire QS. The rate at which IN transfers the flux to NE is 1.5×10^{24} Mx day^{-1}.

2. The IN transfers as much flux as is present in the NE in about 10 hr.

3. ERs are minor contributor to the NE flux, accounting for only 10% of the total IN flux transfered to the NE.

4. From our observations ERs seem to be the same as other IN elements but on larger spatial and temporal scales.

Since IN flux turned to be the most important source of flux in the QS, we studied the evolution of individual IN patches to understand how they are maintained on the solar surface. To this aim, we calculated the total appearance and disappearance rates of IN elements and studied their temporal and spatial variations. We summarize bellow our main conclusions:

1. IN elements in the two supergranular cells appear at the rate of $\sim$120 Mx cm^{-2} day^{-1}. The appearance rate varies with time.

2. The appeared flux is balanced by removal mechanisms (fading, cancellations and flux transfer), that occur practically at the same rate of $\sim$125 Mx cm^{-2} day^{-1}.

3. The flux in supergranular cells exhibits spatial variations. The appearance and disappearance rates of IN elements are higher at the border of supergranular cells, which support the idea that at least some amount of flux is recycled.

According to our results, IN fields are crucial for the QS magnetism. Thus, it is essential to understand the origin of these fields. This problem receives a lot of attention but has not been resolved yet. To this purpose, we will analyze in future how and where IN patches appear. By distinguishing between different modes of appearance of magnetic elements, we will be able to decipher whether IN flux is formed by recycled flux or due to genuine bipolar emergence. We will use the same HOP 151 observations accompanied with novel magnetic field extrapolation technique (Cheung & DeRosa 2012).

After that we will investigate how the emergence of magnetic loops in the photosphere rise up and affect the chromosphere and corona. We know that some small-scale magnetic loops may reach the chromosphere and produce transient brightnenings in Ca II H line, which is probably a signature of local chromospheric heating (Martínez González & Bellot Rubio, 2009). The propagation of energy released due to the photospheric magnetic activity into the chromosphere and corona, will be investigated using Hinode, SDO and The Interface Region Imaging Spectrograph (IRIS; De Pontieu et al. 2014). This will help us to better understand the coupling between photospheric, chromospheric and coronal magnetic fields.

The other important process through which IN fields may release the energy is cancellation. Many IN patches disappear by canceling with opposite polarity IN and/or NE features. We want to investigate whether cancellations involving IN fields may be an important source of energy for the chromosphere and the corona.

Bibliography

Asensio Ramos, A. 2009, ApJ, 701, 1032

Asensio Ramos, A., Martínez González, M. J., López Ariste, A., Trujillo Bueno, J., & Collados, M. 2007, ApJ, 659, 829

Attie, R., & Innes, D. E. 2015, A&A., 574, 106

Barthol, P., et al. 2011, Solar Phys., 268

Beck, C., Schmidt, W., Kentischer, T., & Elmore, D. 2005, A&A, 437, 1159

Bellot Rubio, L. R., & Collados, M. 2003, A&A, 406

Bellot Rubio, L. R., & Orozco Suárez, D. 2015, Living Reviews in Solar Physics, in press

Berkefeld, T., et al. 2011, Solar Phys., 268

Berthomieu, G., Cooper, A., Gough, D., Osaki, Y., Provost, J., & Rocca, A. 1980, in Lecture Notes in Physics, Vol. 125, Nonradial and Nonlinear Stellar Pulsation, ed. H. Hill & W. Dziembowski (Springer Berlin / Heidelberg), 307

Bommier, V., Derouich, M., Landi degl'Innocenti, E., Melodij, G., & Sahal-Bréchot, S. 2005, A&A, 432, 295

Bommier, V., Landi degl'Innocenti, E., Feautrier, M., & Melodij, G. 2006, A&A, 458, 625

Borrero, J. A., & Kobel, P. 2011a, A&A, 527, 29

—. 2011b, A&A, 547, 89

Brault, J. W., & Neckel, H. 1987, Spectral Atlas of Solar Absolute Disk-averaged and Disk-Center Intensity from 3290 to 12510 Å, ftp://ftp.hs.unihamburg.de/pub/outgoing/FTS-Atlas

Cattaneo, F. 1999, ApJ, 515, 39L

Cattaneo, F., & Hughes, D. W. 2001, Astron. Geophys., 42, 318

Centeno, R., et al. 2007, ApJ, 666, 137

Chae, J., Martin, S. F., Yun, H. S., Kim, J., Lee, S., Goode, P. R., Spirock, T., & Wang, H. 2001, ApJ, 548, 497

Cheung, M. C. M., & DeRosa, M. L. 2012, ApJ, 757

Collados, M., Lagg, A., Díaz García, J. J., Hernández Suárez, E., López López, R., Páez Mañá, E., & Solanki, S. K. 2007, inASPConf. Ser. 368, The Physics of Chromospheric Plasmas, ed. P. Heinzel, I. Dorotovič, & R. J. Rutten (San Francisco, CA: ASP), 611

Danilović, S., et al. 2010, ApJ, 723, 149L

De Pontieu, B. 2002, ApJ, 569, 474

De Pontieu, B., et al. 2014, Solar Phys., 289, 7

de Wijn, A. G., Lites, B. W., Berger, T. E., Frank, Z. A., & Tarbell, T. D. 2008, ApJ, 684, 1469

De Wijn, A. G., Rutten, R. J., Haverkamp, E. M. W. P., & Sötterlin, P. 2005, A&A, 441, 1183

De Wijn, A. G., Stenflo, J. O., Solanki, S. K., & Tsuneta, S. 2009, Space Sci. Rev., 144, 275

DeForest, C. E., Hagenaar, H. J., Lamb, D. A., Parnell, C. E., & Welsch, B. T. 2007, ApJ, 666, 567

Del Moro, D., Giordano, S., & Berrilli, F. 2007, A&A, 472, 599

DeRosa, M. L., & Toomre, J. 2004, ApJ, 616

Derouich, M., Bommier, V., Malherbe, J. M., & Landi degl'Innocenti, E. 2006, A&A, 457, 1047

Domínguez Cerdeña, I., Kneer, F., & Sánchez Almeida, J. 2003, ApJ, 582, L55

Domínguez Cerdeña, I., Sánchez Almeida, J., & Kneer, F. 2006, ApJ, 646, 1421

Faurobert, M., Arnaud, J., Vigneau, J., & Frisch, H. 2001, A&A, 378, 627

Faurobert-Scholl, M., Feautrier, N., Machefert, F., Petrovay, K., & Spielfiedel, A. 1995, A&A, 298, 289

Giannattasio, F., Del Moro, D., Berrilli, F., Bellot Rubio, L. R., Gošić, M., & Orozco Suárez, D. 2013, ApJ, 770, L36

Gošić, M. 2012, Master Thesis, University of Granada (Spain)

Gošić, M., Bellot Rubio, L. R., Orozco Suárez, D., Katsukawa, Y., & del Toro Iniesta, J. C. 2014, ApJ, 797, 49

Grossmann-Doerth, U., Keller, C. U., & Schüssler, M. 1996, A&A, 315

Guglielmino, S. L., et al. 2012, ApJ, 745, 160

Hagenaar, H. J. 2001, ApJ, 555, 448

Hagenaar, H. J., DeRosa, M. L., & Schrijver, C. J. 2008, ApJ, 678, 541

Hagenaar, H. J., Schrijver, C. J., & Title, A. M. 2003, ApJ, 584, 1107

Hagenaar, H. J., Schrijver, C. J., Title, A. M., & Shine, R. A. 1999, ApJ, 511, 932

Hagenaar, M., & Cheung, M. 2009, ASP Conference Series, 415, 167

Hart, A. B. 1956, MNRAS, 116

Harvey, K. L., Harvey, J. W., & Martin, S. F. 1975a, Solar Phys., 40, 87

—. 1975b, Solar Phys., 40, 87

Harvey, K. L., & Martin, S. F. 1973, Solar Phys., 32, 389

Harvey, K. L., & Zwaan, C. 1993, Solar Phys., 148, 85

Harvey-Angle, K. L. 1993, Ph.D. Thesis, Utrecht University, Utrecht

Iida, Y., Hagenaar, H., & Yokoyama, T. 2015, arXiv:1510.04764

Iida, Y., Hagenaar, H. J., & Yokoyama, T. 2012, Annual review of astronomy and astrophysics, 752, 149

Ishikawa, R., & Tsuneta, S. 2009a, A&A, 495, 607

—. 2009b, ASP Conference Series, 415, 132

Ishikawa, R., Tsuneta, S., & Jurčák, J. 2010, ApJ, 713, 1310

Ishikawa, R., et al. 2008, A&A, 481, 25L

Jin, C., Wang, J., & Xie, Z. 2012, Solar Phys., 280, 51

Jin, C., Wang, J., & Zhou, G. 2009, ApJ, 697, 693

Keller, C. U., Deubner, F. L., Egger, U., Fleck, B., & Povel, H. P. 1994, A&A, 286, 626

Khomenko, E. V., Collados, M., Solanki, S. K., Lagg, A., & Trujillo Bueno, J. 2003, A&A, 408, 1115

Kosugi, T., et al. 2007, Solar Phys., 243, 3

Lamb, D., & DeForest, C. E. 2003, Fall AGU Meeting, abstract SH42B-0530

Lamb, D. A., DeForest, C. E., Hagenaar, H. J., Parnell, C. E., & Welsch, B. T. 2008, ApJ, 674, 520

—. 2010, ApJ, 720, 1405

Lamb, D. A., Howard, T. A., DeForest, C. E., Parnell, C. E., & Welsch, B. T. 2013, ApJ, 774, 127

Landi Degl'Innocenti, E., & Landi Degl'Innocenti, M. 1973, Solar Phys., 27, 319

Landi Degl'Innocenti, E., & Landolfi, M. 2004, Solar and Stellar Magnetic Activity (Kluwer Academic Publishers)

Leighton, R. B., Noyes, R. W., & Simon, G. W. 1962, ApJ, 135

Lemen, J. R., et al. 2012, Solar Phys., 275, 17

Lin, H. 1995, ApJ, 446, 421

Lin, H., & Rimmele, T. 1999, ApJ, 514, 448

Lites, B. W. 2002, ApJ, 573, 431

Lites, B. W., Leka, K. D., Skumanich, A., Martínez Pillet, V., & Shimizu, T. 1996a, ApJ, 460, 1019

—. 1996b, ApJ, 460, 1019

Lites, B. W., et al. 2013, Solar Phys., 283, 579

Livi, S. H. B., Wang, J., & Martin, S. F. 1985, Aust. J. Phys., 38, 855

Livingston, W. C., & Harvey, J. W. 1971, Solar Magnetic Fields, 43, 51

—. 1975, Bull. Am. Astron. Soc., 7, 346

López Ariste, A., Tomczyk, S., & Casini, R. 2002, ApJ, 580, 519

—. 2006, A&A, 454, 663

Martin, S. F. 1988, Solar Phys., 117, 243

—. 1990, in IAU Symp. 138, Solar Photosphere: Structure, Convection, and Magnetic Fields, ed. J. O. Stenflo (Cambridge: Cambridge Univ. Press), 138, 129

Martin, S. F., Livi, S. H. B., & Wang, J. 1985, Aust. J. Phys., 38, 929

Martínez González, M. J., & Bellot Rubio, L. R. 2009, ApJ, 700, 1391

Martínez González, M. J., Bellot Rubio, L. R., Solanki, S. K., Martínez Pillet, V., Del Toro Iniesta, J. C., Barthol, P., & Schmidt, W. 2012a, ApJ, 758, L40

Martínez González, M. J., Collados, M., & Ruiz Cobo, B. 2006, A&A, 456, 1159

Martínez González, M. J., Collados, M., Ruiz Cobo, B., & Beck, C. 2008, A&A, 477, 953

Martínez González, M. J., Collados, M., Ruiz Cobo, B., & Solanki, S. K. 2007, A&A, 469, L39

Martínez González, M. J., Manso Sainz, R., Asensio Ramos, A., & Hijano, E. 2012b, ApJ

Martínez Pillet, V. 2013, Space Sci. Rev., 178, 141

Martínez Pillet, V., et al. 2011, Solar Phys., 268

Matloch, L., Cameron, R., Schmitt, D., & Schüssler, M. 2009, A&A, 504, 1041

Meunier, N., Solanki, S. K., & Livingston, W. C. 1998, A&A, 331, 771

Nordlund, A. 2008, Phys. Scr., 133, 014002

Nordlund, A., Stein, R. F., & Asplund, M. 2009, Living Reviews in Solar Physics, 2, 6

November, L. J., & Simon, G. W. 1988, ApJ, 333, 427

November, L. J., Toomre, J., & Gebbie, K. B. 1981, ApJ, 245, 123L

Orozco Suárez, D., & Bellot Rubio, L. R. 2012, ApJ, 751, 2

Orozco Suárez, D., Bellot Rubio, L. R., Del Toro Iniesta, J. C., & Tsuneta, S. 2008, A&A, 481, 33L

Orozco Suárez, D., Bellot Rubio, L. R., & Katsukawa, Y. 2012a, arXiv:1203.2185v1

Orozco Suárez, D., Katsukawa, Y., & Bellot Rubio, L. R. 2012b, ApJ, 758, L38

Orozco Suárez, D., et al. 2007a, ApJ, 670, 61L

—. 2007b, Publ. Astron. Soc. Jpn, 59, 837

Parker, E. N. 1955, ApJ, 122

Parnell, C. E. 2002, MNRAS, 335, 389

Parnell, C. E., DeForest, C. E., Hagenaar, H. J., Johnston, B. A., Lamb, D. A., & T., W. B. 2009, ApJ, 698, 75

Pietarila, A., Cameron, R. H., Danilović, S., & Solanki, S. K. 2011, ApJ, 729, 136

Ploner, S. R. O., Schüssler, M., & Solanki, S. K. 2001, ASP Conference Series, 236, 363

Requerey, I. S., Del Toro Iniesta, J. C., Bellot Rubio, L. R., Bonet, J. A., Martínez Pillet, V., Solanki, S. K., & Schmidt, W. 2014, ApJ, 789, 6

—. 2015, ApJ, 810, 79

Rieutord, M., & Rincon, F. 2010, Living Reviews in Solar Physics, 2, 7

Rieutord, M., Roudier, T., Malherbe, J. M., & Rincon, F. 2000, A&A, 357, 1063

Rimmele, T., & Schröter, E. H. 1989, A&A, 221

Roudier, T., Rieutord, M., Malherbe, J. M., & Vigneau, J. 1999, A&A, 349, 301

Sánchez Almeida, J., & Lites, B. W. 2000, ApJ, 532, 1215

Sánchez Almeida, J., & Martínez González, M. J. 2011, Solar Polarization 6, 437, 451

Sánchez Almeida, J., Viticchié, B., Landi Degl'Innocenti, E., & Berrilli, F. 2008, ApJ, 675, 906

Scherrer, P. H., et al. 1995, Solar Phys., 162, 129

—. 2012, Solar Phys., 275, 207

Schrijver, C. J., & Harvey, K. L. 1994, Solar Phys., 150, 1

Schrijver, C. J., Title, A. M., van Ballegooijen, A. A., Hagenaar, H. J., & Shine, R. A. 1997, ApJ, 487, 424

Schrijver, C. J., & Zwaan, C. 2000, Solar and Stellar Magnetic Activity (Cambridge University Press)

Schrijver, C. J., et al. 1998, Nature, 394, 152

Shine, R. A., Simon, G. W., & Hurlburt, N. E. 2000, Solar Phys., 193

Simon, G. W., & Leighton, R. B. 1964, ApJ, 140

Simon, G. W., Title, A. M., & Weiss, N. O. 2001, ApJ, 561, 427

Smithson, R. C. 1975, Bull. Am. Astron. Soc., 7, 346

Socas-Navarro, H., & Lites, B. W. 2004, ApJ, 616, 587

Solanki, S. K., Keller, C., & Stenflo, J. O. 1987, A&A, 188

Solanki, S. K., & Stenflo, J. O. 1984, A&A, 140

Solanki, S. K., et al. 2010, ApJ, 723

Stangalini, M. 2014, A&A, 561, L6

Steenbeck, M., & Krause, F. 1969, Astron. Nachr., 291

Stein, R. F., Nordlund, A., Georgobiani, D., Benson, D., & Schaffenberger, W. 2008, GONG2008 SOGO21 conference procedings, arXiv:0811.0472

Stenflo, J. O. 1973, Solar Phys., 32

—. 1982, Solar Phys., 80, 209

Stenflo, J. O., & Harvey, J. W. 1985, Solar Phys., 95

Stenflo, J. O., Keller, C. U., & Gandorfer, A. 1998, A&A, 329, 319

Straus, T., Deubner, F.-L., & Fleck, B. 1992, A&A., 256, 652

Suematsu, Y., et al. 2008, Solar Phys., 249, 197

Thornton, L. M., & Parnell, C. E. 2010, Solar Phys., 269, 13

Title, A. 2000, Philos. Trans. Roy. Soc. London A, 358, 657

Trujillo Bueno, J., Shchukina, N., & Asensio Ramos, A. 2004, Nature, 430, 326

Tsuneta, S., et al. 2008a, ApJ, 688, 1374

—. 2008b, Solar Phys., 167, 5

Unno, W. 1956, PASJ, 8, 108

Vögler, A., & Schüssler, M. 2007, A&A, 465, L43

Wang, H. 1988a, Solar Phys., 117, 343

—. 1988b, Solar Phys., 116, 1

Wang, J., Wang, H., & Shi, Z. 1992, in ASP Conf. Ser. 27, The Solar Cycle, ed. K. L. Harvey, 27, 108

Wang, J., Wang, H., Tang, F., Lee, J. W., & Zirin, H. 1995, Solar Phys., 160, 277

Welsch, B. T., & Longcope, D. W. 2003, ApJ, 588, 620

Wiehr, E. 1978, A&A, 69

Yelles Chaouche, L., et al. 2011, ApJ, 727, 30L

Zhang, J., Wang, J., Wang, H., & Zirin, H. 1998, A&A, 335, 341

Zhou, G., Wang, J., & Jin, C. 2013, Solar Phys., 283, 273

Zhou, G. P., Wang, J. X., & Jin, C. L. 2010, Solar Phys., 267, 63

Zirin, H. 1985, Aust. J. Phys., 38, 961

—. 1987, Solar Phys., 110, 101

Zwaan, C. 1978, Solar Phys., 60

—. 1987, Annual review of astronomy and astrophysics, 25, 83